DEVELOPMENT OF MICROPLASMAS AND ANALYSIS OF COMPLEX BIOMOLECULES USING PLASMA AND SYNCHROTRON RADIATION

A Thesis
Presented to
The Academic Faculty

by

Joshua Milbourne Symonds

In Partial Fulfillment
of the Requirements for the Degree
Doctor of Philosophy in the
School of Physics

Georgia Institute of Technology
August 2014

DEVELOPMENT OF MICROPLASMAS AND ANALYSIS OF COMPLEX BIOMOLECULES USING PLASMA AND SYNCHROTRON RADIATION

Approved by:

Dr. Thomas M. Orlando, Advisor
School of Chemistry and Biochemistry
Georgia Institute of Technology

Dr. Facundo M. Fernández
School of Chemistry and Biochemistry
Georgia Institute of Technology

Dr. Jennifer E. Curtis
School of Physics
Georgia Institute of Technology

Dr. Edward H. Conrad
School of Physics
Georgia Institute of Technology

Dr. Phillip N. First
School of Physics
Georgia Institute of Technology

Date Approved: April 29, 2014

ACKNOWLEDGEMENTS

In the course of this work, I have primarily labored independently. That is not to say it has been a lonely experience: I have always enjoyed a strong support system, for which I am very grateful.

As my advisor, Thom has given me the flexibility to pursue my curiosity, and provided unwavering support for my studies. I have been fortunate to have such a stable environment and so many opportunities to collaborate in the course of my research.

My work in mass spectrometry has benefited immensely from my collaboration with Facundo Fernández and his group. He and Asiri Galhena helped me succeed in a highly interdisciplinary project, and contributed enormously to the chemical analysis in my research.

I have had a great many wonderful colleagues that have helped me in innumerable ways since my first day in the lab. They have all helped me tremendously along this path. In particular, I would like to thank Gregory Grieves and Aleksandr Aleksandrov for their inexhaustible experience and guidance. I would like to thank Heather Abbott-Lyon, Claire Pirim, and Reuben Gann for being good mentors, counselors, and collaborators for me at various times when I needed it most.

Outside of our lab, I would like to thank Richard Rosenberg for an exciting opportunity, a stimulating collaboration, and one of the most scientifically rewarding experiences of my career.

Thanks to Mom, Dad, Ben and Daniel for supporting whatever I do.

Finally, thanks to Allison, who has been indispensable these past months.

TABLE OF CONTENTS

LIST OF TABLES

LIST OF FIGURES

LIST OF SYMBOLS AND ABBREVIATIONS

DC	Direct Current
AC	Alternating Current
XPS	X-ray Photoelectron Spectroscopy
MFC	Mass Flow Controller
sccm	Standard Cubic Centimeters per Minute
SLM	Standard Liters per Minute
CFM	Cubic Feet per Minute
GPH	Gallons Per Hour
MHCD	Microhollow Cathode Discharge
DBD	Dielectric Barrier Discharge
LTP	Low Temperature Plasma Probe
FAPA	Flowing Atmospheric P
HCD	Hollow Cathode Discharge
DART	Direct Analysis in Real Time
ESI	Electrospray Ionization
MS	Mass Spectrometry/Spectrometer
AP	Atmospheric Pressure
UHV	Ultrahigh Vacuum
DAQ	Data Acquisition Module
MCP	Microchannel Plate
PECVD	Plasma-Enhanced Chemical Vapor Deposition
PMMA	Poly(Methyl Methacrylate)

SUMMARY

In this work, a microplasma-based ionization source for ambient mass spectrometry (AMS) has been developed and patented (Chapter 2). Optical emission spectroscopy, optical microscopy, and electrical measurements have been used to characterize the discharge (Chapter 3). The discharge was used in a direct exposure mode in AMS experiments, and was found to behave as a small Penning ionization source capable of ionizing a range of biomolecules (Chapter 4). In order to broaden the effectiveness of the microplasma ionization source, admixtures of hydrogen in neon gas were used to produce vacuum ultraviolet (VUV) light. The 121.6 nm Lyman-α (10.23 eV) photons produced are effective soft (non-destructive), single-photon ionization sources (Chapter 5). Since this photon energy exceeds the ionization potential of many biomolecules, this source is useful for analysis of a wide range of organic samples.

The microplasma source, in both VUV-generating and direct-exposure modes, is proposed as a method by which to study the damage effects on biomolecules, and preliminary results are presented (Chapter 6). The microplasma research presented is summarized in Chapter 7.

Finally, a collaborative work investigating the role of ionizing radiation in the DNA damage process is presented (Chapter 8). Using a synchrotron radiation source, the photolysis of DNA monolayers on gold substrates in a vacuum environment were studied by X-ray photoelectron spectroscopy (XPS) and X-ray absorption spectroscopy (XAS) experiments. My role in this collaboration was the collection of the portion of data taken at the Synchrotron Radiation Center (SRC), contributing to the analysis of data, and

contributing to the preparation of the manuscript. This manuscript has been submitted to the Physical Chemistry Chemical Physics as of April 2014.

Direct-exposure microplasma ionization was supported by the Bio-Imaging Mass Spectrometry Center at Georgia Tech, an NSF CAREER grant 0645094, and published in Analytical Chemistry (Symonds, J. M.; Galhena, A. S.; Fernandez, F. M.; Orlando, T. M., Microplasma discharge ionization source for ambient mass spectrometry. Anal Chem 2010, 82 (2), 621-7.).

VUV-enhanced microplasma ionization research was supported by the NSF through an American Recovery and Reinvestment Act (ARRA) Major Research Instrumentation (MRI) Instrument Development grant 0923179. The manuscript describing this work has been submitted to the Journal for the American Society of Mass Spectrometry, and recommended for acceptance pending revision as of April 2014.

Support for DNA damage studies was provided by the U.S. Department of Energy, Office of Science, Office of Basic Energy Sciences under Contract No. DE-AC02-06CH11357. The Synchrotron Radiation Center, University of Wisconsin-Madison, was supported by the NSF under Award No. DMR-0537588. Support for my work in this collaboration was provided by U.S. Department of Energy, Office of Science, Office of Basic Energy Sciences under Contract No. DE-FG02-02ER15337.

CHAPTER 1
INTRODUCTION

1.1 Motivation for this work

Mass spectrometry (MS) is an incredibly useful technique for rapid analysis of a wide range of samples in clinical and industrial applications. The concept is simple: sample molecules are ionized and the mass-to-charge ratio (commonly written m/z, with units of Da.) is studied. This ratio allows the user to determine the molecular or atomic mass, and subsequently the chemical composition of the sample being analyzed. The process requires six fundamental steps, illustrated in Figure 1.1: (1) sample molecules are separated from any bulk material present, (2) the molecules are ionized, (3-4) they are transported into a mass spectrometer and separated from the background gas, (5) they are guided toward a detector and sorted by the m/z value, and (6) the sorted particles are counted by a detector, and a spectrum of intensity vs. m/z is formed.

This work focuses on developing an improved method for the second step of the process: ionization. Mass spectrometry is a mature technique, and instrumentation exists to perform mass analysis quite effectively. One of the frontiers of current mass spectrometry research is expanding the applicability of mass spectrometry, which requires improvements that may be divided in two themes.

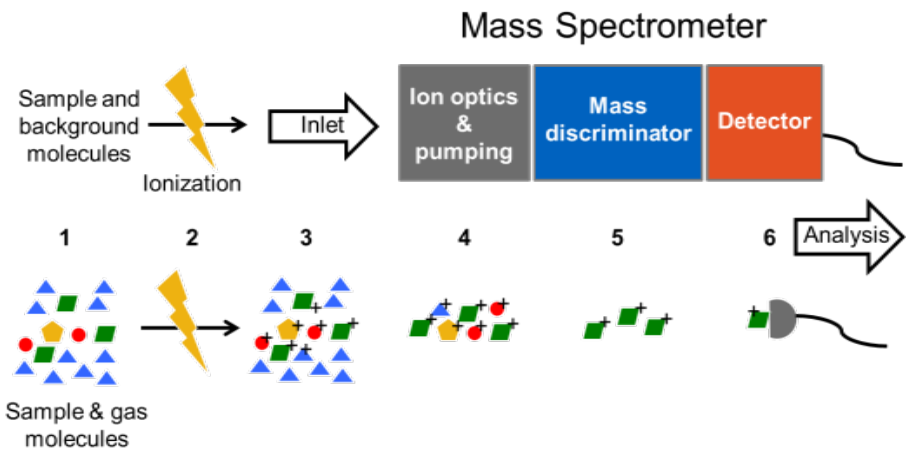

Figure 1.1 Schematic of the ambient mass spectrometry process. (1) Sample molecules are prepared in the gas phase (by desorption, if necessary), (2) where they are ionized, and then (3) transported into the differentially-pumped MS inlet. (4) Neutral molecules are pumped away, leaving ions. (5) A mass discriminator sorts the molecules by m/z value and (6) they are detected, producing the mass spectrum.

The first of these themes is to broaden the applicability of ionization techniques in a wider variety of settings. This includes reducing the sensitivity to the sample environment. Depending on the application, traditional sample preparation steps (such as introduction into a vacuum chamber) may be inconvenient or impossible. This is where ambient mass spectrometry (AMS), a technique that uses vacuum MS detectors to analyze bulk material still in a high pressure environment, becomes crucial. We find many situations where preparation and introduction of a sample into a vacuum chamber for traditional MS is not viable. In clinical settings, such as in an operating room at a hospital, MS may be used to help distinguish cancerous and healthy tissue in vivo [1]. The detectors in use for MS are still reliant on vacuum environments which would be harmful to living tissues, and so sample ions in these experiments must be transported from atmospheric pressure (AP) and pumped down to a low pressure after desorption. The use of radio frequency (RF) ion guides make this step far more efficient, as they

improve the retention of charged particles as the neutral gas is removed from the system. However, this requires sample molecules to already be charged. This provides part of the motivation which has made the high-pressure ionization step a principal area of research in AMS today.

The second theme for new MS technology deals with improving sample-compatibility of the ionization process, making techniques less selective to samples. This sample bias originates from different ionization energies, proton affinities, and reaction pathways of different samples. For the most part, the discrimination that reduces sensitivity to some samples occurs in the ionization step; once ionized, a wide variety of molecules may be transported and detected efficiently. Ionization sources produce charged samples from neutral samples in a variety of ways, and each technique results in some unavoidable chemically-dependent specificity. However, these effects can be minimized by some ionization techniques, and our work includes improvements to the ionization source that broaden the applicability of our process.

The third theme of the current research deals with enhancing the portability of the instrumentation by reducing consumable and power requirements, as well as miniaturization of the hardware. We have endeavored to develop an ionization source suitable for ionization of samples in AMS that lends itself to portable, low-power, and low-cost applications. Such sources will be necessary for the expansion of MS analysis in settings where current MS technology is resource-intensive to be practical.

We have designed and evaluated a microplasma discharge source to fill these needs. Microplasma devices use direct current (DC), alternating current (AC), or pulsed DC potentials on small, closely-spaced electrodes to produce discharges in small gas

flows. Like their larger counterparts, microplasmas are made up of a variety of high-energy particles, including ions, electrons, and photons. We investigated one type of microplasma device, called the microhollow cathode discharge (MHCD), for its reported high-energy electron distribution, low-power DC operation, and simple design. These features fulfill many of the requirements for an AMS ionization source. Microplasmas are used in a wide variety of industrial, medical, scientific, and even residential applications [2-3], but the fundamentals of their operation are not as well-understood. Recent theoretical work has attempted to address this issue [4-5], but understanding of these plasmas and models for their behavior is not yet fully developed. This new territory presents a unique challenge, and we have performed a variety of experiments to characterize some of the fundamental properties of these popular devices.

A parallel research pathway in our laboratory deals with the application of vacuum ultraviolet (VUV) photons to produce single-photon ionization (SPI) in vacuum-based MS experiments. These high-energy photons were found to be excellent ionization sources that produce "soft" ionization (low-fragmentation). Building off work done by Schoenbach *et al.* [6], we found that we could adapt our ambient microplasma source to produce VUV light capable of performing SPI of our samples. Rather than the large and expensive coherent sources typically employed in vacuum-based MS experiments, we modified our source to produce incoherent VUV light via excimer reactions in specialized gas mixtures at high pressure. As shown in Chapter 3, this source combines the performance advantage of SPI with the ease-of-use of AMS, while retaining the low-cost and low-power qualities of microplasmas.

Our work in AMS required us to refine our study of microplasmas by carefully controlling the fabrication methods, and the composition, flow, and pressure of the gases used. We implemented a series of experimental improvements that enabled stable power and gas supply, and we recorded the electrical parameters during operation. After many of these improvements, we attained improved repeatability. However, more meaningfully, the new controls and characterization techniques enabled us to study these devices on a fundamental level and explore the underlying physics. This contribution to the scientific study of MHCDs, in conjunction with research being conducted by other groups, will help to bring microplasmas out of the "dark ages" of application with only limited understanding. In the following work, I present a few steps along this path.

1.2 Fundamentals of DC plasmas

1.2.1 Before the glow: kinetic theory of gases

A particle in contact with a thermal bath at temperature T will have some energy E. The probability that a particle will have some certain energy decreases exponentially as that energy increases, as given by the Boltzmann distribution:

$$f(E)dE = Ae^{-E/kT}. \qquad \text{Equation 1.1}$$

In one dimension, the kinetic energy of such a particle is $E = \frac{1}{2}mv_x{}^2$. This makes our on-dimensional energy distribution:

$$f(v_x)dv_x = Ae^{mv_x{}^2/2kT}. \qquad \text{Equation 1.2}$$

We determine the coefficient A by normalizing the integral over all velocities to account for the fact that the sum of the probabilities must be unity, and find $A = \sqrt{\frac{m}{2\pi kT}}$.

This produces the one-dimensional Maxwell-Boltzmann distribution:

$$f(v_x)dv_x = \sqrt{\frac{m}{2\pi kT}}e^{\frac{-mv_x{}^2}{2kT}}. \qquad \text{Equation 1.3}$$

In three dimensions, the probability of (v_x, v_y, v_z) is the product of three such distributions:

$$f\left(v_x, v_y, v_z\right)dv_{x,y,z} = Ae^{\frac{-m(v_x{}^2+v_y{}^2+v_z{}^2)}{2kT}}. \qquad \text{Equation 1.4}$$

For speed (v), $v^2 = (v_x{}^2 + v_y{}^2 + v_z{}^2)$, and this becomes

$$f(v)dv = Av^2e^{\frac{-mv^2}{2kT}}. \qquad \text{Equation 1.5}$$

After normalization, we get the three-dimensional Maxwell-Boltzmann probability distribution. For n particles, we get the full distribution given by:

$$f(v)dv = \frac{4n}{\sqrt{\pi}}\left(\frac{m}{2kT}\right)^{3/2}v^2e^{\frac{-mv^2}{2kT}}. \qquad \text{Equation 1.6}$$

It is useful to find the mean velocity $(\bar{v})$ of these particles, which we accomplish by evaluating the first moment of the distribution:

$$\bar{v} = \frac{1}{n}\int_0^\infty vf(v)\mathrm{d}v = \sqrt{\frac{8kT}{\pi m}}. \qquad \text{Equation 1.7}$$

1.2.2 Collisions

Collision processes play a central role in the operation of plasmas. Table 1.1 (adapted from [7]) lists the primary processes active in plasma discharges.

Table 1.1 Collision processes in plasmas

Electrons	
$e^- + A \rightarrow A^+ + 2e^-$	Ionization
$e^- + A \rightarrow A^* \rightarrow e^- + A + h\nu$	Excitation
$e^- + A^* \rightarrow 2e^- + A^+$	Penning ionization
$e^- + A \rightarrow e^- + A$	Elastic scattering
$e^- + AB \rightarrow e^- + A + B$	Dissociation
$e^- + AB \rightarrow 2e^- + A^+ + B$	Dissociative ionization
$e^- + AB \rightarrow A^- + B$	Dissociative attachment
$e^- + A^+ + B \rightarrow A + B + h\nu$	Recombination
Ions	
$A^+ + B \rightarrow A + B^+$	Charge exchange
$A^+ + B \rightarrow A^+ + B$	Elastic scattering
$A^+ + B \rightarrow A^+ + B^+ + e^-$	Ionization
$A^+ + B \rightarrow A^+ + B^* \rightarrow A^+ + B + h\nu$	Excitation
$A^+ + e^- + B \rightarrow A + B + h\nu$	Recombination
$A^+ + BC \rightarrow A^+ + B + C$	Dissociation

Kinetic interactions between particles in a gas or plasma are normally binary collisions. These may be either elastic, where the particles conserve kinetic energy after colliding, or inelastic, where some of the kinetic energy is converted to another form, such as during an excitation or ionization event.

In the case of elastic collisions, we may represent the interaction using the hard sphere model (Figure 1.2). The cross section for the collision, σ, is a function of the effective size of the two colliding particles.

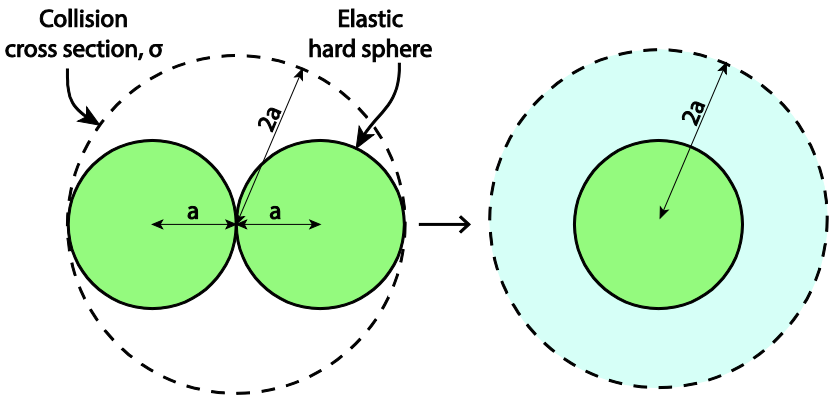

Figure 1.2 Hard sphere model for two colliding particles, each with radius a. The cross sectional area σ for this case is the area of the dashed circle.

For two colliding particles each of radius a,

$$\sigma = \pi(2a)^2 = 4\pi a^2 \ (\mathrm{m}^2). \qquad \text{Equation 1.8}$$

Weakly ionized plasmas, which describe every discharge relevant to this work, are mostly free of collisions involving two charges for which Coulomb forces must be accounted [7]. This is purely statistical, as the neutrals far outnumber ions. In this case, most collisions of interest involve a charged particle and a neutral particle. This type of system is referred to as a Lorentzian gas.

To determine the mean free path of a particle in this model, we consider a test particle which travels in a straight path until it collides with a background particle. In order to simplify this calculation, we may consider the test particle to sweep a regular cylinder through space; the base of the cylinder is equal to the cross sectional area of the test particle, σ, and the length is the distance travelled by the test particle in time t, as shown in Figure 1.3.

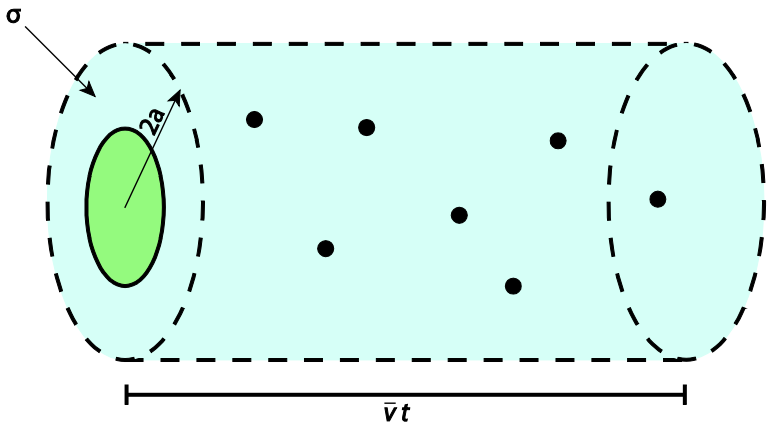

Figure 1.3 A "test cylinder" swept out by a test particle in time t. The number of collisions in this model is given by the volume of the cylinder swept out by the test particle with cross section σ.

Our test particle cross section contains the entire "size" of the interaction, so we need only consider the centers of the background particles contained in our test cylinder. If we assign the test particle a mean velocity $\bar{v}$ (given by Equation 1.7), the volume of the test cylinder is $\sigma\bar{v}t$. If the background gas has a density of n_v particles per unit volume, then the number of collisions after a time t will be

$$\text{collisions} = n_v\sigma\bar{v}t. \qquad \text{Equation 1.9}$$

We are frequently interested in distance travelled by a particle between these collisions: the mean free path. This may be approximated by the number of collisions divided by the length of our test cylinder, or

$$\text{mean free path} \cong \frac{\bar{v}t}{\sigma n_v \bar{v}t} = \frac{1}{\sigma n_v} = \frac{1}{4\pi a^2 n_v}. \qquad \text{Equation 1.10}$$

For reference, the mean free path for N_2 at atmospheric pressure is $\sim 6 \times 10^{-8}$ m [7], so at atmospheric pressure we can expect plasmas to be highly collisional.

1.2.3 Charge acceleration

The most significant (non-collisional) force on charged particles in a plasma is the electrostatic force. In general, for a particle with charge q in electric and magnetic fields $\vec{\mathbf{E}}$ and $\vec{\mathbf{B}}$ respectively, this force is given by

$$\vec{\mathbf{F}} = q(\vec{\mathbf{E}} + \vec{\mathbf{v}} \times \vec{\mathbf{B}}). \qquad \text{Equation 1.11}$$

In practice, the electric field is produced by the electrodes, which are held at various potentials V by our power supply. The corresponding electric field is given by

$$\vec{\mathbf{E}} = -\boldsymbol{\nabla} V \ (\mathrm{V/m}), \qquad \text{Equation 1.12}$$

though this may become quite complex, depending on the device geometry and the creation of space charges once the plasma ignites. For plasmas with small currents without external magnetic fields, we may assume the force on a charged particle simplifies to $\vec{\mathbf{F}} = q\vec{\mathbf{E}}$. From this expression we see that positive and negative charges are accelerated in opposite directions: positive ions are pulled towards the cathode, and electrons toward the anode. However, it is not immediately obvious how this is relevant to the discharge before we have ionization, as the electrostatic force does not act on the abundant neutral particles. In practice, we tend to have some free charge available from background ionization, such as that caused by cosmic rays. When potential is applied to the plasma device, these existing charges accelerate due to the electrostatic force, picking up energy according to

$$\mathrm{W} = \vec{\mathbf{F}} \cdot \vec{\mathbf{r}} = \mathrm{q} \cdot \Delta \mathrm{V}, \qquad \text{Equation 1.13}$$

where $\vec{\mathbf{r}}$ is the vector describing the displacement of the charged particle, and ΔV is the potential difference between the ends of $\vec{\mathbf{r}}$.

Let us consider the motion of electrons for the sake of this discussion; the behavior of cations will be quite similar in the opposite direction, though velocities are much smaller for these heavier particles. Along their path to the anode, the electron collides with neutral particles. While the energy is low, these collisions tend to be elastic. As the accumulated energy reaches thresholds sufficient to produce excitation and ionization of the neutrals, however, energy begins to be transferred to the neutral gas.

1.2.4 Electrical breakdown

In its earliest stages, prior to proper ignition, very little current is carried between the electrodes due to the scarcity of charge carriers. There are two primary sources of electrons in the discharge: volume ionization (produced by ionizing collisions in the gas) and cathode emission. Electrons are ejected from the cathode when it is impacted by a cation with sufficient energy to eject secondary electrons. This can be a substantial source of electrons in the discharge, and is one of the contributing factors to the stability of microhollow cathode discharges, described in §1.3. As the electrode potential is increased, electrons can produce more ionizing reactions before they reach the anode, and cations are able to eject more electrons from the cathode. Ignition of the plasma occurs when free electrons are being produced faster than they are being lost to attachment and recombination. The potential at which this condition is met is called the breakdown voltage of the plasma. Paschen [8] produced an empirical model for this breakdown point as a function of the gas pressure p and electrode separation d, given approximately by

$$V_b = \frac{bpd}{ln(apd) - ln[ln(1 + 1/\gamma)]} = f(pd), \qquad \text{Equation 1.14}$$

where a and b are constants which must be experimentally determined for a range of plasma operation with a particular gas composition. γ, the secondary emission coefficient, depends on the cathode material, and is defined as

$$\gamma \equiv \frac{\#\text{ of electrons emitted}}{\#\text{ of incident ions or photons}}. \qquad \text{Equation 1.15}$$

The Paschen curve, as the plot of this relationship is known, is pictured in Figure 1.4.

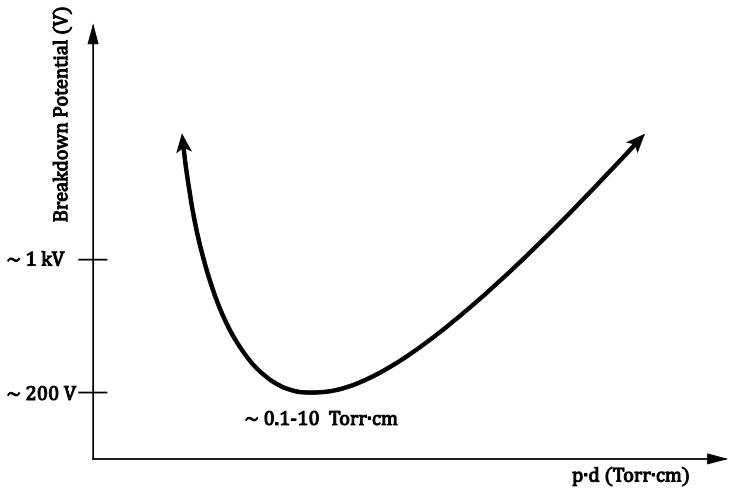

Figure 1.4 Schematic of the Paschen curve. For Ne discharge, the observed minimum occurs $\sim 10^{-1} - 10^{1}$ Torr $\cdot$ cm.

The Paschen law holds fairly well in a variety of settings, but small deviations are abundant. It has been observed that significant variations from the Paschen minimum occur for small-scale devices [9], and additional inflection points have been found in Ne discharges [10] near the curve minimum. Notably, different plasma configurations, such as hollow cathode discharges, may display breakdown voltages below this limit [11].

1.2.5 Discharge modes

As the breakdown progresses, current increases and the rates of electron and photon production increase accordingly. There are distinct changes in the plasma as current is varied, corresponding to changes in the spatial and energetic parameters of the plasma. These regimes are called modes, and plasma conditions in these modes may differ substantially from one another.

Low pressure discharges, which have been studied much more extensively, will serve as a model as we study more recent microplasma devices. The same basic principles apply, though the specific transition parameters may vary. Figure 1.5 shows the major regime changes that occur as discharge current increases in a low-pressure DC plasma.

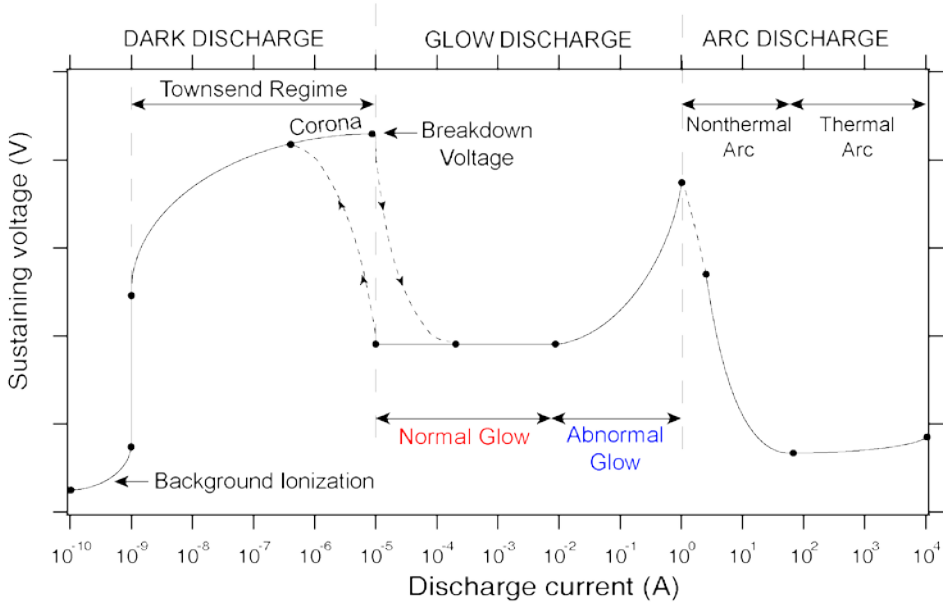

Figure 1.5 Schematic of the modes observed in a low-pressure DC discharge. The MHCDs reported in this work operate in either the normal glow or abnormal glow regime. (Adapted from [7])

The Townsend regime is a pre-breakdown state, and so this is "dark" discharge (*i.e.*, very little emission), though some ionization and recombination is taking place. This mode is not useful in our application, as the amount of radiation is very small. After breakdown occurs, we enter the normal glow regime. In this mode, current density stays roughly constant, and as current increases the plasma expands laterally until the cathode surface is covered by the discharge.

Figure 1.6 illustrates this scenario for an example device with parallel electrodes, each with some area. For the following discussion, let us assume the electrodes are larger than the ends of plasma slab pictured. The glow discharge may be approximated by a resistive volume (with bulk resistivity ρ and conductivity σ).

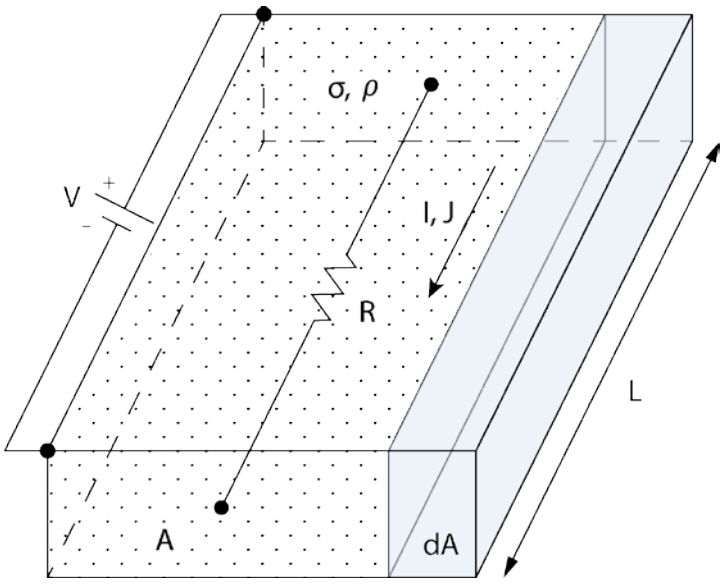

Figure 1.6 A "plasma slab" model for a glow discharge of length L between two parallel electrodes. In the normal glow mode, we consider the cathode area to be greater than A. As discharge current increases by some amount dI, the extra current is carried by a lateral addition to the plasma with cross-section dA. (Adapted from [7])

If the total current carried by the discharge is I, current density J in the slab is given by

$$J = \frac{I}{A}\ (\mathrm{A/m^2}),$$ Equation 1.16

and A is the cross-sectional area of the slab. The electrical bulk resistivity ρ is found from the total resistance R by

$$\rho = \frac{RA}{L}\ (\Omega \cdot \mathrm{m}).$$ Equation 1.17

The electrical conductivity is the inverse of resistivity:

$$\sigma = \frac{1}{\rho} = \frac{L}{RA}\ (\Omega \cdot \mathrm{m})^{-1}.$$ Equation 1.18

In the normal glow discharge mode, as the total current increases, the current density remains roughly constant. This requires the plasma cross section to increase, spreading across the cathode. Consider a filament, or section of this slab with total length L and cross section dA. We can see that as A increases, more filaments of resistance dR are added in parallel, which decreases the total resistance R. This results in a roughly constant sustaining voltage in this mode, even as current rises. In the abnormal glow mode, the cathode has been completely covered by the plasma and all increase in current must come at the cost of increased current density, which requires increasingly high voltages to drive charge carriers through the discharge at a higher rate. This leads to a positive correlation between sustaining voltage and current in the abnormal glow regime.

1.2.6 Organization of a discharge

A charged particle's kinetic energy increases as it is propelled along a line of electric field by the electrostatic force. Inelastic collisions, which reduce kinetic energy, are only accessible by charge carriers that have sufficient energy to excite or ionize their collision partners. Since these charges must travel some distance through the accelerating potential to take part in these inelastic collisions which produce the glow discharge, it is

apparent that the active regions in a plasma will have a spatial dependence. This leads to distinctive spatial structure in plasmas, and the formation of various regions with very different local conditions. Plasmas glow only in regions where the particles have sufficient energy to produce excitation. Charged particles lose energy after these exciting inelastic collisions, and where the energy distribution dips down below that threshold, another dark area appears. This is the simplest model for such a discharge, and it should be noted that other emissive and dark regions are sometimes visible in low pressure plasmas under specific conditions.

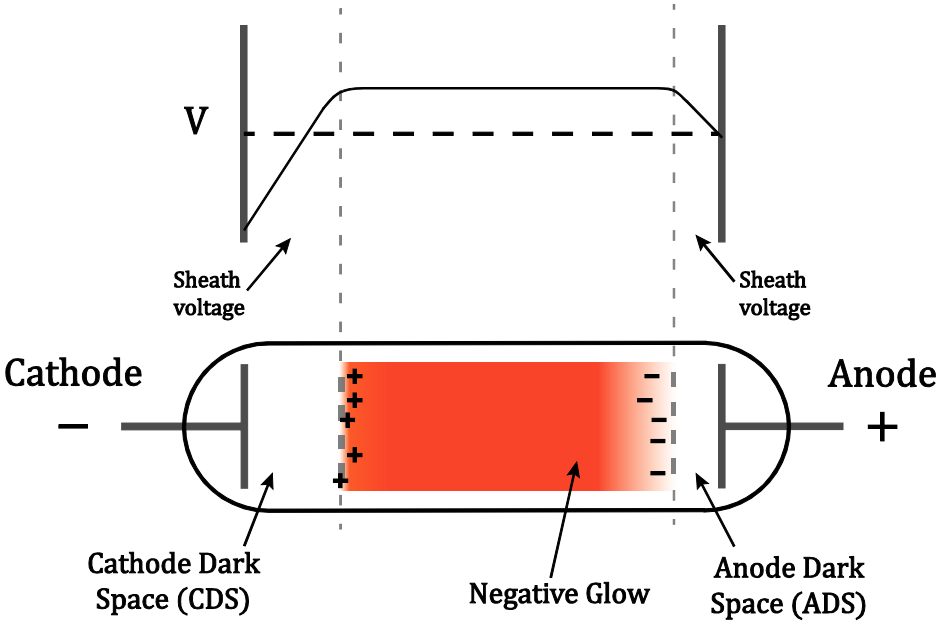

Figure 1.7 A simplified schematic of the regions in a glow discharge and the potential change across the discharge. The negative glow is basically field-free; electrons accelerated from the CDS produce emission in this region and lose energy through inelastic collisions as they travel towards the anode. (Adapted from [7])

Figure 1.7 sketches the distribution of potentials in the DC plasma discharge. This diagram specifically represents the special case of an “obstructed discharge,” a case of

abnormal glow which may occur when operating a plasma at pd values to the left hand side of the Paschen curve minimum. Still, the major features are similar for a normal glow: in the cathode dark space, charges are accelerated by the strong electric field until they have sufficient energy to ionize and excite neutrals in the negative glow region. These liberated charges produce a quasi-neutral plasma which extends towards the anode. This continues until the electron energy has mostly dissipated, producing the second dark region. The cathode dark space is sometimes referred to as the "cathode fall" region, and this part of the plasma plays a critical role in the behavior of the device as a radiation source. This region has the highest electric field in the discharge, and is responsible for the acceleration of electrons, the most important species for producing high-energy emission. Device configurations that produce a high potential difference across the cathode fall region will make useful sources of high energy radiation.

1.2.7 Hollow cathode discharges

If the planar cathode is replaced by a cathode with a cavity, such as a slit or cylindrical hole, the current observed in the discharge at the same potential is much higher than for the simple planar device. This effect was discovered by Paschen and dubbed the hollow cathode effect [12]. In hollow cathode discharges (HCDs), as with other types of discharges, the specific dimensions, materials, gas compositions and pressure ranges will vary plasma properties, which make laws that accurately describe plasma behavior in this mode more elusive. There are several effects contributing to enhanced properties of HCDs compared to their planar counterparts [13], the most important of which are described below.

1.2.7.1 The Pendel effect

Due to the cylindrical symmetry in this geometry, electrons emitted from the cathode may travel across the diameter of the "hollow" and again meet a cathode interface. If an electron still has energy after traversing the negative glow, it will effectively be reflected by the cathode fall on the opposite side. This sends it back into the negative glow where it may continue to produce ionization and excitation. This efficient recycling of electrons in the discharge significantly enhances the energy of the electron distribution [14-15].

1.2.7.2 Contraction of the cathode dark space

It has been observed that operation in the hollow cathode mode produces a thinner cathode dark space compared to planar configurations [13]. The energy gained by an electron traveling through this region is still limited by the total potential drop across the sheath, but the shorter distance reduces the collisional losses, as the path length before reaching the glow is decreased. This effectively makes the electron heating process more efficient, and contributes to the higher electron energies found in hollow cathode discharges.

1.2.7.3 Enhanced cathode effects

The cathode-on-both-sides geometry that gives rise to the Pendel electron effect also produces an ion-based phenomenon. Since positive ions leaving the negative glow region may encounter the cathode in multiple directions, the probability that they are able to impact the cathode and produce secondary electron emission is increased.

Another analogy exists for positive ions as a result of the thinning of the cathode dark space in HCDs: since the number of collisions with neutrals will be reduced as the

path length in this region decreases, cations will reach the cathode with higher energy in the same way electron energy is enhanced.

1.2.8 Paschen scaling → microplasmas

The range of plasmas varies in spatial and temporal extent by many orders of magnitude, from RF microplasmas to interstellar fields. The scaling relationship between plasmas of different sizes, as suggested by the Paschen law, is central to our work. If we may remain in the minimum of the curve by maintaining a constant pd value, then by reducing our electrode geometries, we enable operation of the plasma at higher (atmospheric) pressure. This is a convenient pressure regime for experiments like ambient mass spectrometry.

1.3 Application of microplasmas

As we have discussed, microplasmas can be a useful tool for analytical applications, and their simple operating requirements lend them towards future applications. Perhaps unsurprisingly, the ease with which one can make and use these devices has led their implementation to outpace our fundamental understanding of these devices. Kushner *et al.* [4-5, 16] have made progress in the theoretical study of these devices, but a disconnection between this community and many of the groups applying microplasmas in novel contexts remains. The problem on the experimental side is twofold: first, great care must be taken to ensure comparison of equivalent devices, and this requires extra control and measurement that are simply not necessary for many (if not most) applications. Second, such experiments are difficult to perform. As a result, there is

a shortage of data necessary to provide the groundwork for comparison to theoretical models.

1.4 MHCDs

Microhollow cathode discharges (MHCDs) are a type of microplasma device that are useful for applications where simple, stable operation and low power and gas requirements are desired. These devices are similar to hollow cathode discharges, their larger analogues, and share many of the same desirable properties as a source of radiation. The basic configuration of these devices consists of two conductive electrodes (an anode and a cathode) separated by an insulator. This may be an insulating material or a spatial separation. The electrodes may have a variety of two- or three-dimensional shapes, though as the name implies, they are set apart from other glow discharge configurations by the presence of a cavity in the cathode surface. Anodes may be arbitrarily shaped in these devices. For planar electrodes, such as those used in this work, the cavity is a simple hole in the cathode plate, but for three dimensional cathodes this hole may be blind (one-ended) or continue through the material.

In this work, we employed a device that is basically planar: three layers, consisting of two electrodes on opposite sides of an insulator, were stacked together. A hole through each layer permitted a gas flow to pass through the device. Within the cavity, the plasma was ignited by the voltage between the anode and cathode, and the radiation and energetic particles created in this discharge were used in a variety of experiments described later.

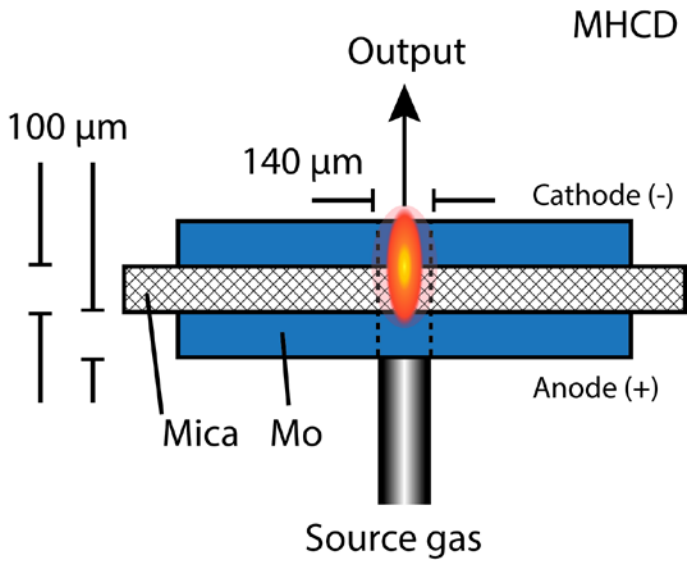

Figure 1.8 Schematic of a microhollow cathode discharge (MHCD). Depicted here is the particular foil-based MHCD described in §2.1.2.

1.5 Ionization processes in mass spectrometry

The mass spectrometry experiments performed in this work analyzed samples in positive ion mode: only cationic samples were detected by the mass spectrometer. There are a number of ways in which these positive ions may be produced.

1.5.1 Electron ionization

Electron impact ionization may produce ions through a variety of sample interactions. Those producing positive ions are listed in Table 1.2. The first case listed is the most favorable, as it produces a simple ion from the sample molecule without fragmentation. The notation used is commonly simplified ABC = M when we are primarily interested in mass spectrum peaks corresponding to the full sample ion (or adducts of this ion), as smaller fragment ions may be harder to identify in complex spectra.

Table 1.2 Electron impact processes producing positive ions

Reaction ($ABC + e^- \rightarrow$)	**Process**
$ABC^{+\bullet} + 2e^-$	Ionization
$ABC^{2+} + 3e^-$	
$AB^+ + C^\bullet + 2e^-$	Dissociative ionization
$A^+ + BC^\bullet + 2e^-$	
(etc.)	
$AC^+ + B^\bullet + 2e^-$	Dissociative rearrangement
$B^+ + AC^\bullet + 2e^-$	
(etc.)	
$AB^- + C^+ + e^-$	Ion-pair formation (rare)
$A^- + BC^+ + e^-$	
(etc.)	

1.5.2 Chemical ionization

Table 1.3 Chemical ionization processes producing positive ions [17]

Reaction	**Process**
$M + [BH]^+ \longrightarrow [M + H]^+ + B$	Proton transfer
$M + X^+ \longrightarrow [M + X]^+$	Adduct formation
$M + X^+ \longrightarrow [M - H]^+ + HX$	Hydride abstraction
$M + X^{+\bullet} \longrightarrow M^{+\bullet} + X$	Charge exchange

Chemical ionization pathways are prevalent in ambient mass spectrometry. At atmospheric pressure, charged and energetic species undergo a number of collisions with neutral sample and background molecules. Where chemical reactions are favorable, as in the donation of a proton to a molecule with a higher proton affinity, such transfers are likely to occur. This process is often “softer”, *i.e.*, results in less fragmentation of the sample molecule, compared to electron impact ionization. Consequently, this is a favorable method of ionization in many applications.

1.5.3 Penning ionization

Glow discharges are rich sources of electronically-excited neutrals. Such energetic states often undergo spontaneous radiation before they have a chance to perform chemical reactions. However, certain energetic states with long lifetimes, such as high-angular-momentum states that may not decay in one step due to quantum mechanical selection rules, may form in the plasma. These states are known as metastables, and are powerful reaction agents in mass spectrometry. Simply put, these energetic neutrals (particularly noble gas atoms) store energy until it can be released in a collision with a sample or background molecule, producing ionization. The reaction mechanism for Penning ionization is given by

$$A^* + M \rightarrow A + M^{+\bullet} + e^-. \qquad \text{Equation 1.19}$$

1.5.4 Photoionization

Photoionization, or more specifically single photon ionization (SPI), is a simple ionization process in which a photon strikes a particle and carries enough energy to eject an electron. In SPI, VUV light sources (with photon energy of ~10 eV) provide enough energy to liberate the electron and produce a positive sample ion, but typically the photon energy is only slightly above this threshold. Compared to other ionization processes, such as electron impact (EI) ionization, SPI has the advantageous characteristic of leaving sample molecules largely intact. This is a result of a lack of excess energy in the interaction which might be delivered to a sample molecule.

1.6 Final thoughts

When we began this project, microplasmas were gaining popularity as potent energy sources that could be produced at low cost and operated at atmospheric pressure. MHCD sources had not yet been used for ambient mass spectrometry, and we set out to develop and adapt this technology to fill this role. In the course of our work, we discovered ways to enhance the capabilities of this source, but simultaneously encountered challenges of control and reproducibility. Addressing those issues led us to develop an elaborate control system which could then be used for more careful study of the properties of these devices. There are a wide variety of microplasmas in use in the literature, though these various configurations often elude direct comparison due to their sensitivity to small design details. It is necessary, therefore, to provide as much supporting characterization as possible when presenting work with a microplasma source. The following work will present the fabrication and operational details of our device, as well as our characterization data and successful applications in atmospheric pressure mass spectrometry experiments.

CHAPTER 2
EXPERIMENTAL DESIGN

2.1 Microplasma device design and fabrication

Several MHCDs were investigated, and an overview of the most successful apparatus configuration is described below.

2.1.1 Silicon-based MHCD

A successful MHCD design used in our experiments was a monolithic device constructed from a Si wafer, which was a modified version of a design by Park *et al.* [18]. This design uses a p-type silicon substrate as one electrode, with the dielectric and second electrode patterned on top. This one-piece design is an ideal configuration for field operation or commercialization, as it makes the MHCD easily replaceable and reduces the room for error in assembly. It is also an advantageous design for experiments that require a large number of devices, as mass fabrication of high-quality devices is readily achieved. However, the equipment and labor costs to prepare these devices are high at the small scales of experiment.

2.1.1.1 Design and fabrication

Using standard lithographic techniques, MHCDs were constructed from silicon wafers. The basic steps were as follows (refer to Appendix A for details):

1. 100 mm diameter, 525 μm thick, p-doped Si wafers with a 100 crystal orientation and 10-20 Ω/sq sheet resistivity. were obtained from Silicon Valley Microelectronics, Inc. (Santa Clara, USA).

2. Using plasma enhanced chemical vapor deposition (PECVD), a thin layer (7-10 μm) of SiO_2 was deposited on the top surface of the wafer.
3. A layer of photoresist (Megaposit SPR-220) was deposited on the SiO_2 layer and patterned to reveal portions of the wafer that would be etched away. These areas would correspond to the through-holes in the device. In our initial design, each device had three holes patterned into them, with 100 μm, 200 μm, and 300 μm diameters. The three holes were made to examine the effect of hole diameter on the operational characteristics of the discharge. Of these, only the 200 μm and 300 μm holes were fully developed during fabrication, and the 100 μm was sealed off during experimental operation.
4. Using plasma etching tools, SiO_2 not protected by the photoresist was removed.
5. The wafer was mounted to a carrier wafer before through-etching. In another plasma etching tool, the material removal process was continued until a hole with nearly vertical sidewalls was produced through the wafer. The high aspect ratio features are made possible by the Bosch process, whereby repeated etch and deposition steps selectively passivate the sidewalls and allow the etch to continue downwards.
6. Another layer of photoresist was added to mask MHCD device edges.
7. Metal (Ni or Al) was deposited on the masked wafer in a layer ~200 nm thick via e-beam evaporation. Due to the isotropic nature of e-beam deposition and the steep sidewalls of the wafer through-holes, this process did not typically deposit enough metal in the holes to induce electrical shorting.

8. Using a liftoff technique, the mask was removed leaving the MHCD margins free of cathode material.
9. The wafer was diced into 2×6 mm devices. Gas and electrical connections were provided through a housing which supported the device during experimental operation.

The earliest wafer-based devices utilized multiple hole diameters per device and an aluminum cathode layer. These devices, which were fabricated by another student, were used for the experiments presented in the first chapter. The process used to create these devices was not recorded. The steps described above reflect the process I developed to make similar devices. One probable difference in these two processes are in the electrode deposition step: these earlier devices likely had the Al electrode deposited before any holes were patterned. As a result, the electrode would have first been masked off and etched by a wet chemical process, and then dry etched as above to produce the deep through-holes.

It was observed that eventually these devices would fail from removal of the cathode layer via sputtering. Since only the cathode had degraded, the devices could be rehabilitated by additional electrode deposition processes in the e-beam evaporator. Ni has a lower sputtering rate than Al, so it was used as the cathode material for all refurbished devices. The e-beam evaporator minimized the rate of deposition in the plane of the device, which limited deposition inside the hole through the device. This deposition cannot be completely eliminated, however, so the cathode layer thickness

attainable through this method was limited by the fact that the radial deposition would eventually lead to internal shorting of the device.

Another difficulty with these devices was the multi-hole design. Originally, this design was chosen so that the effect of cathode hole diameter could be studied, and it was intended that the differently-sized holes could be studied individually in various experiments. In practice, such isolation of one discharge hole proved difficult and the device frequently discharged through either or both holes as the effective cathode diameter changed due to sputtering. This variation precluded any size-dependent comparisons, so a single-size device was developed for future experiments.

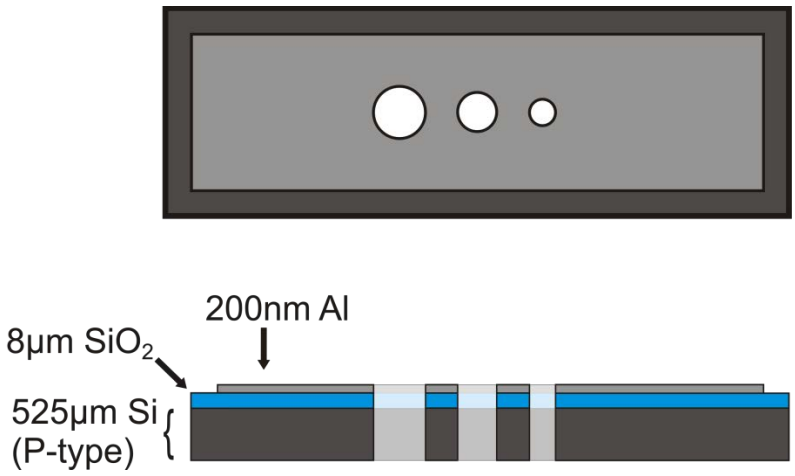

Figure 2.1 Wafer-based microhollow cathode discharge showing three discharge cavities. Original design used an Al cathode, and later changed to Ni.

2.1.1.2 Performance

The major advantages of this design are the excellent control over all dimensions, the one-piece device which obviates a complex layer alignment process during assembly, and the ability to be batch-produced.

Major drawbacks to this method are the steep requirements and initial costs to fabricate, and a lengthy fabrication process. Each wafer requires several multi-hour processing steps in cleanroom semiconductor instruments, though dozens of devices may be produced on a single wafer.

Our earliest mass spectrometry experiments (described in Chapter 4) were performed using this type of device with a relatively thin (200 nm) Al or Ni electrode layer. The low thickness led to undesirable enlargement (via sputtering) of the cathode, leading to device instability and eventual failure (inability to produce a glow discharge). This happens in any DC discharge device, as ions are continually impinging on the cathode, but without sufficient bulk in the cathode material the timescale of this failure was inconveniently short for experimental operation. Typically, the effective lifetime of this type of device was a couple of hours. The early devices had shortcomings which limited their effectiveness in the laboratory, but this design is fundamentally a good one. For any future applications on a larger scale, this is a good method for making MHCDs in an easy-to-use, tightly-controlled, mass-producible package.

2.1.2 Drilled-foil MHCD

Due to the short device lifetime and unwanted multi-hole discharge behavior observed with the early wafer-based MHCDs, a new method was sought to improve device lifetime and stability. The best of the alternative designs studied was one based on a device described by Schoenbach *et al.* [19], comprised of three individual foil layers; two molybdenum electrodes (100 μm thick) separated by a 100 μm thick single-crystal mica dielectric layer. These layers had holes drilled in them individually, and had to be

aligned after the fact, which significantly increased complexity of operation in practice. The protocol for this task is described in §2.1.3.

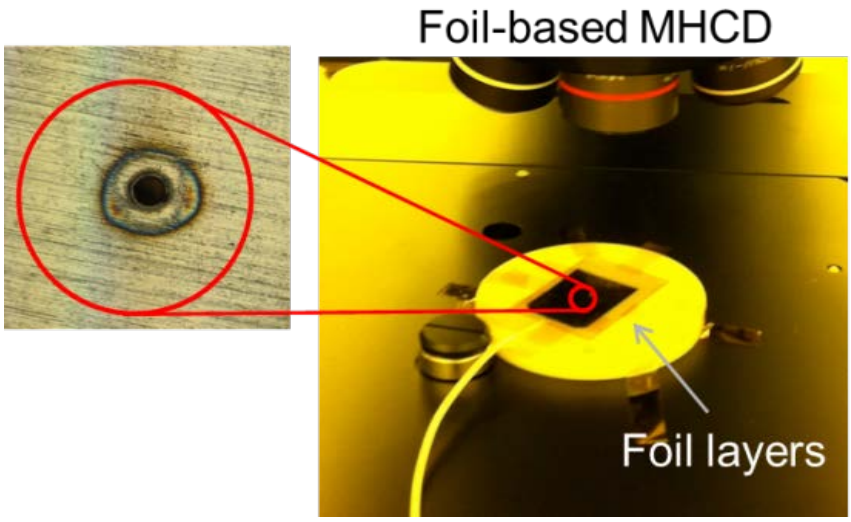

Figure 2.2 Assembly process for the foil-based MHCD. Right: alignment and inspection under an optical microscope. Detail shows cathode hole enlargement and sputtering damage after operating discharge.

2.1.3 MHCD device holder

The problem of utilizing one of these MHCD devices, once produced, is a subject of at least equal complexity. A variety of solutions were developed, the best of which is described here. The fundamental aspects of a good holder are common to any MHCD design that shares a basic layout with the planar devices used in our experiments. The essential properties are the ability to direct a gas source through the MHCD opening and to apply a voltage, without either the gas or potential reaching parts of the apparatus other than those intended. Ideally, this device allows the MHCD device to be easily replaceable. The specific dimensions of such a device are quite flexible, and are generally suited to the particular application or type of experiment that will be performed.

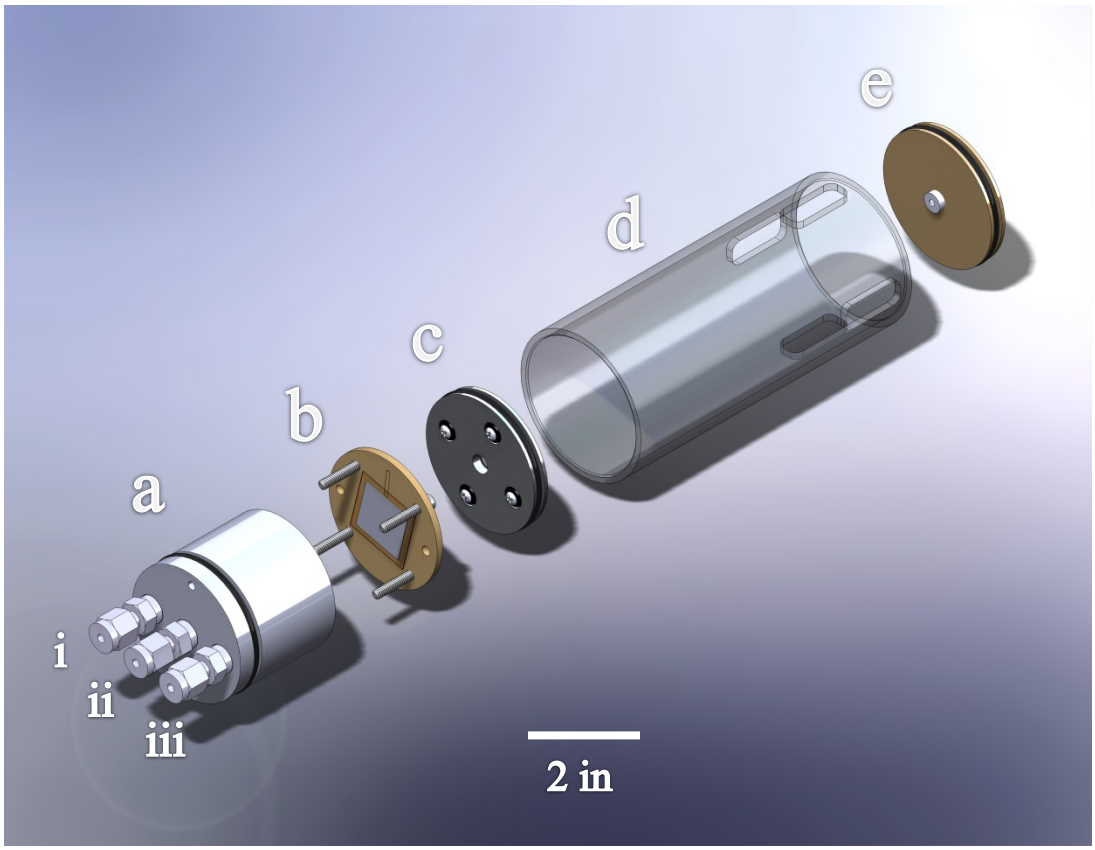

Figure 2.3 MHCD experimental assembly. (a) MHCD body, with (i) purge gas (ii) plasma supply gas, (iii) exhaust gas fittings, and (not pictured) electrical connections. (b) MHCD endcap, showing foil assembly and clamping screws. (c) LiF window with seals (d) Al housing (e) mass spectrometer inlet collar (with tip of MS capillary showing).

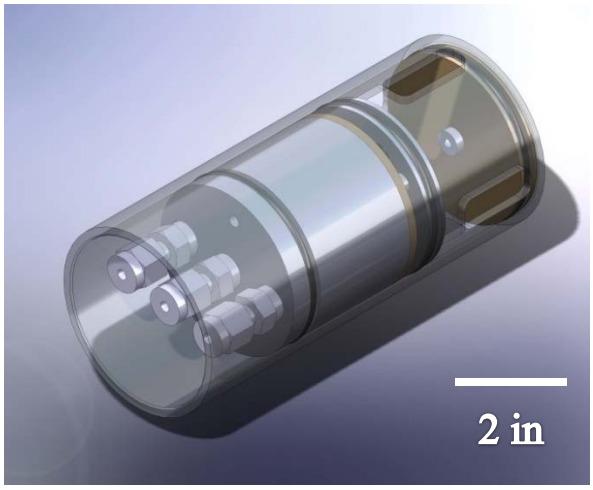

Figure 2.4 MHCD assembly shown in collapsed form (as used in experiments).

Protocol for assembling foil-based MHCD device:

1. Thread a length of thin (~75 μm) stainless steel wire through the device holder, which should be disconnected from gas lines
2. Electrically-insulating, vacuum-compatible grease is helpful to assist in gas sealing and to prevent internal shorting inside the holder apparatus. For this purpose, Apiezon N grease (vapor pressure 6.0×10^{-10} Torr at 20℃) was found to be effective. Low-volatility grease is particularly important in the course of mass spectrometry experiments. Dow Corning High-Vacuum Grease (1.2×10^{-5} Torr at 150℃) was readily observed in mass spectrometry experiments when present even in small quantities.
3. Each layer is threaded onto the stainless wire, aligning the holes
4. The high voltage wire is brought into contact with the cap, which contains a spring contact to transmit current to the front-most layer, the cathode.
5. The cap is carefully bolted on to the body of the holder, pressing the layers together and making electrical contact and making the supply gas o-ring seal. Make any final adjustments to layer position with the wire before tightening.
6. If the layers are well-aligned, the wire will be free to slide out of the device. Electrical continuity can be checked, and the hole visually inspected to ensure no blockage will obstruct gas flow.

If a monolithic device design (such as the wafer-based MHCD) is employed, the method is identical, though the wire-threading step may be replaced by any means of positioning the device coaxially with the holder.

2.1.4 Window

For experiments utilizing only the light produced by the MHCD, such as those in Chapters 3 and 5, a LiF or quartz window was employed between the MHCD and the detector. The window served as a gas-tight seal in the housing which allowed the region around the MHCD, referred to here as the "plasma chamber", to be purged or evacuated independently of the sample/detector area ("sample chamber"). This window was positioned ~10 mm from the MHCD and permitted only the photons produced in the plasma to pass into the sample chamber. Over time, the plasma would deteriorate windows, and so this flange allowed replacement of the window material when degradation was observed, and protected more sensitive components like the optical fiber from damage by the plasma.

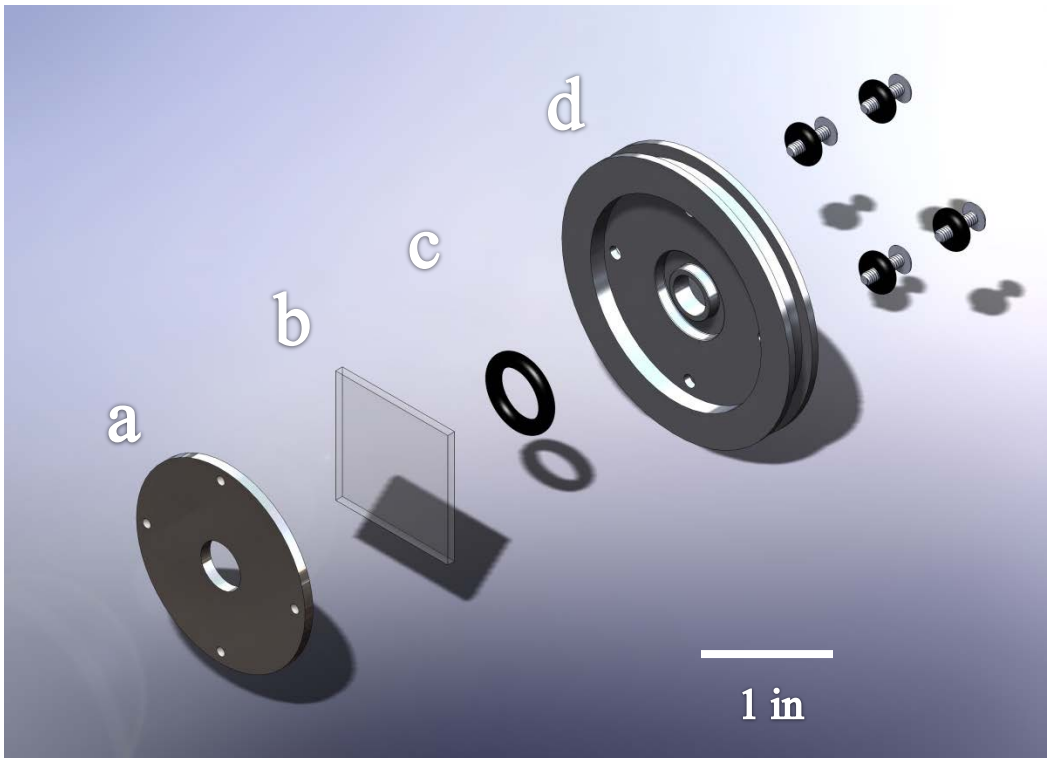

Figure 2.5 MHCD window assembly. (a) Stainless steel window clamp (b) LiF/quartz 25mm x 1 mm window (c) Viton o-ring (d) Aluminum window flange

2.1.5 Other designs

In the course of optimizing the MHCD fabrication process, a variety of devices were investigated but saw little use in other experiments. Some of them are described below.

2.1.5.1 Capillary plasma

A glass pipette tube was heated and drawn to a fine point using a propane torch. A W wire was inserted into the larger end and fed nearly to the narrow tip, and served as a anode. A strip of copper was affixed to the outside of the capillary tip, and this electrode was grounded. A piece of tubing was used to feed gas (Ne) through the larger end, and the wire had a +630 V potential applied to it. This produced a jet of plasma, similar to the flowing atmospheric pressure afterglow (FAPA) microplasma configuration in the literature [20]. This device was successfully used to demonstrate the capability of microplasma sources coupled to mass spectrometry imaging systems. This experiment was performed by drawing an "X" shape with an azulene-methanol solution on a piece of photo paper, and allowing the solution to dry. An infrared laser focused to a small (~100 μm) spot provided location-specific desorption of the azulene sample, which was scanned in two dimensions in front of and slightly below the mass spectrometer inlet. The capillary plasma was positioned above the sample and directed toward the MS, and the effluent plume emitted performed ionization of the desorbed sample plume coming off the sample. Figure 2.6 shows the result of an imaging scan depicting the $[M]^{+\bullet}$ molecular cation intensity as a function of position. Contrast in this experiment was limited primarily by the volatility of our sample, which was easily desorbed from the substrate.

Laser desorption would produce a large quantity of sample molecules in the gas phase, and thus the detected analyte signal would linger for some time after the sample had been moved.

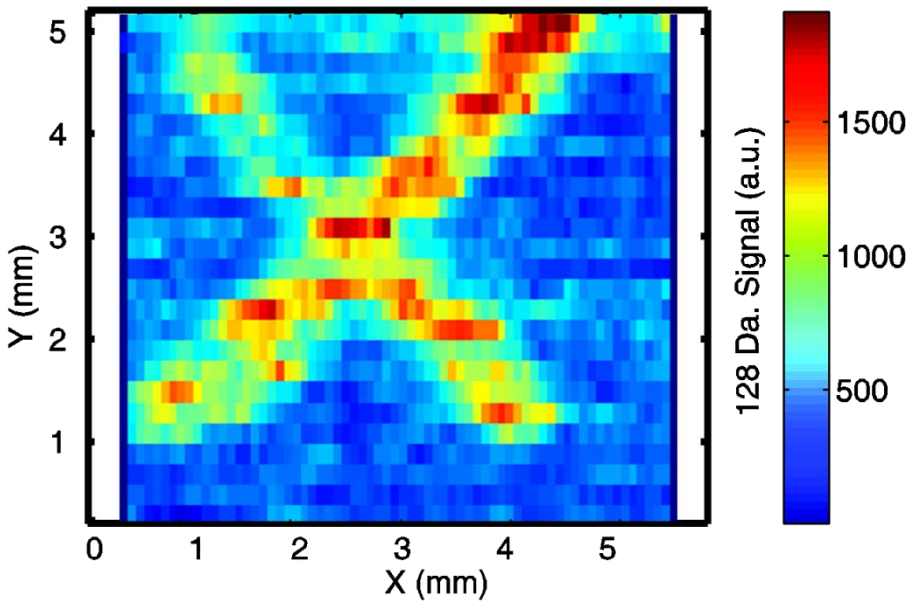

Figure 2.6 Mass spectrum image of azulene on photo paper sample, obtained with IR laser desorption and microplasma ionization.

2.1.5.2 Glass coverslip MHCD

In order to avoid a complex and costly lithography process, we attempted to make MHCDs starting with thin glass coverslips. Metallization of the cleaned glass coverslips was performed with an e-beam evaporator, and produced Ni electrodes ~300 nm thick with ~5 nm Ti or Cr adhesion layers to promote bonding to the glass. This step was straightforward, but fabrication of the hole was problematic. We attempted both mechanical drilling, using a high-speed rotary diamond cutting tool used in dentistry, and laser-drilling processes. Both caused excessive removal of the deposited electrode

material, and laser drilling (with a pulsed laser) produced jagged hole edges and small radial cracks in the glass. A few devices were intact enough to be operated, but the thin electrode material quickly separated from the glass during operation.

2.2 MHCD operation

A wide variety of experiments were performed throughout the presented work, and the specific details of those experiments are described in the relevant sections. The basic methods of operation of the MHCD device itself, however, are common to the different applications and are described in this section.

2.2.1 Electrical power

Power in these experiments was supplied by a high voltage DC power supply. For the drilled-foil MHCDs, the electrode facing the sample and/or detector was chosen to be the cathode, and operated at a negative voltage while the anode was held at ground potential. While operating the Si-based MHCD, connection to the bare Si anode was made by the aluminum housing, which for safety purposes was kept at ground potential. In this configuration the anode was facing the sample, and negative voltage was supplied to the cathode on the “upstream” side of the device.

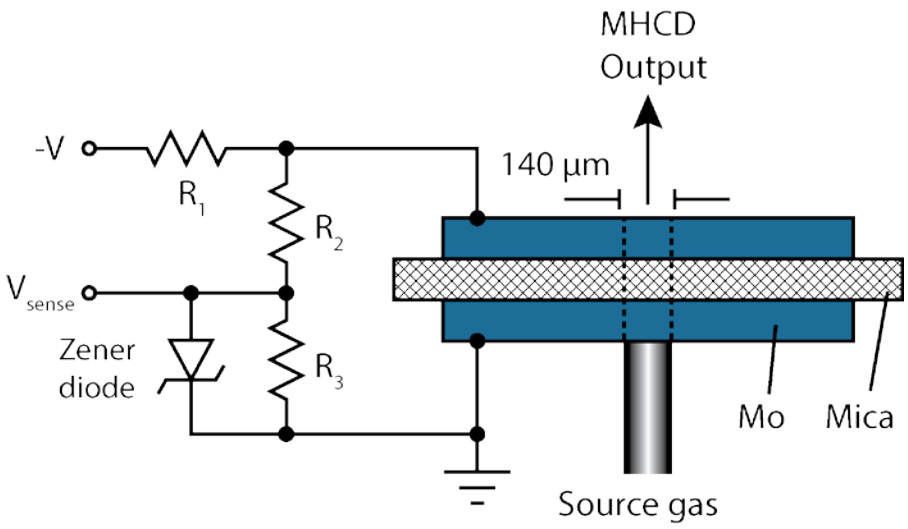

Figure 2.7 MHCD electrode configuration. R_1 is the ballast resistor, R_2 and R_3 form a voltage divider for measuring discharge voltage, and the zener diode limits the output in the open circuit condition when no plasma exists to prevent overvoltage of the sensing network.

In the operation of DC plasmas, a ballast resistor is necessary to limit current. This is a result of the mismatch between breakdown voltage (as mapped by the Paschen curve) and the sustaining voltage, which is lower. In the absence of a resistor in series with the discharge device, a DC power supply will (nominally) maintain a constant voltage output. This extra voltage drives a higher discharge current, and the discharge might transition to a different operating regime (see Figure 1.5); in the extreme case, if the voltage and current available from the supply are both very high, the plasma transitions to an arc. In that case, the plasma becomes quite hot (due to Joule heating, given by $P = I^2R$) and conductivity increases due to a high degree of ionization. There are some applications where this is desirable behavior (such as in arc welding or plasma cutting), but for our purposes we want a glow discharge, which requires limiting the discharge current.

2.2.2 Gas supply

A range of control methods have been employed to deliver gas to the microplasma device. Initially, a simple rotameter was employed with a needle valve for control. Rotameters, which are a type of variable area meter, indicate gas flow rates by allowing the viscous flow of gas to push a small sphere upwards against gravity in a graduated tube. The model used in our experiments was a Matheson FM-1050 high-accuracy flow meter. These devices come calibrated from the factory for a number of gases, or a chart of coefficients for calculating gas flow when using a non-calibrated gas. These coefficients and calibration curves are often not self-consistent, so this method is not recommended for precise measurements. Mass flow controllers (MFCs), which use thermal sensors to determine the flow rate of a gas, are less sensitive to gas pressure changes and may be more suitable for high-accuracy applications. We utilize two mass flow controllers in our experiments in order to produce final gas mixtures. Through the first (Omega model 5506), pure Ne is delivered to the MHCD. The second (Omega model 5504) is connected to a mixing manifold, where mixtures of other gases in Ne may be prepared and metered out at rates determined by the final concentration desired.

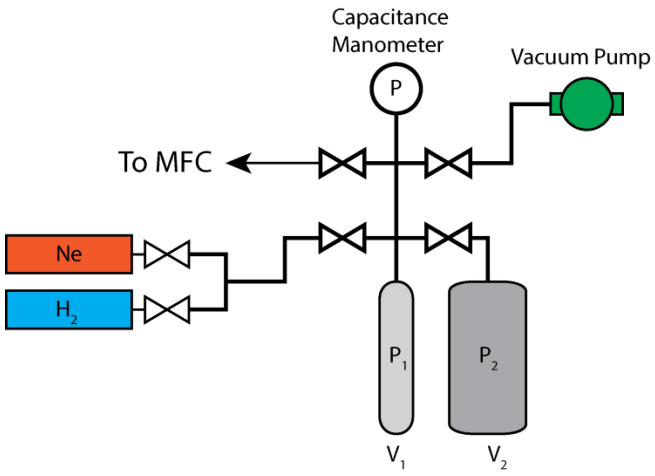

Figure 2.8 Gas mixing manifold, shown with Ne/H_2 mixture setup. Not pictured: Pure Ne MFC, which mixes with the output of the mix gas MFC displayed in this figure. V_1/V_2 = 0.026 including gas lines when the bellows valve is closed. If bottle valve is closed instead, V_1/V_2 = 0.0415 is used for mixing calculations.

Gas mixtures are prepared by filling two calibrated volumes with different gases and then allowing the gases to mix. The final concentration is determined by the partial pressure of each gas. This allows us to deliver precise mixtures of a wide range of concentrations without many different sizes of MFC, but comes at the cost of finite runtime for mixed gases. With this method, we may investigate H_2 in Ne mixtures from 0.001-8% H_2 in Ne (after dilution) with 0.01% accuracy and an order of magnitude range of concentrations available in a given experiment. The procedure for producing these mixtures is rather lengthy: refer to Appendix B for details.

When operating the plasma at atmospheric pressure, a nitrogen purge was employed to prevent atmospheric impurities (such as H_2O and/or O_2) from entering the plasma. This was found to limit degradation of the device. Control of the plasma gas supply was handled by a LabVIEW program that automatically adjusted the flow rates of

the MFCs to keep total flow rate constant while concentration was varied, and vice versa. This program also handled data recording duties for plasma parameters.

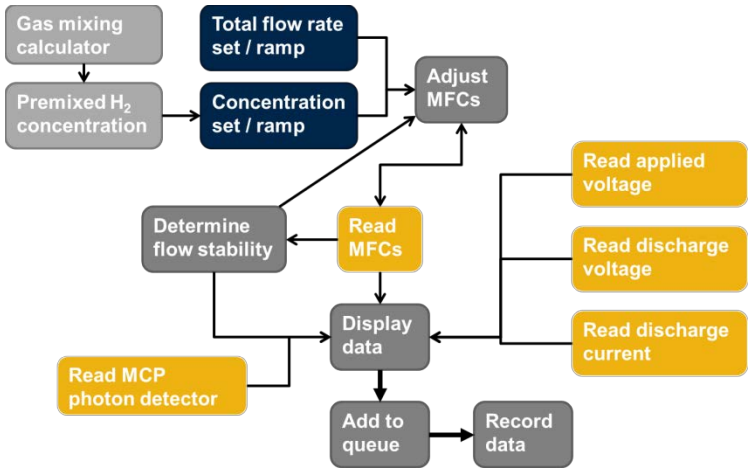

Figure 2.9 Flow chart for control of microplasma experiments with LabVIEW program.

2.3 Other instrumentation

2.3.1 Microchannel plate VUV detector

A matched pair of microchannel plate detectors was used to sense VUV radiation. The details of this experiment can be found in §5.2.4. Signals were detected through the USB 6008 (National Instruments) DAQ-based counter input after being amplified by an F-100T preamplifier (Advanced Research Instruments Corporation). The preamp in turn was connected to the MCP feedthroughs by a decoupling box, which isolated the AC portion of the signal:

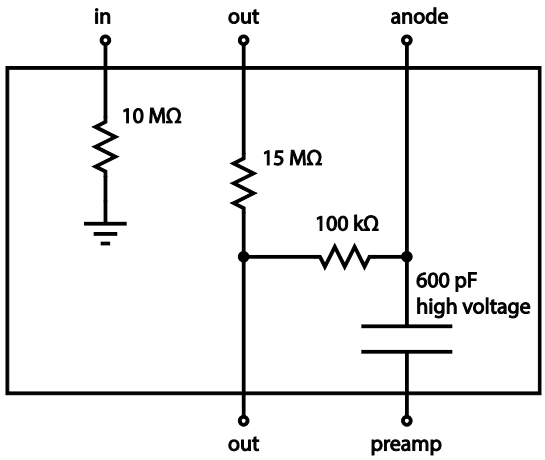

Figure 2.10 MCP decoupling box.

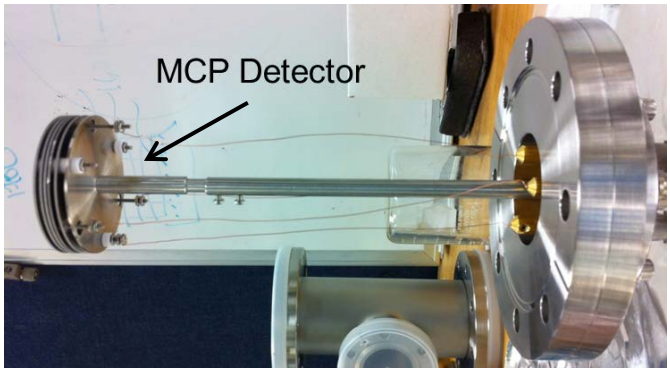

Figure 2.11 MCP detector assembly on a CF flange.

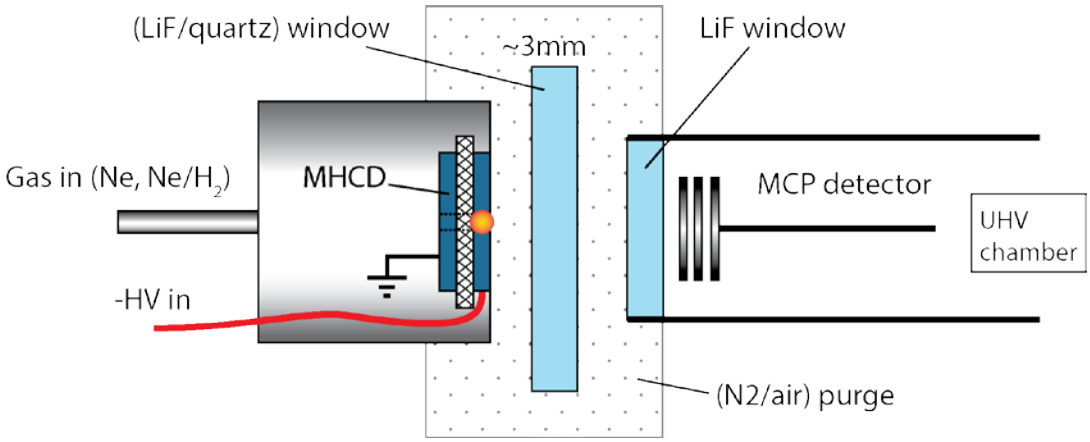

Figure 2.12 Diagram of experimental setup used in VUV transmission experiments (§5.2.4). Cylindrical aluminum housing is shown on the left with foil-based MHCD, and MCP detector is shown in UHV chamber at the right. This MHCD configuration was common to all experiments using foil-based MHCD devices.

2.3.2 Voltage sensing network

Voltage applied to the MHCD circuit, consisting of the discharge itself with the ballast resistor in series, is easily monitored by the power supply. This is the actual control parameter that the power supply adjusts in order to maintain a current setpoint. However, the more relevant discharge voltage, which is the potential drop across the MHCD, is harder to measure. Typically this measurement would be done by a voltmeter connected to the MHCD in parallel, though none of the tools typically suited for this task were capable of measuring the high voltages required.

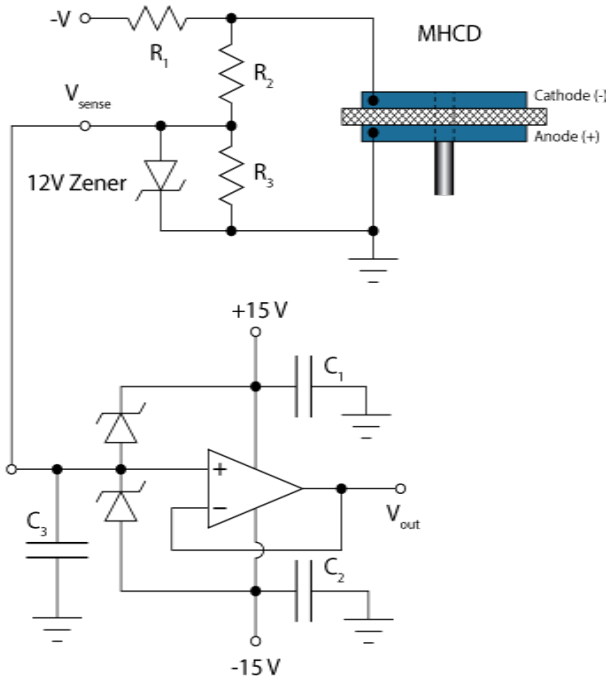

Figure 2.13 Discharge voltage sensing network. $R_1 = 97.5\ k\Omega$ (ballast resistor), $R_2 = 21\ M\Omega$, $R_3 = 560\ k\Omega$. $C_1 = C_2 = C_3 = 0.001\ \mu F$. The pictured operational amplifier is a LF 353N unit.

Using a voltage divider network is a common technique to navigate this issue, but this introduces another issue in our application. A voltage meter, or any circuit measuring

a voltage in parallel, must have an impedance much higher than the load it is measuring, to prevent appreciable current flow through the measuring device which would throw off the reading. In operation, the plasma sustaining voltage is typically in the range of tens to hundreds of volts at currents of 1-10 mA. This corresponds to an effective resistance on the order of 10-100 kΩ. In order to measure this voltage, we need to use a parallel voltage divider with resistance at least an order of magnitude higher resistance: our divider has a total resistance of ~ 22 MΩ. However, in order to read the voltage across the smaller resistor in the divider ($R_4 = 560$ kΩ), the same must again be true for the measuring device. In this experiment we read this voltage via an external computer data acquisition board (National Instruments USB-6008 DAQ), which has a fairly low input impedance of 144 kΩ, which is clearly insufficient. This requires the use of a voltage buffer (an amplifier with unity gain) which effectively transforms the impedance of the voltage signal we are trying to measure. The effective input impedance of the buffer is 10^{12} Ω. This is far greater than the 560 kΩ resistor it is measuring, and the near-zero output impedance of the buffer allows it to be read accurately by the 144 kΩ input on the DAQ. This is one of the more pedestrian aspects of our experimental setup, but it is essential to proper measurement of discharge voltage, and neglect of this detail might not be readily apparent in collected data.

CHAPTER 3
CHARACTERIZATION OF THE MHCD SOURCE

3.1 Electrical Characterization

As shown in §1.2.5, current and discharge voltage are important control parameters in glow discharges. These quantities were monitored during operation of the MHCD, and recorded in tandem with other experimental data and parameters. The discharge current and the voltage applied to the ballasted MHCD circuit are simply reported by the power supply, but measuring the actual potential drop across the plasma, which indicates the sustaining voltage of the discharge, is more useful. This requires the use of a high-impedance sensing network (described in §2.3.2), and allows us to obtain some information about the operating regime.

In §1.2.5 we showed that the relationship between discharge current and sustaining voltage allows us to distinguish between the normal and abnormal glow discharge modes. By measuring the voltage across the MHCD over a range of currents, we can measure this relationship, and by comparison determine which of these glow regimes is in operation.

3.1.1 Results and discussion

As shown in Figure 3.1, we observe a different relationship between the discharge voltage and current at different pressure regimes.

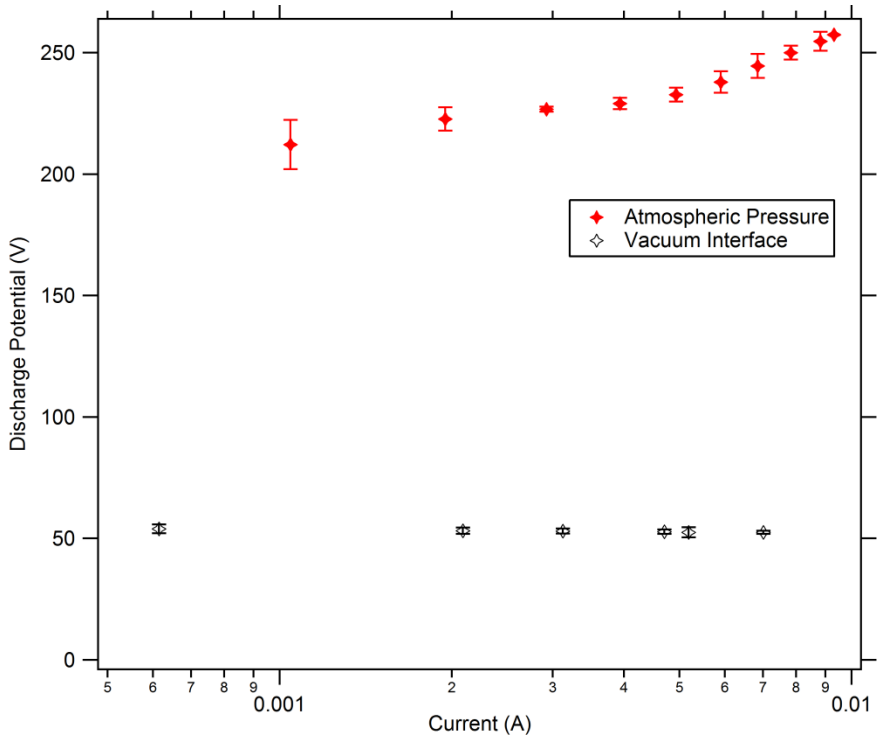

Figure 3.1 Discharge voltage vs. current for Ne MHCD, operated at atmospheric pressure with N_2 purge, and at reduced pressure.

Comparing these results to Figure 1.5, we note that the difference between these curves appear to indicate a shift in the discharge mode. For the reduced pressure operating conditions, sustaining voltage decreases as current increases, as is the case in the normal glow mode. At higher pressure, this relationship reverses, and the discharge has an apparent positive resistance.

It may be useful to compare this result to the Paschen curve. If the Paschen curve traces the breakdown voltage, drawn as a vertical line in Figure 1.5, then we may imagine lines of equal current, roughly parallel to this breakdown curve, extending along the positive y axis. As current is not a proper function of voltage in the discharge mode diagram, we cannot make a simple analogy with current vs. pressure × electrode separation. However, we may be able to draw a set of curves that correspond to each of

the mode transitions in the diagram of Figure 1.5; the point corresponding to the breakdown voltage would be the familiar Paschen curve, and a similar plot could be made for the glow-to-arc transition. In this way, we might better represent that the transitions of interest are represented as a function of V and pd than of sustaining voltage alone.

Our experimental measurements confirm this approach, and with careful control of pressure and electrode separation we might actually be able to map this out in the future. It is worth mentioning that, as the Paschen curve varies for different gas mixtures and device geometries, such a plot would also be highly dependent on the particulars of the system used to generate it. This inconsistency stems from simplifying a highly complex plasma system into a deceptively simple function of two or three variables. However, such practices are still helpful for the sake of approximation.

The result of note from the data shown in Figure 3.1 is the change in operating modes. As shown in Chapter 5, we observe significantly different behavior from the MHCD used as a photoionization source in these two pressure regimes. From these data, we may be inclined to attribute the difference in performance to this change in discharge modes. However, the relationship is not clear. At higher discharge pressures, which may correspond to the abnormal glow discharge mode, we observe a higher discharge potential. This should translate to higher electron energy in the cathode fall region, leading to higher-energy emission. However, at reduced pressure, though the discharge is operating in the normal glow regime, the plasma itself is larger and more emissive, and so the distribution of photon energies may be dominated by the higher total output in the low pressure plasma. Alternatively, our model may be too simple: in simple planar

discharge geometries it has been observed that sheath thickness decreases as electric field increases in the abnormal glow, but there may be more complex phenomena at work in the case of MHCDs.

3.2 Optical Measurement of Device

Due to Paschen scaling (described in §1.2.7.1), we expect both the electrode separation and hole diameter dimensions to be important parameters in the operation of MHCDs. It is therefore important to carefully measure and control these dimensions to ensure consistency in our experiments.

The spacing of electrodes in our MHCD design is provided by the thickness of the dielectric layer. For foil-based MHCDs, the thickness of all layers is easily controlled by making these layers from larger sheets of known thickness. For wafer-based designs, the deposition rate of SiO_2 is controlled during the PECVD process, and may be measured at stages during this processing via optical film measurement tools (Nanospec Reflectometer).

In the fabrication of foil-based devices, the through-hole is drilled mechanically, which is a rapid but delicate process. As with all mechanical hole-drilling, the actual hole diameter exceeds that of the drill bit used in the operation, and so measurement of the hole is appropriate after the electrode and dielectric foils have been prepared. Measurements were taken by imaging the individual foils on an Olympus IX-51 optical microscope with a 50x objective lens before assembly of the MHCD device.

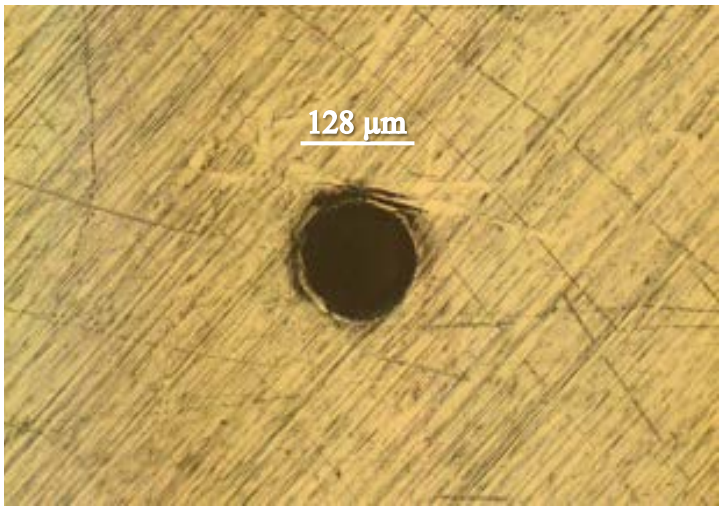

Figure 3.2 Optical image of molybdenum electrode, showing measured hole diameter.

In the following work, foil-based MHCDs had electrode hole diameters of ~100-150 µm, and dielectric hole diameters were typically ~ 25 µm larger. All layers were 100 µm thick.

3.2.1 Results and Discussion

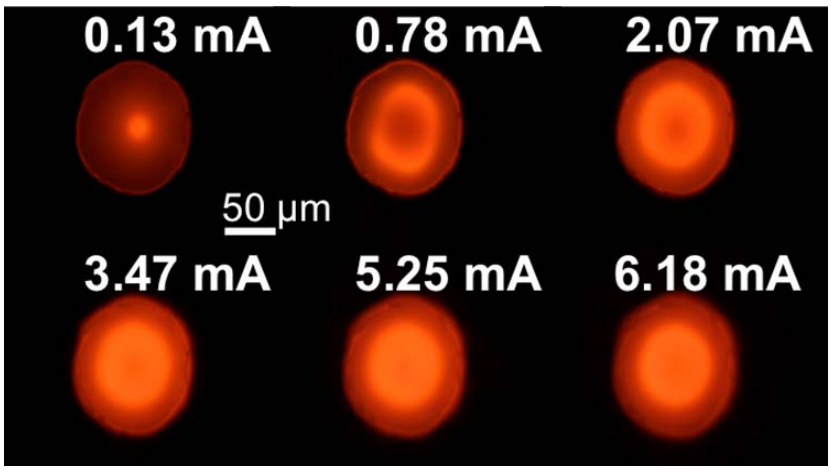

Figure 3.3 Six microscope images of the Ne MHCD. The discharge shows a mode transition from the normal to abnormal glow regime. This is consistent with our potential vs. current measurements, which indicate a discharge already in the abnormal glow mode for currents from 1-10 mA.

Preliminary attempts to characterize the discharge were performed optically under a microscope (Figure 3.3). These images show the discharge stable at a near-breakdown limit of 0.13 mA. This is probably an early normal glow discharge, which appears concentrated along the device axis due to the larger sheath thickness and incomplete coverage of the cathode. As current increases the discharge expands, we see the MHCD begin to fill in. The outer diameter does not change significantly after the image at 2 mA, which indicates that our cathode is fully covered by the discharge and has become an abnormal glow discharge by this point. At higher currents we see the center of the discharge becoming brighter, which is consistent with our results in the previous section: as discharge potential increases in the abnormal glow mode, the electrons travelling through the sheath should have more energy, and thus produce excitation further into the center of the negative glow.

3.3 Optical Emission Spectroscopy

Emission spectroscopy is a powerful tool for the analysis of plasmas. Photons emitted by plasmas reveal the energetic states and compositional identity of gases present in and around the discharge region. Using this light, we may measure the operating parameters in a non-invasive manner. Depending on the resolution of the spectra obtained, if one has a suitable model for the system one may determine the gas temperature, degree of ionization, and electron density in the plasma. Translational gas temperature may be determined by Doppler broadening of atomic lines. The temperature of vibrational and rotational modes may also be determined, in the case of diatomic gases, by fitting the data to a simulated emission spectrum.

Plasmas are inhomogeneous systems, and spectroscopic observation of individual regions allows one to fully map the operation of a discharge. In the case of larger plasma systems, such as those found in industrial plasma reactors, it may be possible and perhaps more convenient to measure some properties directly. For example, with tools such as thermocouple and Langmuir probes, one might practically measure the temperature and charge carrier density (respectively) in larger systems that accommodate the intrusion of such devices. The introduction of a physical object into a plasma will necessarily change its properties; these objects will necessarily disturb to the local electric field and impede the flow of neutral and charged particles.

However, in the study of microplasmas, the small scale of the discharge device precludes the use of most of these tools, and so spectroscopic measurement is invaluable in this application.

3.3.1 Spectroscopic measurement of gas temperature

Emission from N_2 was studied to indirectly probe the temperature of species in the MHCD plasma. At wavelengths from 500-800 nm, Ne emission dominates the emission spectrum, but from 300-500 nm most of the observed light originates from N_2 emission. The abundance of excited Ne and Ne^+ may be measured directly if the absolute intensity of the emission lines can be obtained [21]. The formula for this process (given a particular atomic transition from state m to state n) is:

$$I_{\mathrm{nm}} = \frac{1}{2\pi} n_{\mathrm{m}} A_{\mathrm{nm}} h \nu_{\mathrm{nm}} \qquad \text{Equation 3.1}$$

where I_{nm} is the radiation density ($\mathrm{W/cm^2 \cdot sr}$), n_{m} is the number density of the excited-state ions or atoms, A_{nm} is the Einstein coefficient for spontaneous emission ($\mathrm{s^{-1}}$) for a particular transition, h is Planck's constant ($6.623 \times 10^{-27}\,\mathrm{erg \cdot s}$), and ν_{nm} is the

frequency of the corresponding line (s^{-1}). The notation used here is common to absorption spectroscopy, but the constants are identical in the case of emission.

To obtain a value for temperature, one must assume a state of (at least local) thermal equilibrium. In the case of plasmas, this is not a safe assumption; different species within the plasma may have markedly different energies, and there may be additional spatial variations. However, it is often considered practical to assume a state of quasi-equilibrium where a given type of particle is in thermal equilibrium with others of that type. The justification for this assumption would be that different varieties of particles are subject to different forces within the plasma, but the energy of particles of one kind should basically follow the Boltzmann distribution. Hence, we may define separate temperatures for electrons, neutral atoms, and ions within the plasma.

If we assume the emitting atoms are in such a state of quasi-equilibrium, then using the Boltzmann equation we may obtain an expression for the temperature as follows:

$$\frac{N_m}{N_0} = \frac{g_m}{g_0} e^{E_m/kT} \qquad \text{Equation 3.2}$$

where N_m and N_0 refer to the excited and ground states, respectively, g_m and g_0 are the corresponding statistical weights, E_m is the excitation energy of state m, k is the Boltzmann constant (1.38×10^{-16} erg/K), and T is the temperature (K).

While straightforward, this method of obtaining discharge temperature was not feasible for Ne emission lines in our experiment as we do not have a reference calibration with which to deduce quantitative intensities, and so only relative intensities may be measured. As a result, instead of direct measurement of Ne, emission from N_2 was studied as a surrogate. Such a substitution is not without risk: it is reasonable to assume

that the more massive N_2 molecules, with additional degrees of freedom available for the storage of energy, may not be in ideal thermal equilibrium with the Ne atoms in the discharge. Worse yet, we are particularly interested in the energy distribution of electrons, which have been shown to have quite irregular distributions in certain parts of the hollow cathode plasma [13]. Keeping that in mind, it may still be reasonable to expect similar trends in the temperatures of neutral and charged particles. To that end, it is worth investigating the temperature of N_2 and N_2^+ in the plasma. One must maintain due reservations when extrapolating the temperatures obtained from N_2^+ cations to the electrons, but it is reasonable to conclude that, as they are subject to the same magnetohydrodynamic forces in the plasma, similar qualitative changes may occur to each as experimental parameters are varied.

However, a disclaimer is in order. Treating these measurements as temperature by fitting emission spectra to Boltzmann distributions relies on the fundamental assumption that the energy distribution follows such a distribution, which in turn hinges on the assumption of thermal equilibrium. In larger plasmas in closed volumes, such local equilibrium conditions may exist, and this model may be a good approximation. For a flowing microplasma device we have every reason to suspect that this is less valid. However, this should allow determination of some figures of merit in the plasma rather than a true temperature. This figure of merit does share some of the same qualities as a temperature. When the measured rotational temperature increases, we observe a higher number of hot rotational states in the plasma. The issue is the particular shape of the distribution: if it's not Boltzmann, it's not temperature. Indeed, there is some indication in the literature that there may be a higher-than-Boltzmann population of hot rotational

states in microplasmas [22]. In the course of this discussion I will continue to refer to the temperatures for the sake of convenience, but this disclaimer should be kept in the back of one's mind.

3.3.2 Experimental

3.3.2.1 Gas supply

We studied two pressure regimes for MHCD operation: atmospheric and reduced pressure. When operating the MHCD at atmospheric pressure, the plasma operating environment was kept free of other impurities by a N_2 purge (see §2.2.2 for details). In this case, N_2 emission was driven in two ways: the purge gas may mix into the discharge gas and be excited directly, and energetic species produced by the plasma may excite the neutral gas in the region in front of the plasma. This effect was large enough to be visible to the unaided eye; a narrow cone of bluish nitrogen emission could be seen in the region directly between the MHCD and the window used in optical emission experiments. Additionally, a small amount (1%) of N_2 was mixed into the gas supply upstream of the plasma for comparison.

Instead, when operating the MHCD at reduced pressure, no ambient source of N_2 exists (except possibly from small leaks in the seals) and so N_2 must be introduced upstream of the plasma to produce emission. The gas mixture used for measurement of temperature of the reduced-pressure MHCD was once again Ne filled with 1% N_2.

3.3.2.2 Optical spectrometer and light collection

Spectral measurements were taken on a Spex 1680 Monochromator that has been modified to enable computer control and improved performance. A US Digital model

HBA2 absolute blind-hollow-bore optical encoder was connected to the main worm gear drive in the spectrometer, allowing closed-loop position control of the gratings, which significantly improved repeatability. The photomultiplier tube was replaced with a more sensitive unit (Hamamatsu R928) with a spectral range of 185 – 900 nm, and a thermoelectric cooler housing was sourced to reduce signal noise. New control software was written in LabVIEW to take advantage of these improvements, improving scanning speed and enabling some automation of the scanning procedure. Initial wavelength calibration was performed using a Ne discharge lamp.

A new optical coupling system, shown in Figure 3.4, was designed and constructed for the spectrometer inlet. The spectrometer is set up several meters from the rest of the plasma-operating equipment, and so an optical fiber was used to direct light from the plasma experiments to the spectrometer.

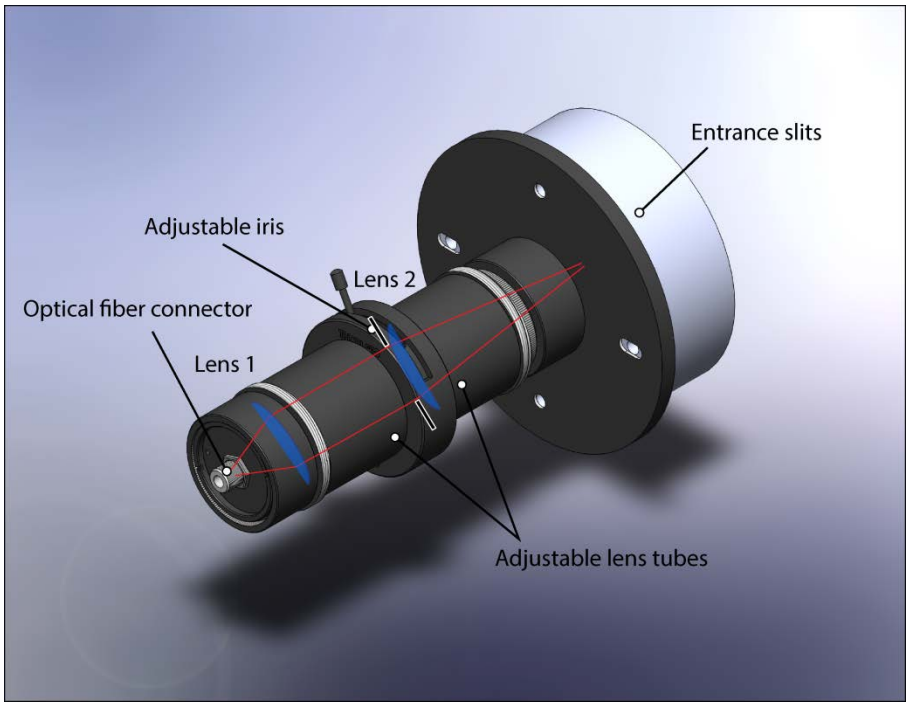

Figure 3.4 Optical fiber interface on the spectrometer entrance. The position of both quartz lenses may be adjusted to focus beam. Focal lengths: $f_1 = 35$ mm, $f_2 = 75$ mm.

The fiber assembly chosen was custom 12m fiber with SMA fittings from ThorLabs, with the same fiber core as the "solarization-resistant" (UV-compatible) ThorLabs model M19L02, which was also purchased for other experiments. These fibers are designed to retain ~50% of their original transmission rating after exposure to UV light. Both share a 200 μm step-index multimode fiber core, and permit transmission from 180 to 1150 nm. In practice, we detect limited signal below 300 nm (possibly limited by a lens in the thermoelectric cooling unit), so in future work a glass coverslip may be employed to protect the fiber from wavelengths shorter than 300 nm to extend the fiber's lifetime.

There are a few factors to consider when approaching the problem of transporting light from the plasma to the spectrometer. First, light is collected from the plasma by an optical fiber in close proximity. Light is then emitted from the opposite end of the fiber at some fixed angle. In this case, the numerical aperture (NA) of the fiber is 0.22, corresponding to an acceptance/emission angle of $2\theta \approx 25.4°$ by the following formula:

$$\mathrm{NA} = \sin\theta \qquad \text{Equation 3.3}$$

where θ is the half-angle of the acceptance cone. This must be condensed by a lens and matched to the entrance slits of the monochromator, which accepts light at f/4. F-number (or f/#) is defined as

$$f/\# = \frac{1}{2\,\mathrm{n}\sin\theta} \qquad \text{Equation 3.4}$$

where n is the refractive index at the source. This is often simplified by the small angle approximation, yielding

$$f/\# \approx \mathrm{f/D} \qquad \text{Equation 3.5}$$

Where f is the focal length of the lens, and D is the diameter of the entrance pupil. We have selected a two-lens system to collect light from the fiber and project it onto the entrance slits. The light from the fiber was collimated by a 35 mm quartz lens, passed through an adjustable aperture set to 18.75 mm diameter, and then focused by a 75 mm lens, yielding the desired F-number. The signal intensity was optimized by making fine adjustments to the position of each lens with respect to the fiber and spectrometer, but was found to be in close agreement with the predicted positions.

The entrance end of the fiber was aligned to the MHCD axis and pressed directly against a LiF window which separated the plasma region from the fiber. The window was positioned approximately 10 mm from the MHCD device. This arrangement of the fiber and source collects almost as much light as an optimal lens assembly, with fewer alignment steps. Fine-adjustment of the fiber position was performed using an XY stage and optimized by maximizing the spectrometer signal on one of the Ne emission lines.

3.3.3 Theory of fitting rovibrational temperatures to N_2 discharge spectra

The electronic transition $C\ ^3\Pi_u \rightarrow B\ ^3\Pi_g$ in N_2 gives rise to the so-called "Second Positive System" (SPS) of emission lines. This system contains very strong emission lines readily observed in most N_2 and air discharges, in the UV-visible range from 268-546 nm [23]. Using the models developed for the energy levels of N_2, analysis of the SPS spectrum is relatively straightforward, as several of the SPS transitions are observed in parts of the spectrum without overlapping lines. As described in Herzberg [24] and [25], the method for fitting rotational temperature is, with a few assumptions, as follows. We will first assume the rotational energy levels are not individually resolved (as their

spacing is finer than the ~2 Å resolution limit of our spectrometer), and so spin splitting for this system, which has a much finer structure, may be ignored. The energy of a N_2 molecule, then, is the sum of its electronic, vibrational, and rotational energies:

$$E(v,J) = E_e + E_v(v) + E_r(v,J), \quad \text{Equation 3.6}$$

where E_e is the electronic state energy, $E_v(v)$ and $E_r(v,J)$ are the vibrational and rotational contributions, where v and J are the vibrational and rotational quantum numbers, respectively. The vibrational energy level, for example, is given by

$$E_v(v) = hc\omega_e\left(v+\tfrac{1}{2}\right) - hc\omega_e x_e\left(v+\tfrac{1}{2}\right)^2 + \cdots, \quad \text{Equation 3.7}$$

or correspondingly by the "term values":

$$G(v) = \omega_e\left(v+\frac{1}{2}\right) - \omega_e x_e\left(v+\frac{1}{2}\right)^2 + \omega_e y_e\left(v+\frac{1}{2}\right)^3 - \cdots \quad \text{Equation 3.8}$$

In these equations, ω_e, $\omega_e x_e$, and $\omega_e y_e$ represent constants of the anharmonicity of the N_2 molecule. Similarly, the term values for rotational energy are given by:

$$F(v,J) = B_v J(J+1) - D_v J^2(J+1)^2 + \cdots, \quad \text{Equation 3.9}$$

$$B_v = B_e - \alpha_e\left(v+\frac{1}{2}\right) + \cdots, \quad \text{Equation 3.10}$$

$$D_v = D_e - \beta_e\left(v+\frac{1}{2}\right) + \cdots \approx 0, \quad \text{Equation 3.11}$$

where B_v is the rotational constant, and the second order constant D_v represents the influence of centrifugal force, is very small compared to B_v, and is neglected in our calculations. Note in Equation 3.10 that the rotational constant B_v is dependent on the vibrational state; in the absence of interaction between rotation and vibrational modes, this would not be so, and this term would be replaced with a constant *B*. The constants used in these calculations are found in the NIST database [26]:

Table 3.1 N_2 Constants of the SPS levels

Electronic State	Λ	E_e (cm^{-1})	ω_e (cm^{-1})	$\omega_e x_e$ (cm^{-1})	$\omega_e y_e$ (cm^{-1})	B_e (cm^{-1})	α_e (cm^{-1})
C $^3\Pi_u$	1	89136.88	2047.17	28.445	≈ 0	1.82473	0.01868
B $^3\Pi_g$	1	59619.35	1733.39	14.122	-0.0569	1.63745	0.01791

Using the equations above, emission line energies may be calculated for a range of vibrational and rotational transitions. Application of angular momentum selection rules ($J'' - J' = \Delta J = -1, 0, 1$) creates three sets of emission lines, commonly referred to as the P, Q, and R branches. The number of rotational transitions that must be considered is chosen such that all higher states contribute a negligible amount to the total intensity. This maximum value of J worth consideration increases with temperature, but for our studies, $J_{max} = 75$ was sufficient.

The next step in the process of developing a synthetic spectrum is to determine the intensity of each emission line. In the standard notation, the upper state quantum numbers are written v' and J', while the lower state quantum numbers are v'' and J''. For the sake of clarity, we will simplify our notation:

$$\text{Upper state } m = C_{v',J'} \qquad \text{Equation 3.12}$$

$$\text{Lower state } n = B_{v'',J''} \qquad \text{Equation 3.13}$$

Assuming an optically thin plasma (limited self-absorption), the intensity of a transition line is the product of the population density of excited state particles N_{m}, the emitted photon energy $hc\upsilon_{\mathrm{nm}}$, and the proportion of those emitting particles that transition per

second, given by the Einstein transition probability of spontaneous emission, A_{nm}. Thus the emitted intensity is given by:

$$I_{nm} = A_{nm} \cdot hc\upsilon_{nm} \cdot N_m \qquad \text{Equation 3.14}$$

where for a radiating dipole

$$A_{nm} = \frac{64\pi^4 {\nu_{nm}}^3}{3hcg_m} \cdot \frac{1}{2J'+1} \sum_{j'j''} \left|\boldsymbol{R}_{j'j''}\right|^2 \cdot \mathrm{q}_{v'v''} \cdot \mathrm{S}_{J'J''} \qquad \text{Equation 3.15}$$

In Equation 3.12 $\sum_{j'j''}\left|\boldsymbol{R}_{j'j''}\right|^2$ is the transition moment and g_m is the statistical weight of the $\mathrm{C}\ {}^3\Pi_{\mathrm{u}}$ state, both of which are constants. The quantities $\mathrm{q}_{v'v''}$ and $\mathrm{S}_{J'J''}$ represent the Franck-Condon and Hönl-London factors, respectively. The Franck-Condon factors are reported in the literature for this system [27], and the Hönl-London factors are easily calculated [24].

Utilizing this model for line intensities, it is useful to relate the rotationally-excited state population density to the rotation temperature by fitting this population to the Boltzmann distribution. This assumption has been verified for the population density of rotational levels in the $\mathrm{C}\ {}^3\Pi_{\mathrm{u}}$ in the SPS band [25]. The same assumption is not, in general, true for the vibrational levels, which will be considered in §3.3.3.1. However, in some cases this approximation is still made, taking a temperature over several vibrational transitions.

The population density for molecules in vibrational state v, N_v, is approximated by:

$$N_v = N \cdot \exp\left[-G_0(v')hc/_{kT}\right] \qquad \text{Equation 3.16}$$

where N is the total population. The population density for molecules in rotational state J, N_J, is given by

$$N_J = N \cdot \exp\left[-F(v', J')hc/kT\right], \qquad \text{Equation 3.17}$$

and so our final expression for emission line intensity is

$$I_{nm} = \text{Const.} \cdot \frac{\nu_{nm}{}^4}{2J' + 1} \cdot q_{nm} \cdot S_{nm} \cdot \exp\left[-F_m(v', J')hc/kT_r\right]. \qquad \text{Equation 3.18}$$

Figure 3.5 shows a sample set of synthetic emission lines, with the three branches colored individually.

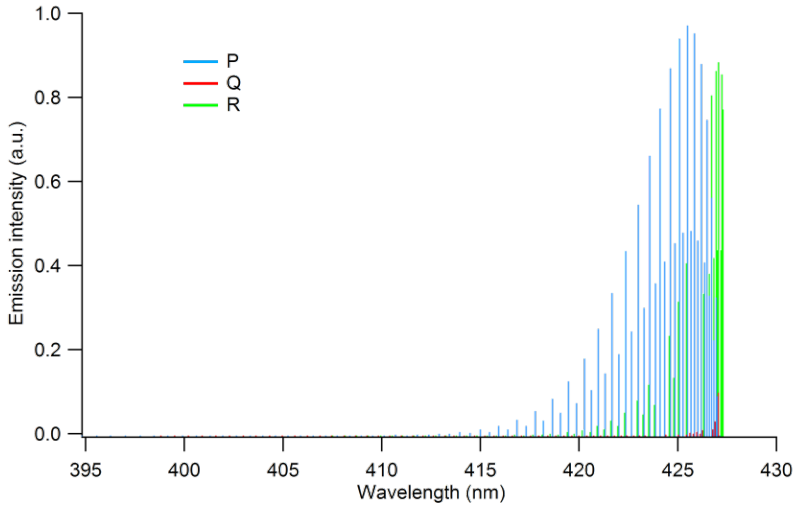

Figure 3.5 Calculated emission line position and intensities for SPS $v = 0 \rightarrow 2$ transition, showing P, Q, and R branches of emission. The P, Q, and R branches correspond to electronic transitions with $\Delta J = -1, 0, \text{and} + 1$, respectively.

Once one has obtained emission line energies and intensities for each transition of interest, the last step in forming a synthetic spectrum is to account for the finite resolution of the real spectral data: each of these discrete transitions may be treated as a Gaussian with a width reflecting the resolution limit of our monochromator. In the software developed to perform this calculation, a set of x-coordinates (wavelength values) corresponding to measured data points is used as the basis for the synthetic plot. For a single vibrational transition, the Gaussian contribution from every rotational transition in the P, Q, and R branches is combined:

$$I_{v',v''}(\lambda) = \sum_{J',J''}^{J_{max}} I_{nm} \cdot \exp\left[-\left(\frac{\lambda - \lambda_{nm}}{\Delta\lambda}\right)^2\right], \qquad \text{Equation 3.19}$$

where λ is the observed wavelength and

$$\Delta\lambda = \frac{\text{FWHM}}{2\sqrt{\ln 2}}. \qquad \text{Equation 3.20}$$

An example of this Gaussian blur of the emission lines is shown in **Figure 3.6**.

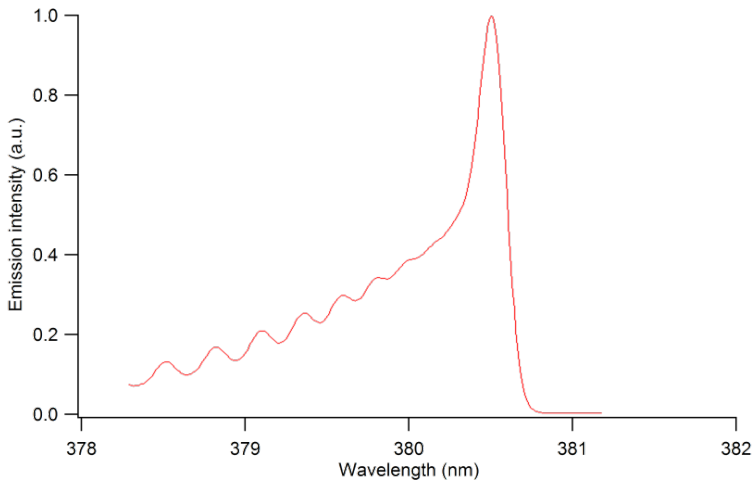

Figure 3.6 Final synthetic rovibrational spectrum for the second positive system (SPS) of N_2 emission, C $^3\Pi_u \rightarrow$ B $^3\Pi_g$, $v = 0 \rightarrow 2$.

To finally arrive at the rotational temperature, seed values were estimated for the values of T_r and the constant in Equation 3.18. The code developed optimized these parameters by minimizing the value of χ^2 when fitting the synthetic curve to the data. Using the initial guesses entered by the user, the program generated a set of alternative guesses (both higher and lower) for the two fitting parameters, and used the best fit as the new starting guesses in the next iteration, which increments in smaller steps. This process was carried out four times, and it was determined that further iterations yielded little improvement. An example result of this fitting process is shown in Figure 3.7.

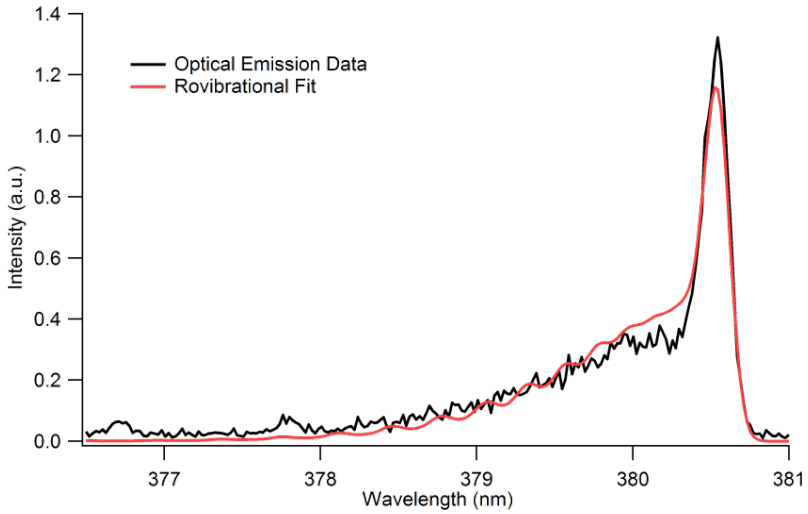

Figure 3.7 Synthetic rovibrational SPS spectrum fit to observed N_2 emission.

3.3.3.1 Vibrational temperature measurement of N_2

Software developed by Navratil *et al.* [28], Spectrum Analyzer 1.7, was used to aid in optical emission spectrum peak identification and wavelength calibration. This program also contains a subroutine to fit vibrational temperature using the Boltzmann method described in §3.3.3, and this code was employed for our measurement of the

vibrational temperature T_v. Of course, as only T_v is calculated in this way, it is worth justifying our assumption that T_r and T_v may be measured independently. T_v must be fit over multiple vibrational transitions, just as T_r is measured over many rotational transitions, but the vibrational fit may be performed without rotational considerations since only the band head maxima contribute, and these peak heights are insensitive to T_r, as shown in [25].

Conversely, a change in T_v would introduce an error to the rotational state fit, but this change will be absorbed into the constant used to fit T_r. Heuristically, this constant scales the curve as one might expect, while changes in T_r change both the slope and height (relative to the band head maximum) of the rotationally-dependent "leading edge" of the rovibrational peak. Consequently, it is possible to obtain a good fit for T_r even with an arbitrary constant, and we need not make a more complex model that simultaneously fits T_r and T_v. These temperatures were measured for neutral molecular nitrogen in a variety of conditions.

3.3.3.2 Rotational temperature measurements of N_2

As described in §3.3.3, the SPS band corresponds to the $C\ ^3\Pi_u \rightarrow B\ ^3\Pi_g$ transition of neutral molecular nitrogen. The associated rotational and vibrational temperatures correspond to the rotational energy of neutral N_2.

3.3.3.3 Rotational temperature measurement of N_2^+

The final temperature measured in our plasma was the rotational temperature of N_2^+. The so-called "first negative system" (FNS), which stems from the transition $B\ ^2\Sigma_u^+ \rightarrow X\ ^2\Sigma_g^+$, is the most easily observed emission system for N_2^+. The method for

this fit is nearly identical to the method used to measure T_r for N_2, using the constants in **Table 3.2** for the calculation. However, the process is complicated by the fact that most of the lines in the FNS band overlap with transitions in the SPS band. Consequently, the SPS spectrum must be fit in the $\Delta v = 2$ region (as performed in §3.3.3.2, and those fit parameters are used to generate a spectrum for the $C\ ^3\Pi_u(v = 1) \rightarrow B\ ^3\Pi_g(v = 5)$ transition that overlaps the $B\ ^2\Sigma_u^+(v = 0) \rightarrow X\ ^2\Sigma_g^+(v = 1)$ band we are trying to fit. Our T_r-fitting software was written to perform the SPS fit first, fix its value, and then iteratively fit the superimposed FNS line in the same fashion. As intimated previously, our lack of a simultaneous model for T_r and T_v makes this process susceptible to errors in the constant for the SPS fit, which reduces the confidence in the FNS fit. This led to increased error in our T_r measurements for the N_2^+ molecule.

Table 3.2 N_2 Constants of the FNS levels

Electronic State	Λ	E_e (cm^{-1})	ω_e (cm^{-1})	$\omega_e x_e$ (cm^{-1})	$\omega_e y_e$ (cm^{-1})	B_e (cm^{-1})	α_e (cm^{-1})
$B\ ^2\Sigma_u^+$	0	25461.46	2419.84	23.189	-0.5375	2.07456	0.024
$X\ ^2\Sigma_g^+$	0	0	2207	16.1	-0.04	1.93176	0.01881

3.3.4 Electron density measurement

Electron density in a plasma is commonly determined by measuring the degree of Stark broadening in the hydrogen Balmer-α (H-α) emission line. This broadening occurs as a result of local electric fields, indicative of local charge densities, around an emitting atom that causes splitting of degenerate energy levels. This technique may be performed using the emission lines of a variety of gases, but hydrogen emission lines are particularly

sensitive to the Stark effect, and of these the H-α line is positioned in an easily-observed part of the spectrum [29]. This method is often employed to estimate the electron density as a function of the full width of the H-α peak at half maximum (FWHM). Such formulae have a limited range of applicability. For example, one approximation [30] provides the following relation:

$$N_e(\mathrm{cm}^{-3}) = 10^{17} \cdot \left(\frac{\Delta\lambda_{\mathrm{FWHM}}}{4.8}\right)^{1.46808}, \qquad \text{Equation 3.21}$$

which the authors claim is accurate for densities as low as $N_e = 1.4 \times 10^{15}$ cm^{-3}.

3.3.5 Results and discussion

Figure 3.8 illustrates the difference between exciting nitrogen in the purge and adding it directly to the discharge gas supply. We expect to enhance the emission representative of the negative glow by adding N_2 to the plasma supply gas. As discussed previously, there will be some N_2 coming from the purge flow will be excited within the plasma, and adding N_2 directly to the discharge should increase the N_2 emission originating in the discharge. The heating of gas in this system is predominantly taking place within the plasma (following the bulk of the current flow), so we expect the N_2 emission from the discharge to have higher temperatures than the reservoir of N_2 in the neutral purge gas, which must receive its energy via collisions with species from the discharge (or other particles that have obtained their energy in this way). The 1% N_2 spectra were not fully investigated at high pressure to conserve the N_2/Ne mixture for vacuum experiments that could not be performed without it. Thus, most high pressure data reported here uses the N_2 purge as the emission source.

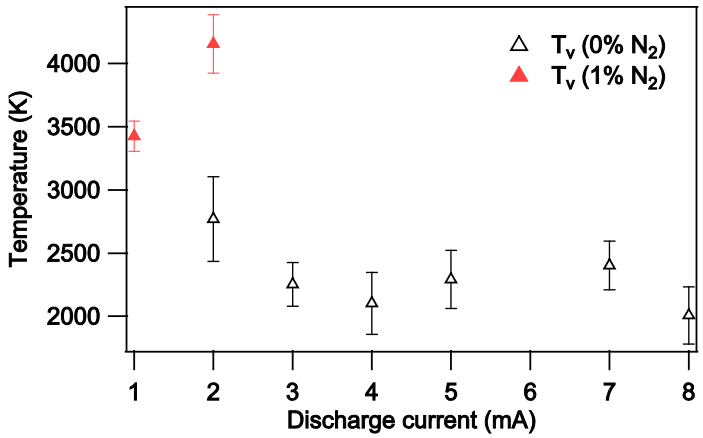

Figure 3.8 Vibrational temperature vs. discharge current for Ne MHCD with N_2 purge, showing the effects of N_2 addition to the upstream gas mixture.

In order to determine the current-dependence of the energy levels in our discharge, rovibrational temperatures for SPS emission and rotational temperature for FNS emission were measured. The results of this study are displayed in Figure 3.9.

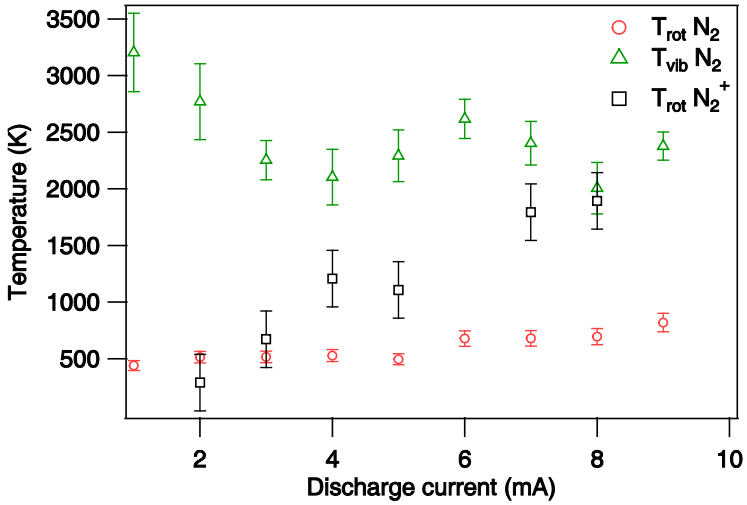

Figure 3.9 Rotational temperatures of N_2 and N_2^+, and vibrational temperature of N_2 vs. discharge current for Ne MHCD at atmospheric pressure (N_2 purge).

We observed that for the neutral N_2 emission spectra, T_r increased slightly and T_v remained approximately constant. Conversely, T_r increased with discharge current in the

case of cationic emission. Indeed, this is the only significant current-dependent trend in rovibrational temperatures that we observed in the course of these experiments. If our assumption that N_2^+ mimics the behavior of other charged species in the plasma holds, this result implies increased electron energy at higher currents. Recalling our results from §3.1.1, higher currents correspond to higher discharge potentials and thus electron energies in the abnormal glow regime, so this appears consistent. However, this correlative argument makes no attempt to describe the mechanism by which such interaction may take place. Certainly coupling of the electric field to the ionic molecule, allowing passing electrons to exert a torque on the inductively polarized structure, would have a perturbing effect on the rotational energy of N_2^+ molecules. However, it is not obvious why this might have a net effect of increasing these energy states. Another argument can be made from consideration of the excitation source in the plasma. Any emitting molecule has absorbed energy from an energetic charged or neutral particle. In this type of discharge, the electron energy distribution is typically much higher than that of other particles, and would have the strongest current-dependence of these distributions. Ions would interact more strongly with this energetic bath than would neutral N_2, and so the stronger current-dependence of T_r for N_2^+ could be explained in this way.

As for the higher values for T_r in N_2^+, a comparison of the source is again useful. If electron recombination is not dominating the discharge dynamics, then the source of N_2^{+*} is frequently N_2^+ [25], which has already been heated by its previous ionization step. Neutral N_2^*, on the other hand, most likely originated from one of the cool ground state molecules common in the gas. It could be argued, therefore, that the cooler

rotational profile of the ground state N_2 would lead to a cooler rotational profile in the excited state, leading to a systematic disparity in T_r between these two species.

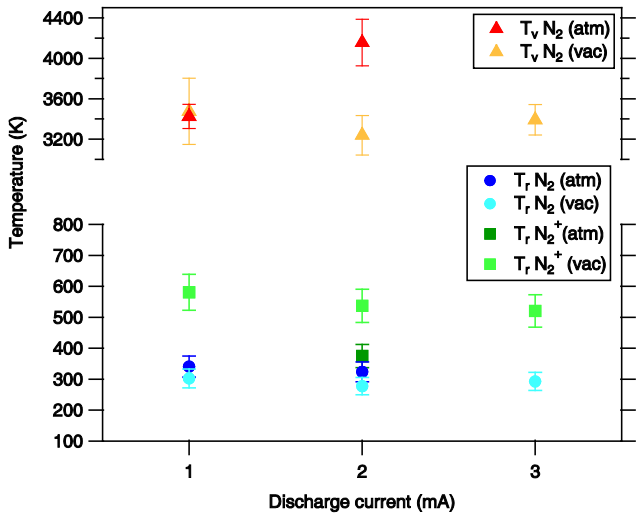

Figure 3.10 Comparison of rotational and vibrational temperatures in low pressure and atmospheric pressure operation. Ne MHCD with 1% N_2 mixed into discharge gas. Atmospheric discharge has N_2 purge in front of the MHCD, and in low pressure operation this is replaced by a rough vacuum.

Our results in §5.3 demonstrate different behavior for the MHCD when operated at reduced pressure vs. atmospheric pressure. We investigated the rovibrational temperatures of N_2 under these conditions to study temperature differences in these two plasmas. Discharge current was limited to 3 mA for the low pressure plasma, as the discharge resistance increased significantly in this mode as a result of the lower concentration of charge carriers. As shown in Figure 3.10, temperatures were fairly constant over this current range. Interestingly, the rotational temperatures for N_2^+ become slightly hotter when the pressure is reduced, and this trend is slightly reversed (or non-existent) for the neutral molecule. As described earlier in this section, we expect the ion rotational temperature to be slightly hotter than that of neutral N_2. Collisions between

N_2 and N_2^+ have thermally equalize these temperatures, pulling both distributions towards some intermediate value. At reduced pressures, the collision rate decreases, and we observe the temperatures pull away from one another.

Measurements made of the Stark-broadened H-α emission line (Figure 3.11) appear to be very close to the resolution of our spectrometer, so our electron density measurement is not practical. For a representative H-α line from our discharge (in this case, a 9 mA discharge with a 1% H_2 in Ne gas mixture), our FWHM was 0.263 nm, compared to 0.253 for a nearby Ne emission line.

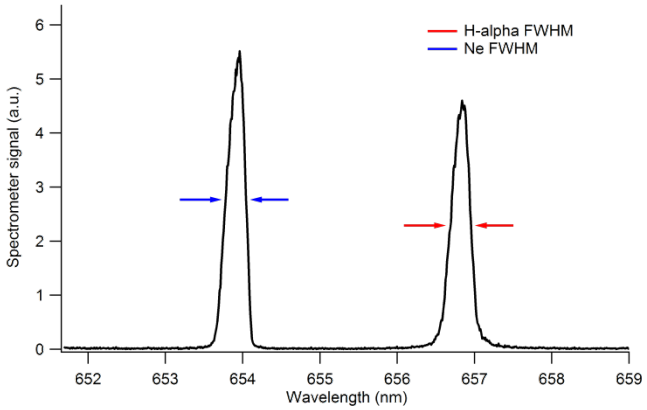

Figure 3.11 Stark broadening measurement of H-α emission from MHCD with 20 sccm flow of Ne with 1% H_2 admixture, and 9 mA discharge current. Left, Ne emission line, FWHM = 0.253 nm. Right, H-α emission line, FWHM = 0.263.

As reported by Foest *et al.* [31], typical electron densities for DC microplasmas are on the order of 10^{14} cm^{-3}, which corresponds to a peak width of 0.0434 nm, which is below our resolution for this instrument. However, Moselhy *et al.* [32] have shown the use of MHCDs in operating conditions similar to the one used in this work to produce electron densities of 10^{15} cm^{-3}, which would produce a Stark broadened width of ~0.208 nm. This width approaches the limit of possibility for detection with our instrument. When operating the MHCDs with a pulsed-DC power source, electron densities were observed

by Moselhy *et al.* to be as high as 5×10^{16} cm^{-3}, which would produce a peak width of nearly 3 nm, which should be readily apparent if an alternative power supply is configured.

3.4 Conclusions

As discussed previously, our temperature measurements are useful to describe the plasma, even if the quantities do not physically correspond to true temperatures for the species observed in the emission spectra. MHCDs are not well-understood, and so this information may be useful to the community as their applications expand. Ultimately, we would like to develop a model of MHCD operation that one could use to predict energy distributions of the various plasma species in a variety of operating conditions. This would be extremely beneficial to the work described in Chapter 5, which shows how the source may be tuned to produce different effects in mass spectrometry experiments. Further experiments are necessary to continue this characterization work. Simulation studies of MHCDs have made significant progress toward this goal [4], but theoretical studies must have experimental data for comparison. We have shown that optical emission spectroscopy may be a powerful tool to gain information about the underlying energy distributions that are the ultimate goal, even if the interpretation of such data is not trivial.

CHAPTER 4
A MICROPLASMA DISCHARGE IONIZATION SOURCE FOR AMBIENT MASS SPECTROMETRY

4.1 Overview

The first report of desorption electrospray ionization (DESI) by Cooks *et al.* in 2004 [33] triggered immense interest in further exploration of alternative "ambient" approaches for generating ions directly from sample surfaces in open air. As a result, more than two dozen other ambient ionization techniques have since been developed [34-36]. These new methods of producing ions have simplified the mass spectrometric analytical procedure, thus increasing throughput. Several of these new ambient ionization methods employ atmospheric plasmas, including direct atmospheric pressure photo-ionization (DAPPI) [37], direct analysis in real time (DART) [38], flowing atmospheric pressure afterglow (FAPA) [39], plasma-assisted desorption ionization (PADI) [40], desorption atmospheric pressure photoionization (DAPCI) [41], low-temperature plasma (LTP) ionization [42], and dielectric barrier discharge ionization (DBDI) [43]. These techniques are understood in the context of analytical chemistry. However, the physiochemical processes and mechanism(s) governing desorption/ionization are not well-understood, and remain an active area of research. Furthermore, these plasma sources typically require relatively high operation voltage and power due to their macroscopic nature, thus somewhat complicating their use in the field of portable mass spectrometry. In addition, none of the plasma-based ambient desorption/ionization techniques allow sufficient spatial control necessary to distinguish chemical features with less than a few hundreds of micrometers resolution. Approaches using laser

desorption/ionization techniques achieve better resolution, but the available ion densities are limited and the comparative costs are higher [44].

The plasma physics community has been actively engaged in developing inexpensive low-temperature microplasmas and plasma needles for industrial applications [3]. Microplasmas are weakly ionized discharges that represent a new and fascinating realm of plasma science. The "*pd* scaling" of the well-known Paschen law suggests reasonably low voltage operation of microplasma devices at atmospheric pressure for cavities of sufficiently small (< 300 μm) dimensions. The applied voltage necessary to achieve a discharge condition in these microplasmas is typically less than a few hundred volts, and the overall power dissipation is minimal compared to other discharge sources. Electrodes in these devices can be configured in a variety of ways and can be powered using DC, AC, or pulsed potentials. In the latter case, monopolar pulsed (ns) excitation leads to increased electron energy distributions while minimizing the gas temperature. When utilizing rare gases, the temperatures within the plasma are slightly above 400 K, and the metastable, ion, and electron densities typically range between 10^{12}-10^{15} cm^{-3} [45]. The efficacy of these low-temperature plasmas is driven by non-thermal processes involving direct impact ionization, inelastic ion and electron scattering, and metastable impact. Though the applications of these low-power, low-flow rate miniaturized plasma devices have been primarily geared toward device patterning in the semiconductor industry [46], their potential for optical spectroscopy and mass spectrometry applications is being gradually recognized [3]. These devices are often collectively referred to as "microplasmas" due to the different operating modes being employed with similar devices in various applications [31]. In this work, we demonstrate the first use of a

microplasma in a microhollow cathode discharge (MHCD) configuration [3, 47] as a versatile miniature ion source for ambient air mass spectrometric analysis of solid, liquid, and gaseous samples.

4.2 Experimental

4.2.1 Materials and Chemicals

All reagents and chemicals were used as received without further purification. High purity (99.9%) HPLC grade methanol and ultrapure water (18.2 MΩ cm^{-1}) obtained from a Nanopure purification unit were used to prepare all solutions. L-leucine and L-histidine were purchased in powdered form. All other chemicals, including 99.9% pure dimethylformamide (DMF), 99% pure dimethyl sulfoxide (DMSO), methyl salicylate, and caffeine powder were purchased from Sigma Aldrich Co. Over-the-counter pharmaceuticals such as Claritin® (10 mg), ibuprofen (200 mg), Tylenol® (250 mg), and Excedrin® in tablet form were purchased from a local pharmacy. The working gas used in the microplasma was ultra-high purity helium.

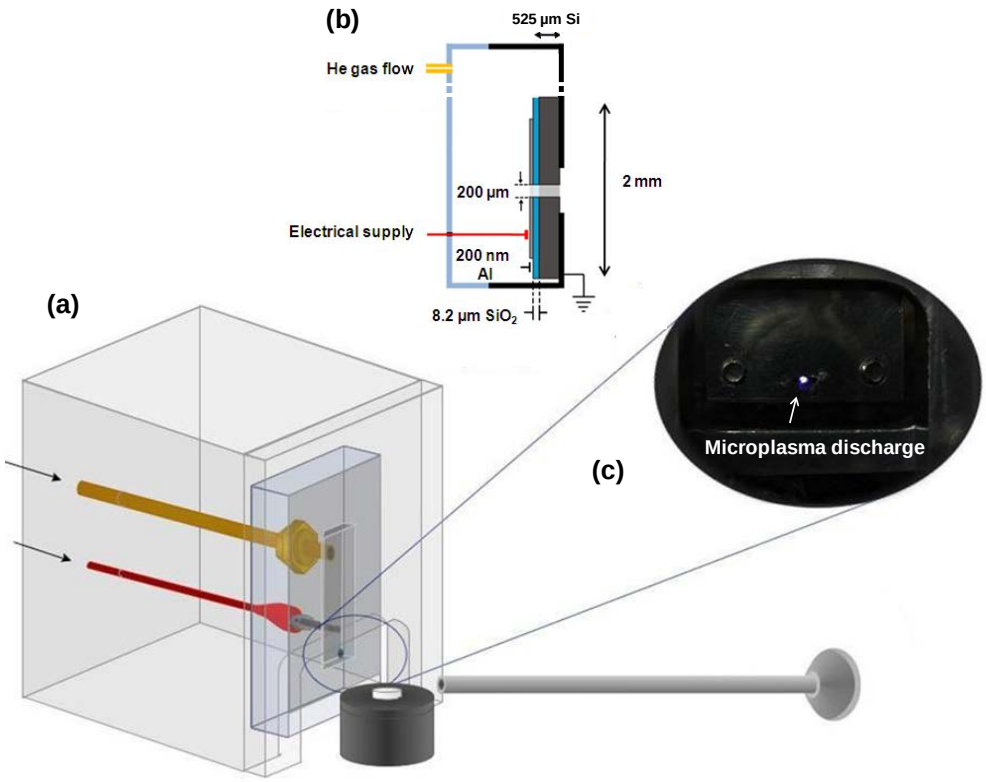

Figure 4.1 Microplasma ion source for ambient ionization MS: (a) spatial arrangement of the inlet capillary with respect to the ion source, (b) cross-sectional schematic of the microplasma chip assembly, and (c) photograph of continuous discharge observed within the chip cavity. Note that the plasma interacts with the sample directly and is incident at a 45° angle relative to the surface normal.

4.2.2 Microplasma Discharge Device

The microplasma discharge device was constructed in the MHCD configuration. The device was fabricated from a 525 µm thick, 100 mm diameter p-type silicon (100) wafer. An 8.2 µm SiO_2 layer was deposited via chemical vapor deposition (CVD) onto its polished side of the Si wafer. A 200 nm thick aluminum electrode was deposited on top of the SiO_2 layer, and a 200 µm circular opening was made through the Si-SiO_2-Al layered structure using standard photolithography and plasma etching techniques. This effectively defined the cavity where the microplasma was generated (Figure 4.1b). The

wafer was diced into 2 × 6 mm rectangles with each hole at the center of the 2 × 6 mm chip. A housing was constructed from Al and poly(methyl methacrylate) (PMMA) to mount the microplasma chip, secure electrical connectors, and direct gas flow through the discharge cavity. The discharge gas (ultra-high purity helium) was delivered at a flow rate of 0.28 L min^{-1}. The negative DC potential was applied to the Al electrode with the ballast resistor connected in series to create a microplasma discharge ring inside the microhollow cavity (Figure 4.1c).

4.2.3 Instrumentation and MHCD Operation

Experiments were performed on an LCQ DECA XP^{+} ion trap mass spectrometer. The standard instrument ion source was modified with an extended ion transfer capillary (16 cm long, 0.381 mm I.D., and 0.1588 mm O.D.) held at 300˚C. The instrument was set to collect spectra in automatic gain mode for an ion trap injection time of 200 ms at 2 microscans per spectrum. The microplasma device was held in an aluminum supporting structure that housed gas and electrical connections to the microplasma chip. Power was provided by a Stanford Research Systems model PS350 power supply (Sunnyvale, CA). The microplasma device was operated at a constant negative voltage between -300 V and -350 V. Current was limited by a ballast resistor (2.187 MΩ,) and typically maintained at ~30 μA by adjusting the supply voltage. The microplasma device assembly was positioned ~1 cm from the mass spectrometer inlet capillary with the plasma stream oriented at a ~45˚ angle. Samples were placed directly in the ionization region ~1 to 5 mm away from the inlet (Figure 4.1a). The effluent plasma stream was allowed to flow past and interact directly with the sample. The effluent stream was incident at a 45° angle relative to the sample surface normal. This arrangement effectively desorbed, ionized,

and transported the analytes into the mass spectrometer. When testing liquid solutions, a sample drop was placed on the end of a borosilicate glass capillary tube which was held in the ionization region approximately 2 mm away from the microplasma source gas outlet.

4.3 Results and Discussion

4.3.1 Microplasma Characteristics

The predominant discharge type in this work is believed to be a low-current atmospheric pressure glow-type microdischarge, which occurs in the helium gas stream as it passes through the orifice and out to the sample. These discharges are non-equilibrium, low-temperature plasmas which generate such chemically active species as metastable atoms, high-energy electrons, and radical ions [48]. These are similar to the species obtained in packed-bed dielectric barrier discharge systems [49]. A typical background spectrum of the microplasma operated with helium is shown (Figure 4.2). With the discharge potential operated at –320 V and the helium flow rate at 0.28 L min^{-1}, the major ionic species identified were protonated water clusters ($(H_2O)_nH^+$, n = 2-4) with n = 2 dominating the spectrum. The reactant background ion mass spectrum obtained with this microdischarge was essentially equivalent to what has been reported for corona-to-glow atmospheric pressure discharges such as DART [20]. Background reactant ion spectra obtained with a commercial DART ion source and a homemade DART-type analog [50] were very similar to those obtained with the microplasma source presented here (data not shown). Similar water cluster distributions have been modeled by a process beginning with a Boltzmann-like distribution with n = 4-10, followed by

rapid declustering reactions in the atmospheric pressure ionization (API) interface resulting in the formation of the *n* = 2-3 clusters [51]. Ionization of neutral desorbates/analytes occurs by water-mediated proton transfer, making the device intrinsically ambient [38, 52]. Proton affinities of $(H_2O)_nH^+$ measured via guided ion beam experiments [53] have been shown to increase with *n* [53]. Under vacuum conditions, clusters with *n* = 2-3 present larger reaction cross sections for proton transfer relative to higher mass water cluster ions [53-54]. The abundance of cluster ions with *n* = 2-3 should therefore be advantageous for efficient proton transfer to analyte/desorbate molecules.

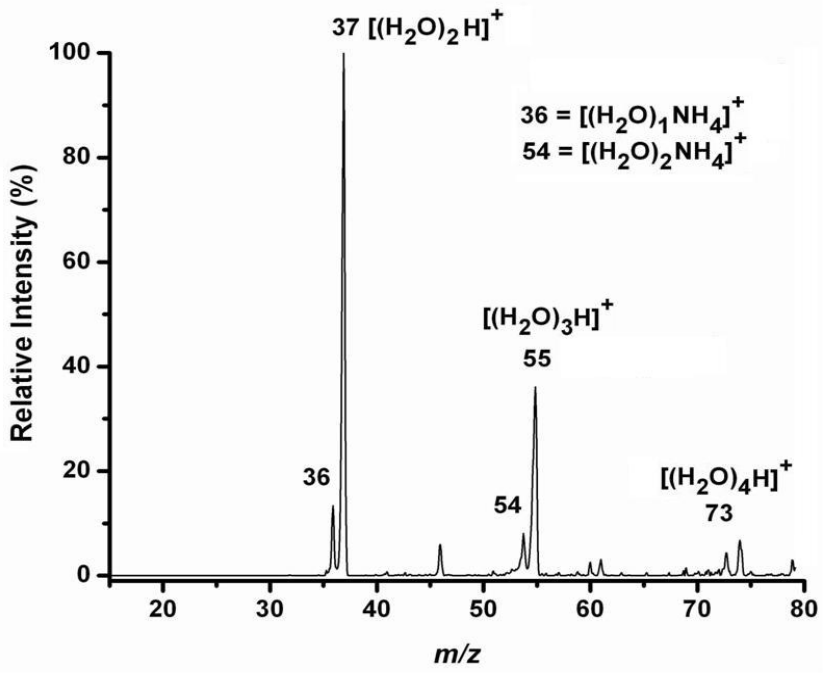

Figure 4.2 A typical mass spectrum of the reactant background ions generated by the microplasma ionization source using helium as the discharge gas. The spectral range scanned was *m/z* = 15 to 200, though no higher mass water clusters were observed.

The background spectra in our experiments show a distinct lack of H_3O^+. H_3O^+ has the lowest proton affinity of all the protonated water ions, as a single water molecule

is not able to "solvate" the proton efficiently. Thus, H_3O^+ is a very effective proton source and its absence further indicates that small water clusters are important in the eventual protonation of desorbates/analytes [55]. Based on these results, we believe that it is mainly the small water cluster ions that are most effective since the larger ions can be considered proton "sinks." Protonated water cluster ions under atmospheric pressure conditions have been previously presented as the primary ionization agents in ambient plasma ion sources such as DART [52], FAPA, and others. Proposed ionization pathways are believed to be similar to Kebarle's proton transfer mechanism reported to prevail in atmospheric pressure chemical ionization (APCI) [51].

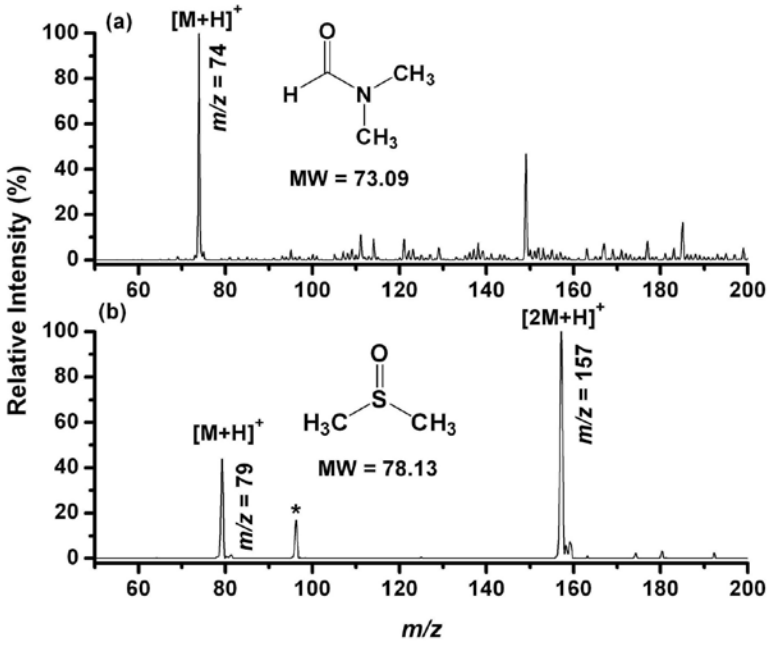

Figure 4.3 Mass spectra of (a) dimethylformamide (DMF), and (b) dimethyl sulfoxide (DMSO) vapor in air, acquired in positive ion mode using a helium microplasma. Ammonium adducts are marked by asterisks.

In addition to protonated water clusters, a second series of peaks corresponding to ammonium adducts was also observed in the microplasma reactant ion spectra (Figure 4.2). These species are believed to originate from trace amounts of ammonia in the laboratory environment and could lead to the formation of ammoniated analyte ions. The presence of these ammonia adducts was confirmed with a DART ionization source. Besides proton transfer, three other plasma processes can lead to charged products when these microplasma ion sources are used [56]. One process is electron-impact ionization of gas-phase targets. A second process is photoionization due to vacuum ultraviolet (VUV) light produced in the plasma, and a third is metastable-induced Penning ionization via collisions of electronically excited rare gas atoms with neutral analyte molecules. Although it is possible that these parallel ionization mechanisms are taking place simultaneously to a certain extent, the preponderance of protonated species in our spectra indicates prevalence of the proton transfer (PT) mechanism.

4.3.2 Performance of the Microplasma Source

Figures 4.3–4.6 illustrate the performance of the microplasma device for ionizing gaseous-, liquid-, and solid-phase samples in ambient air. To demonstrate that the microplasma source can be used to ionize trace gas-phase molecules, vials containing dimethylformamide [$(CH_3)_2NC(O)H$] (DMF), and dimethyl sulfoxide [$(CH_3)_2SO$] (DMSO) were each held ~2 m away from the microplasma device. In both experiments the samples were exposed to ambient air by removing the caps of the containing vials for several seconds, while the microplasma device and mass spectrometer were kept in the operating mode. After a few seconds delay, mass spectra were recorded with signal-to-noise ratios in excess of 1000. The major product observed for DMF was the protonated

monomer (Figure 4.3a), whereas for DMSO, both the protonated monomer and the dimer were observed (Figure 4.3b). In addition to the protonated species, the DMSO experiment showed the formation of ammonia adducts. The ammoniated water clusters described above are likely responsible for the appearance of these ionic species. The spectral response was extremely high for these compounds, and a stable signal was observed over the entire analysis time. Besides protonated analyte ions, prominent background peaks at *m/z* = 163, 180 and 279 were observed in many of the microplasma mass spectra. These species probably originated from atmospheric contaminants and/or from the microplasma cavity construction materials. No fragmentation was observed for DMF or DMSO. Collisions with metastable helium atoms carrying 19.8 eV, corresponding to the helium $^3S_1$ state, could transfer sufficient electronic energy to dissociate small organic molecules. However, the immediate reaction of metastable helium with atmospheric water or nitrogen makes direct ion activation by Penning ionization less probable [52].

To demonstrate the device's ability to ionize liquid samples, solutions of methyl salicylate and caffeine were tested. Figure 4.4a shows the mass spectrum of 10 µL of a 1 ppm methyl salicylate ($C_8H_8O_3$) solution prepared in neat methanol. The major species observed in the spectrum was the protonated analyte (*m/z* = 153). In addition, a less prominent fragment ion, corresponding to the loss of CH_3OH at *m/z* = 121 was observed. Methyl salicylate is a common chemical warfare agent simulant used as a surrogate of distilled sulfur mustard. Detection of ppm levels of this compound using the microplasma device is encouraging, as it could lead to its use in battlefield chemical warfare agent monitors.

The spectrum obtained from 10 µL of a 5 mM caffeine solution in 50:50 MeOH:H_2O is illustrated in Figure 4.4b. The major species observed in the spectrum were the protonated monomer and dimer ions. We found our ion source to also be effective on a variety of solid low molecular weight analytes, even though the helium gas was unheated. Experiments were conducted on powdered samples of amino acids deposited on the tip of glass capillary tubes essentially in the same arrangement as used for liquid samples. Figure 4.4c and Figure 4.4d show mass spectra of powdered L-leucine and L-histidine, respectively. Again, prominent protonated monomer and dimer ions were observed, together with evidence of some degree of formic acid neutral loss fragmentation in both cases.

The microplasma-mediated desorption/ionization source can be further used to detect drug molecules present on various surfaces, including pharmaceuticals and drugs of abuse. Figure 4.5 illustrates the surface analysis of three different over-the-counter pharmaceuticals and a one dollar US currency note, the likes of which are often found to contain trace amounts of illegal drugs. Figure 4.5a shows the surface analysis of Claritin® (10 mg), an antihistamine medicine used to treat common allergies. The active ingredient loratadine was detected as a distinct protonated molecule during analysis (m/z = 383). The non-steroidal anti-inflammatory drug (NSAID) ibuprofen was readily detected as the protonated molecular ion (m/z = 207) in an ibuprofen tablet (Figure 4.5b). In addition, a peak at m/z = 224, corresponding to the ammonium adduct, was observed. The peak at m/z = 177 was assigned to the loss of formaldehyde from the protonated molecule. Figure 4.5c shows the spectrum of a regular strength (250 mg) Tylenol® tablet. The base peak in the spectrum corresponded to the protonated acetaminophen monomer (m/z = 152), the

active ingredient in Tylenol®. The acetaminophen dimer ion was observed, but to a lesser extent. Similar to ibuprofen, additional peaks originating from ammonia adducts were observed.

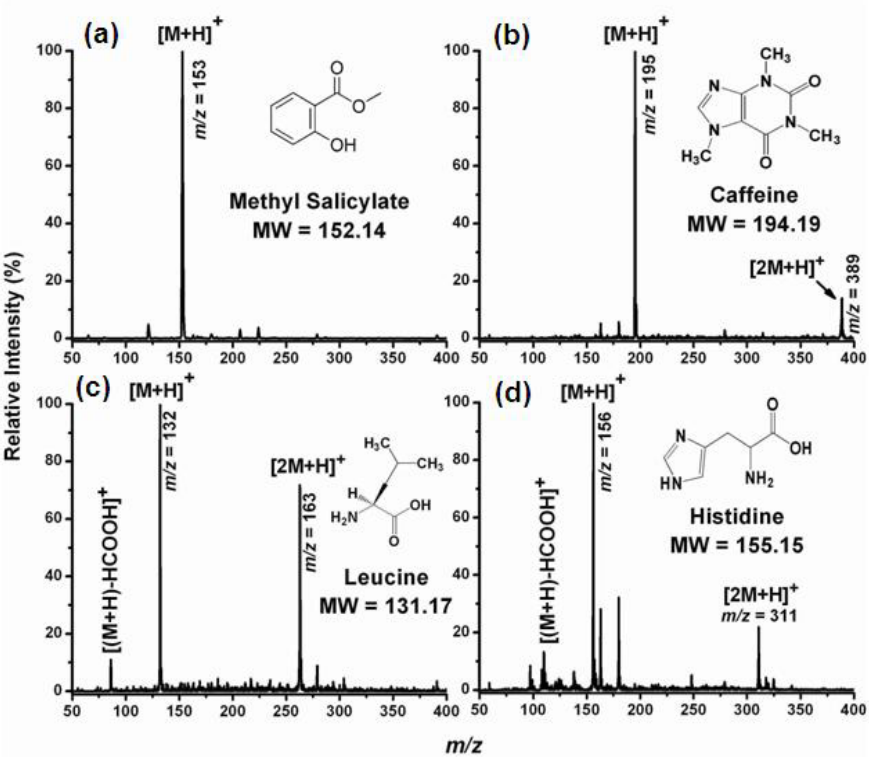

Figure 4.4 Microplasma desorption/ionization of liquid samples, (a) 1 ppm methyl salycilate in neat methanol, (b) 5 mM caffeine in 50:50 MeOH: H_2O solution, and solid samples, (c) L-histidine, (d) L-leucine. The mass spectra were collected directly from solutions (10 µL) or powdered solids deposited on the tip of glass capillaries.

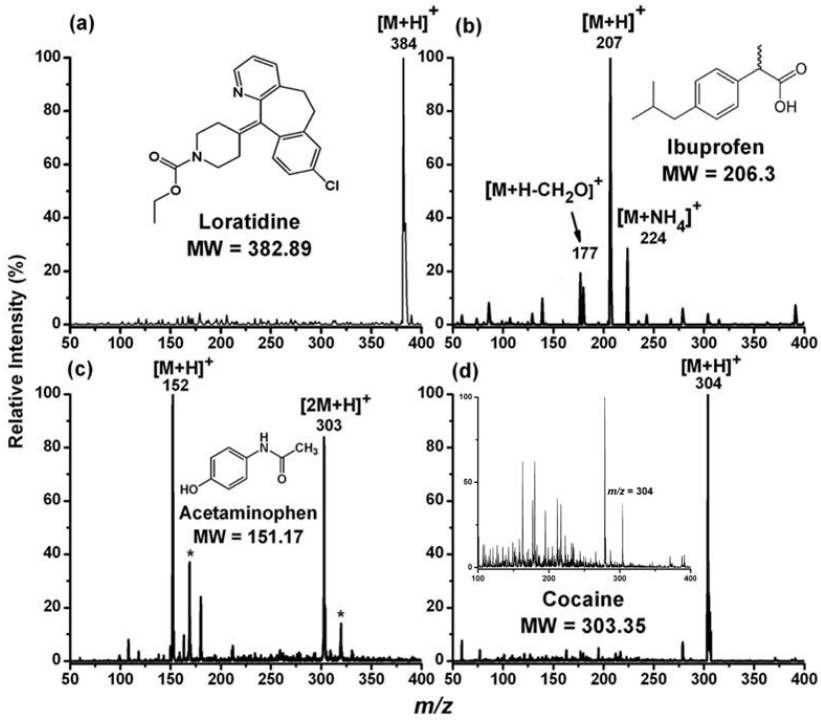

Figure 4.5 Analysis of various over-the-counter pharmaceuticals in tablet form, and a United States one-dollar bill using microplasma ionization: (a) a Claritin® tablet containing 10 mg of loratadine, (b) a generic ibuprofen tablet (200 mg), (c) a Tylenol® tablet containing 250 mg of acetaminophen, and (d) background-subtracted spectrum of a circulating one-dollar bill showing the presence of the drug of abuse cocaine. Inset in (d) shows the non-background-subtracted spectrum. All samples were directly analyzed without prior sample preparation.

For further demonstration of the effectiveness of this ion source for samples of increasing complexity, a U.S. dollar bill was investigated for the presence of illegal drugs on its surface. The bill was introduced directly into the ionization region. It is well known that low denomination paper currency in circulation can carry trace amounts of cocaine [57], which is a rather robust molecule. Figure 4.5d shows the background-subtracted mass spectrum obtained by direct analysis of this sample with the microplasma desorption/ionization source. Although the non-background subtracted spectrum (Figure 4.5d, inset) was significantly more complex, showing signals caused by the ionization of chemicals present in the ambient air and plasma species, the presence of cocaine,

detected as an ion at *m/z* = 304, is still clearly visible. These results suggest the potential of the microplasma device for use in law enforcement applications.

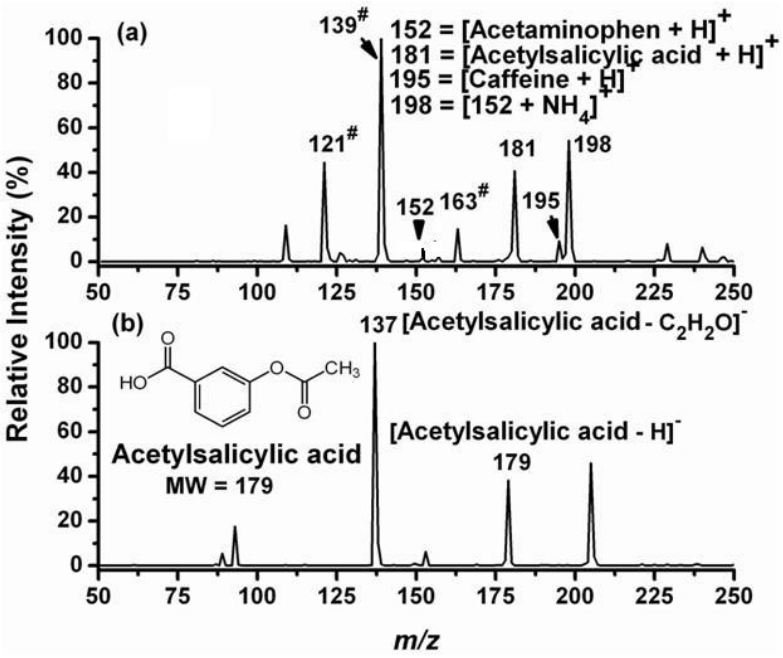

Figure 4.6 A multi-component Excedrin® pharmaceutical tablet interrogated with the microplasma device in: (a) positive ion mode, and (b) negative ion mode. The peaks annotated with "#" are fragment ions from acetylsalicylic acid.

Finally the analysis of a complex multi-component sample was demonstrated by probing a common migraine relief medicine, Excedrin®, containing acetylsalicylic acid (250 mg), acetaminophen (250 mg), and caffeine (45 mg) in both positive and negative ion modes (Figure 4.6). In positive ion mode, all three active ingredients were detected, as seen in Figure 4.6a. The protonated molecule signals are expected at *m/z* = 152, 181, and 195, respectively [58]. The presence of $[(H_2O)_nNH_4]^+$ in the background readily allows the formation of complementary NH_4^+ acetylsalicylic acid adducts. In addition, several acetylsalicylic acid fragment ions were observed. The peak at *m/z* = 121 corresponds to the acetic acid loss from the protonated molecule. Peaks at *m/z* = 139 and

m/z = 163 are fragments from losses of CH_2CO and water, respectively. The negative ion mode microplasma mass spectrum of the same tablet revealed the formation of the deprotonated acetylsalicylic acid molecule ion, concomitantly with a fragment ion due to loss of CH_2CO (Figure 4.6b). No other active ingredients were detected in negative ion mode. Formation of negative ions in plasma-based ambient ionization sources can originate from electron capture (EC), dissociative EC (often referred to as dissociative electron attachment), proton abstraction, or halide attachment [59-60]. In this case, the ionization mechanism appeared to follow a proton abstraction process. Although the mechanistic aspects of this microplasma ionization source have yet to be studied in detail, a potential pathway leading to formation of $[M–H]^-$ ions is proton transfer between the analyte and O_2^- species [59].

Table 4.1 Calculated detection limits based on measured sensitivity, analyte density, and approximate sample analysis volume. See text for details.

Drug	API*	Ion mode	LOD** (per mm^2)
Excedrin®	**Caffeine**	+	**5.4 ng**
	Acetaminophen	+	**14.3 ng**
	Acetylsalicylic acid	+	**3.0 ng**
		-	**0.5 ng**
Tylenol®	**Acetaminophen**	+	**0.4 ng**
Ibuprofen (generic)	**Ibuprofen**	+	**8.0 ng**
Claritin®	**Loratadine**	+	**0.4 ng**

*API refers to the active pharmaceutical ingredient
** LOD refers to the limit of detection expressed as the surface concentrations of various APIs per 1 mm^2 of table surface with estimated 1 μm plasma depletion layer.

Table 4.1 summarizes the calculated limits of detection (LOD) for various active pharmaceutical ingredients (APIs) in tablet formulations probed by the microplasma device in its current configuration. Specifically, an active sample analysis region was approximated based on a conservative estimate for plasma spot-size (3 mm disc) and a ~1 μm desorption/ionization depth. Analyte densities in the tablets were then calculated from the approximate tablet volumes and the indicated drug doses. Combining the calculated analyte densities, analysis volume, and measured detection limit yielded the minimum LOD values. Interestingly, the same analyte (acetaminophen) showed two different detection limits for two different tablet formulations, Tylenol® vs. Excedrin®. Such behavior can be attributed to differences in desorption rates of the analytes from the tablet excipient matrix and/or competing proton transfer reactions in the gas phase following desorption. It should be noted that these observed detection limits represent the calculated values for our current arrangement of the apparatus, and do not reflect any inherent limitations of the technology. Detection limits could be further improved by refining the control of the microplasma source and improving ion transmission into the mass spectrometer inlet.

Though reasonably good results were obtained with solid and liquid samples, vapor phase analysis was clearly the easiest to perform with this device. In general, most successful experiments were for species that had a nominal mass of <500 Da. Although the specific mechanism for desorption in these experiments is not yet well understood, one possibility is electronic energy transfer due to metastable helium and ion impacts. In this case, desorption would be non-thermal. Though thermal desorption cannot be ruled out, one must keep in mind that a primary characteristic of microplasmas is that energy is

deposited in the electron mean energy. Under these conditions, heating of the discharge gas is minimized, and so the thermal desorption induced by the microplasma ionization source itself is limited.

The microplasma devices, on average, operated without significant degradation for a few hours. Device failure was indicated by a rapid shift to more negative values of the potential required to sustain the discharge. Sputtering of electrode materials in and around the chip contributed to the device failure. It was observed that periodically cleaning the microdischarge orifice with high purity methanol effectively extended the device lifetime [45, 61-62]. The electrode sputtering phenomenon presents an engineering obstacle that limits practical use of these devices with relevant cavity dimensions below several tens of micrometers.

4.4 Conclusions

An ambient ionization source based on a microhollow cathode discharge has been developed for desorption/ionization of gaseous, liquid and solid samples, followed by mass spectrometric analysis. This type of microplasma was shown to be an effective desorption/ionization source for many low molecular weight compounds. Our results suggest that small water clusters play an important role in this plasma-based ionization source. This result solicits further investigation into the role that water content in the ambient atmosphere may have on ionization efficiency, and overall effectiveness of the device. Microplasma ambient ionization holds several advantages over alternative desorption/ionization approaches including ease of use and low cost, and may be desirable in applications where more demanding power, gas, or solvent supply requirements cannot be met. Our current work involves using similar devices for

spatially-resolved mass spectrometry, with the goal of employing their small size to improve image resolution. If successful, this would provide the basis for a solvent- and matrix-free, inexpensive ambient mass spectrometry imaging platform.

4.5 Acknowledgements

This work was supported by the Bio-Imaging Mass Spectrometry (BIMS) Center at the Georgia Institute of Technology and partially by an NSF CAREER grant 0645094. The authors would also like to thank Lan Sun for providing help in the preparation of microplasma chips.

CHAPTER 5
DEMONSTRATION AND CHARACTERIZATION OF A MHCD-BASED VUV PHOTON SOURCE FOR ATMOSPHERIC PRESSURE MASS SPECTROMETRY

In this section, we demonstrate the first use of an atmospheric pressure microplasma-based vacuum ultraviolet (VUV) photoionization source in atmospheric pressure mass spectrometry applications. The device is a robust, easy-to-operate microhollow cathode discharge (MHCD) that enables generation of VUV photons from Ne and Ne/H_2 gas mixtures. Photons were detected by excitation of a microchannel plate detector and by analysis of diagnostic sample ions using a mass spectrometer. Reactive ions, charged particles and metastables produced in the discharge were blocked from entering the ionization region by means of a lithium fluoride window, and photoionization was performed in a nitrogen-purged environment. By reducing the output pressure of the MHCD, we observed heightened production of higher-energy photons, making the photoionization source more effective for analysis of high-ionization-energy samples. The initial performance of the MHCD VUV source has been evaluated by ionizing model analytes such as acetone, azulene, benzene, dimethylaniline, and glycine, which were introduced in solid or liquid phase. These molecules represent species with both high and low proton affinities, and ionization energies ranging from 7.12 to 9.7 eV.

5.1 Overview

Plasma ion sources have been used extensively for elemental analysis and have also been applied to the analysis of molecular identities, primarily via coupling to mass

spectrometers. Horning *et al.* [63-64] were the first to describe an atmospheric pressure chemical ionization source using a corona discharge for small molecule analysis, with later work by Lubman *et al.* [65-66] which sought to increase the population of reagent ions by using an atmospheric-pressure glow discharge. These techniques laid the groundwork for plasma-based atmospheric pressure ionization mass spectrometry (MS), but they were mainly designed for coupling MS to chemical separations, where ionization suppression is mitigated by the simplified nature of the eluting stream. With the advent of ambient ionization direct analysis approaches, many different configurations of plasma ion sources have enjoyed renewed attention. These sources represent one of the fastest-growing and most diverse segments of the ambient MS field, as reflected in the numerous publications appearing in the last few years [67].

Ambient ionization sources based on plasmas involve direct current (DC) or radiofrequency (RF) electrical potentials applied to a flowing discharge gas such as nitrogen or helium. These discharges generate streams of ionized molecules, radicals, excited-state neutrals and electrons, and photons. Sources can be divided into two categories: distal and direct plasmas. In the former configuration, plasmas generate active species in a region separate from the sample region, and in the latter the plasma comes into contact with the sample. Direct analysis in real time (DART), is an example of a distal source, where most of the ionic plasma species are filtered from the gas stream, which is then heated and directed towards the sample [38]. Direct plasma techniques, such as the low temperature plasma probe (LTP) [42] and flowing atmospheric pressure afterglow (FAPA) [39] employ all reactive species in the plasma to induce ionization. Direct sources such as LTP may not require auxiliary heating of the gas stream to be

effective for low molecular weight analytes or in the case of FAPA, the electric discharge itself may produce enough heat to effect desorption. Microhollow cathode discharges, (MHCDs) such as the type presented in this paper, have been used as both direct ionization and distal desorption/ionization sources for MS [68-69]. Plasma-based ambient sampling/ionization techniques share the operational benefits of simple instrumentation and minimum need for high-purity solvents, though their greatest value to the field of ambient MS may be the fact that the mass spectra produced by these experiments is typically simple to interpret, due to a relative lack of multiply-charged species and multiple adduct ions.

Miniaturization of ion sources is a key development in MS that promises to open new possibilities for sampling and analysis [3, 31, 70-71]. To this end, microplasma sources are rapidly gaining popularity for their ability to deliver the ionization capabilities of larger plasma sources in a compact package, while simultaneously reducing the power and gas supply requirements to field-compatible levels [72]. This feature has led to their coupling to analyzers typically used for field work, such as ion mobility spectrometry (IMS) [73]. Microplasmas have also been used as excitation sources for elemental emission spectroscopy [74-76], and the development of alternative geometries [77] and arrayed devices [78] suited to various analysis or bulk processing tasks has been a focus of the previous work. The use of these sources in ambient sampling/ionization approaches, however, is still in its early stages.

MHCDs are a type of device typically constructed of two conductive layers separated by an insulator with a hole, or array of holes, through all layers. These devices are of particular interest for several reasons. First, they are easily implemented with DC

power and a low flow rate gas supply, making them simple and inexpensive to operate. This type of device is well-known to exhibit excellent discharge stability, which is beneficial in analytical applications. Better fundamental understanding of MHCDs has been the subject of recent studies [79].

Single photon ionization (SPI) is a powerful tool for mass spectrometry [80]. By bombarding analytes with photons possessing energy greater than their ionization energy (IE) threshold, they may be ionized in an efficient and chemically-simple manner. In the case of many organic molecules of interest, this ionization threshold is around 8 eV, corresponding to photons with wavelengths <155 nm. 8 eV photons lie squarely in the vacuum ultraviolet (VUV) spectrum, which begins around 200 nm (~6.2 eV), at the point which air no longer permits transmission. This makes SPI non-trivial outside of a vacuum environment, so additional precautions must be taken to deliver VUV photons to the sample efficiently. Surrounding the sample environment with a VUV-transparent gas, as we do in this paper, is one such approach that bridges the gap between “ambient” and “atmospheric pressure” ionization. This purge can be performed in an open experimental configurations and the technique is compatible with samples that have had little to no preparation.

A major benefit of SPI is the fine control of the ionization process: the amount of energy delivered to analyte molecules is limited by the photon energy, and causes ionization without excessive fragmentation. Therefore, SPI sources typically produce mass spectra that are simpler to interpret (lacking multiple adducts). If the photon energy is adjustable in an SPI experiment, it additionally enables discrimination between high-IE and low-IE substances in complex mixtures. This technique has suffered from a practical

viewpoint, since production of high photon fluxes necessary for efficient SPI is often complex and expensive, especially if laser techniques are used. Gas-discharge lamps may be employed instead, but these sources present their own challenges. Sample-source distance should be minimized in atmospheric pressure SPI experiments, but the size of traditional lamp sources limits proximity. These lamp sources typically require several tens to hundreds of Watts of electrical power, whereas the source reported here requires at most 12 W, which is advantageous in portable applications. Even so, VUV lamps have been effectively used in an ambient ionization technique first developed by Vaikkinen *et al.* to produce direct ionization of solid samples at atmospheric pressure [81]. This technique, desorption atmospheric pressure photoionization (DAPPI), may produce ionized species from samples either by direct photoionization or by exciting a proton transfer reaction from solvent dopants used in sample introduction. Atmospheric pressure photoionization (APPI), a more established atmospheric pressure technique, also employs VUV lamps [82].

Though VUV discharge lamps and various laser techniques are currently used to perform SPI in a variety of settings [83], smaller, more portable, less expensive, and even disposable microplasma devices may prove to be effective SPI sources too, especially for field MS applications. One type of microplasma, the microhollow cathode discharge (MHCD), lends itself particularly to this role by producing high electron energies with simple DC operation. The higher electron energies initiate the excimer (excited dimer) reactions capable of producing VUV light [3, 19]. In this paper, we report on the developments in adapting a distal MHCD ionization device for use as an atmospheric

pressure/ambient VUV photoionization source, demonstrating that it is highly capable and perhaps more flexible than traditional SPI sources.

5.2 Experimental

5.2.1 Materials and Chemicals

All chemicals were used as received without further purification. All samples investigated, including benzene, azulene, dimethylaniline, and glycine were obtained from Sigma Aldrich (St. Louis, MO). Molybdenum foil (99.95% purity) 100 µm thick was obtained from Alfa Aesar (Ward Hill, MA). Monocrystalline mica foil with 100 µm thickness was obtained from McMaster-Carr (Elmhurst, IL). Two types of LiF window were employed. The first, mounted on a Conflat (CF) flange on the UHV chamber, measured 12.5 mm in diameter by 4 mm thick. The second, used as a filter in front of the microplasma, was 25 mm square and 1.5 mm thick, and was obtained from Del Mar Photonics (San Diego, CA). A fused quartz slide, also used as a microplasma filter, was obtained from Chemglass Inc. (Vineland, NJ) and measured 25 mm square and 1 mm thick. Where appropriate, Viton o-rings used in the experiment were lubricated with UHV-compatible grease, Apiezon N, obtained from M&I Materials Ltd. (Manchester, UK).

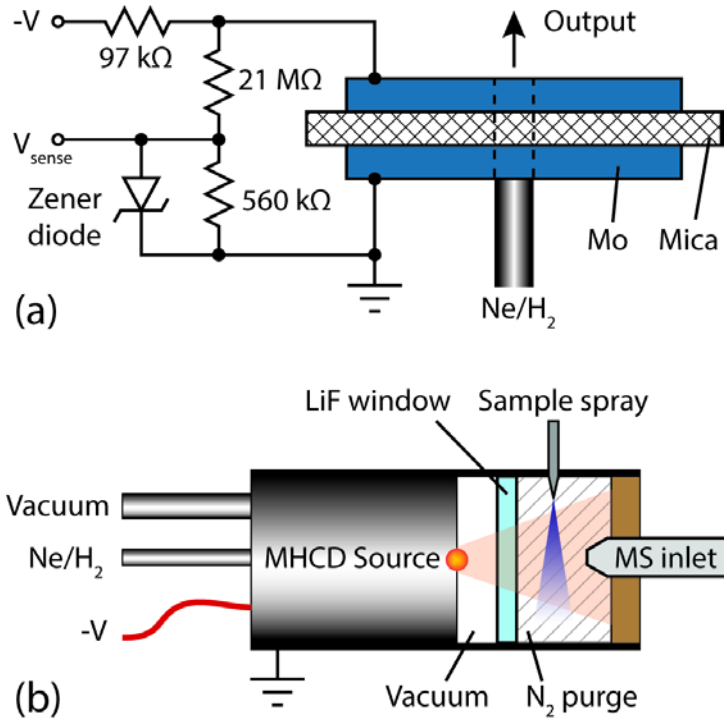

Figure 5.1 Experimental setup. (a) Electrical and gas connection diagram for the MHCD source, including ballast and discharge potential sensing circuits. (b) Mass analysis experimental setup shown with vacuum applied to the MHCD chamber, reducing pressure at the MHCD outlet. Light from the discharge travels through the LiF window and an N2 purge to reach the sample chamber, where the sample is introduced, photoionized, and then analyzed by the mass spectrometer. Liquid samples were sprayed into the chamber by a nebulizer (pictured) and solid samples were introduced on a glass capillary in the same position.

5.2.2 Microplasma Device

A MHCD device was utilized as the plasma source. Similar devices have been shown previously to produce substantial amounts of VUV light, though these sources have not been used in combination with MS to our knowledge [84]. As shown in Figure 5.1a, the device was constructed from two molybdenum foil electrodes, each 100 µm thick, separated by a mica foil with a thickness of 100 µm. The foils were first drilled mechanically, producing holes ~140 µm in diameter in each. After machining, the Mo foils were cleaned with acetone and isopropanol. The mica foil was cleaved with tape to

produce clean surfaces. Finally, the stack was clamped together with electrical and gas connections. Gas lines, and fittings used throughout the experiment were made of stainless steel or Teflon, and Viton o-rings were used to create gas seals at non-UHV interfaces. The use of these materials prevented the unwanted introduction of volatile compounds into the plasma. Discharge current was limited by a ballast resistor (97 kΩ). Discharge potential was measured with the aid of a high-impedance voltage divider (also shown in Figure 5.1a) and recorded using a National Instruments USB-6008 DAQ module after passing the signal through a buffer amplifier (not pictured).

5.2.3 Microplasma operation and instrumentation

Neon and hydrogen gas were supplied to the MHCD through two FMA-5500 series mass flow controllers (MFCs) from Omega Engineering (Stamford, CT). In order to precisely supply small concentrations of hydrogen to the MHCD, a premixed bottle with a moderate concentration (2-8% H_2) was first produced. This was accomplished by combining calibrated volumes with each gas at known pressure, measured by a model 890B Micro-Baratron pressure transducer from MKS Instruments (Andover, MA). The premixed gas was then metered through the first MFC, and pure Ne, metered by the second MFC, diluted the output to the desired concentration (0.1%–8 % H_2). A computer controlled the MFCs, and the relative flow rates were adjusted automatically in order to produce the desired hydrogen concentration and total flow rate as the experiments were conducted. Power was provided by a Stanford Research Systems model PS350 power supply (Sunnyvale, CA). The MHCD was operated with a DC potential between -1000 V and -1200 V. Current into the ballast resistor and plasma device was held at approximately 10 mA by small automatic adjustments to the supply voltage. The addition

of hydrogen to the gas mixture tended to slightly increase the discharge current, so this was a necessary step during experiments probing the influence of H_2.

In the course of optimizing the ion source, two plasma operating environments were tested. Initially the MHCD output chamber was purged with N2 (Figure 5.1b) and observed a maximum in the VUV flux as a function of total gas flow rate around 15 sccm. In another configuration, a vacuum interface (Figure 5.1b) reduced pressure at the MHCD output, which moved the optimum light output to lower values of gas flow rate. However, plasma stability suffered and a flow rate of 20 sccm was found to be optimal for this arrangement. As discussed in more detail below, the reduced pressure conditions increased the output of higher-energy photons.

Sputtering of the MHCD cathode was observed after experiments, and the damage was investigated with an optical microscope. Over the course of a device's lifetime, sputtering would expand the cathode diameter up to twice its original size. As the cathode diameter grew larger, the MHCD would operate with reduced stability, at which point the device was replaced. Other effects dependent on device lifetime were not observed. Typically these devices would survive several hours of continuous operation, or approximately a week of intermittent operation. Longer lifetimes can be achieved using reduced duty cycles and operation using radiofrequency or pulsed power supplies [85]. The MHCD design and materials used were found to be preferable relative to several others investigated due to their robust nature. MHCDs with cathodes that were insufficiently thick, or that did not have clean circular holes, sometimes suffered from instability or reduced lifetimes.

5.2.4 Optical experiments

A multichannel plate (MCP) detector was used to distinguish VUV photons from the large amount of visible light produced by the discharge. MCP detectors are typically "solar-blind," making them useful for detecting ionizing radiation [86]. In this case, <200 nm light may produce photoelectrons on the surface of the MCP, which are then amplified and detected in our experiment. This setup served as a way to directly measure the photon energy without a vacuum monochromator. While they could not resolve particular wavelengths, the experiments were able to measure light output in particular energy ranges by careful selection of gas and window filters between the source and the detector.

The microplasma source was positioned in front of a LiF window on a vacuum chamber housing a MCP detector. The MCPs were a matched pair of 25 mm (effective diameter) plates purchased from Photonis USA, Inc, (Lancaster, PA). The voltage applied to each plate was 825 V. An aluminum housing was constructed around the microplasma and LiF window, excluding light from the laboratory and permitting control of the interface atmosphere. The MS interface was purged with air and nitrogen during these experiments, both at a rate of 2 L/min. A filter window, made from either LiF or fused quartz, was positioned between the microplasma source and the LiF detector window. LiF permits transmission of light wavelengths >105 nm, whereas quartz transmits light >160 nm [87]. The filter was positioned approximately 5 mm from the microplasma source and 5 mm from the detector window. A pinhole aperture was added in front of the detector window in order to reduce signal intensity.

MCP signal pulses were filtered through a DC decoupling circuit and amplified by an Advanced Research Instruments Corporation F-100T pulse preamplifier. A computer with a National Instruments USB-6008 data acquisition module measured pulse rate from the preamp.

The first set of experiments compared VUV transmission through different interface environments. This was achieved by first optimizing the source parameters by maximizing MCP signal, and then comparing the count rate as a function of different window materials and purging gases. These transmission configurations were examined while ramping the operating voltage of the MHCD device.

Experiments measuring VUV flux as a function of hydrogen concentration were performed in the optimal high-transmission configuration, at the same low-gain setting used previously.

5.2.5 Mass spectrometry experiments

Figure 5.1b shows a typical arrangement for MS experiments. The microplasma source was directed at the inlet capillary of an Agilent 6410 Triple Quadrupole mass spectrometer, operating in Q_1 single quadrupole scan mode. A housing constructed of aluminum and polyether ether ketone (PEEK) was built to control the experimental environment as in the light detection experiments. A window flange, containing the square LiF filter used previously, was constructed to isolate the environment around the microplasma from that around the mass spectrometer inlet. This prevented any transmission of ions, electrons, and metastables generated in the microplasma from entering the inlet chamber where the sample was placed.

Samples for these experiments were positioned directly in front of the mass spectrometer inlet, after the LiF filter in the direction of photon and ion transmission. Two sample introduction techniques were employed. Liquid samples (*e.g.* benzene, acetone, dimethylaniline) were sprayed in by means of the nebulizer (pictured) that was part of the stock Agilent ESI source. Solid samples (*e.g.* azulene) were deposited onto a glass capillary, which was introduced into the sample chamber by means of an opening in the side. The nebulizer and the housing were held at ground potential. The applied voltage to the plasma was -1200 V and the current was 10 mA. Plasma gas flow was typically 15-20 sccm and the plasma region was purged with N_2 at a rate of 2 SLM, except as specified. Samples were purged with N_2 at a rate of 11 SLM. The same aluminum housing was employed to contain the sample and purge, but this was performed predominantly to facilitate purging and to collect fumes from carcinogenic samples. This ionization technique could also be performed with a more open configuration as is typical with standard ambient ionization sources, providing that a sufficient VUV-transparent purge gas flows between light source and sample.

5.3 Results and Discussion

5.3.1 Microplasma performance

Results from the light transmission experiments are shown in Figure 5.2. The signal intensity varied over several orders of magnitude, and so in the configurations permitting the highest transmission of VUV light, the detector gain needed to be reduced to avoid damage. Reducing the voltage applied to the MCPs and adding a foil pinhole aperture to reduce flux incident on the detector accomplished this. In order to compare

signals at both ends of this intensity range, high-gain data was first collected for all signals. In the highest-transmission configuration, LiF window with N_2 purge, the detector saturated before maximum MHCD voltage was achieved. The aperture was put in place and the MCP gain was reduced, and the experiment was repeated, yielding a lower intensity signal. The low-gain data were scaled to match the unsaturated portion of the high-gain data. Comparison was achieved by plotting the resultant higher-than-detectable signal on the same scale as the low-gain, high-transmission data.

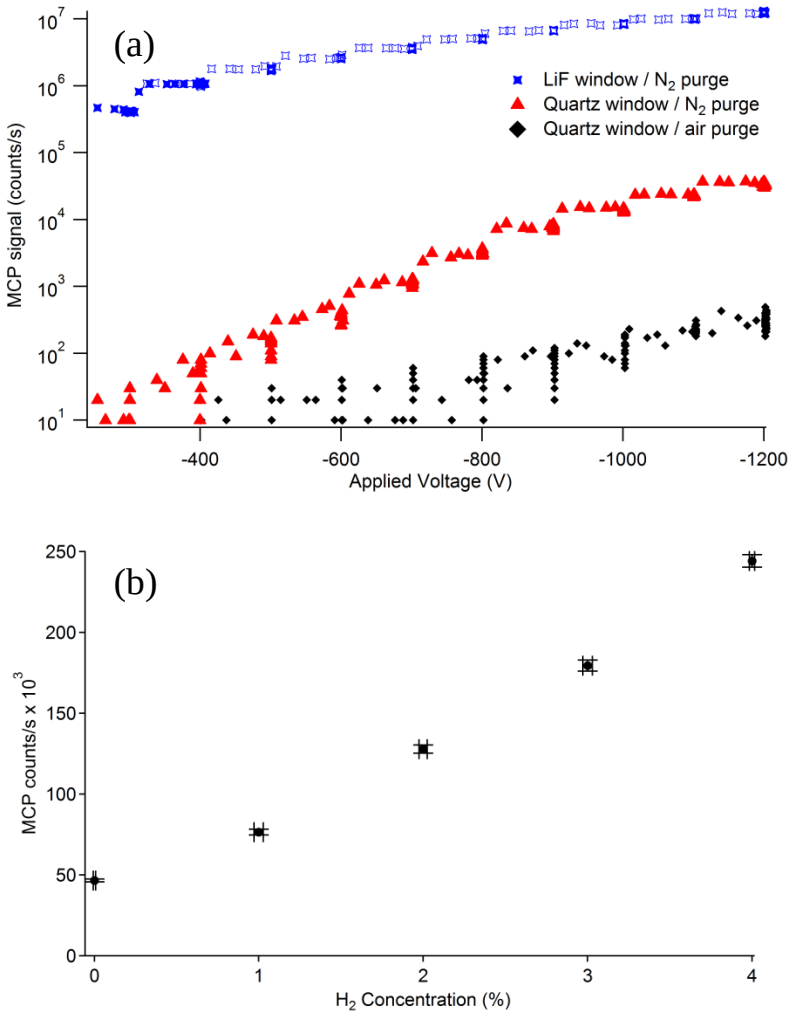

Figure 5.2 Microplasma light detection by an MCP detector. The MHCD was operated with 20 sccm Ne flow. (a) MCP response to MHCD source with various interfaces: LiF vs. quartz filter windows, and N_2 vs. air purge. Intense signal using LiF windows and N_2 purge has been scaled to fit. (b) MCP signal vs. H_2 concentration. Discharge was

operated again at 20 sccm with an applied voltage of -1200V. Note the gain has been reduced, and the first point in this plot corresponds to the maximum in plot (a).

As illustrated in Figure 5.2a, the MCP signal was greatly enhanced by purging the microplasma/MCP detector interface with N_2, because VUV light is strongly absorbed by both oxygen and water in air [88-89]. It has been shown that a nitrogen or rare gas purge, which would exclude these absorptive species, may permit transmission of VUV photons under atmospheric pressure conditions [90]. In the case of nitrogen, this was shown in the literature to be fairly effective for wavelengths as low as 105 nm [91]. Our results reaffirm the importance of a VUV-transparent purge gas in any ambient SPI application. Figure 5.2a exhibits a dramatic difference in signal when the quartz window was replaced with LiF; the additional signal is driven by light that will be transmitted by LiF but not by quartz, namely, photons in the range between the LiF cutoff at 105 nm and the quartz cutoff at 160 nm. This would include the Lyman-α emission line at 121.6 nm, though the reader should note that there was no H_2 addition required to observe this flux. Optical emission spectroscopy shows that there are strong emission lines from singly-charged Ne in this range, though more intense UV emission lines in the range of 160-200 nm are also present [92]. Figure 5.2(a) shows the MCP response increases with the use of a LiF window and the subsequent transmission of more energetic photons. This increase is about two orders of magnitude, though it is important to note that the MCPs are approximately two orders of magnitude more sensitive to these wavelengths [93]. This would imply that the total flux of photons between 105-160 nm is likely on par with the flux of 160-200 nm light. This result is somewhat surprising compared to the NIST emission spectrum; the shorter wavelengths are mainly produced by singly-charged Ne

species, which are typically much less abundant than neutrals in plasmas. This observed skew in intensity seems to be a confirmation of the theory that MHCDs produce a high-energy electron distribution and a high degree of ionization, a result attributed to the Pendel effect in this type of microplasma [15, 47]. Figure 5.2b shows that the VUV flux can also be enhanced considerably with the addition of only a small amount of H_2 into the discharge. We were limited to investigating H_2 concentrations up to 8% by our instrumentation (only part of this range is shown). The VUV flux increased in this range with H_2 concentration and there did not appear to be any significant discontinuities in this relationship. However, since VUV flux was not the limiting factor in our experiments, lower H_2 concentrations were mostly used to permit longer run times between gas mixing steps.

Previous results analyzing the light from Ne/H_2 MHCDs observed intense Lyman-α output, which was maximized with respect to H_2 at less than 1 % concentration in Ne [94]. Our data show no such maximum. Given the results of Becker *et al.* [84, 94], it seems reasonable to conclude that our detected signal stems from a broader range of emission than a simple Lyman-α source. We find support for this in the literature: in high pressure (1000 Torr) VUV lamps it has been observed that Lyman-α flux accounts for only 5% of the total output between 100-200 nm [95]. This may be the results of collisional quenching of the excited hydrogen state that gives rise to the Lyman-α photons. In any case, we observed the production of useful photon fluxes from H_2 in the 105-160 nm range to increase up to H_2 concentrations of at least several percent. The total flux at peak operating conditions was estimated based on the quantum efficiency of the MCPs at the wavelengths of interest. We estimate this source produces 4×10^{10}

VUV photons/s·sr. This is comparable to the flux from certain commercial Kr discharge lamps (~10^{11} photons/s) [96].

There appear to be several factors affecting the photon energies and fluxes produced by this source. As usual, discharge current and gas pressure appear to be critical. The MCP signal increases with discharge current and the addition of H_2 to the Ne discharge. The Ne discharge was shown to produce ionization of some molecular species (described below), and this effect was enhanced by H_2 addition in two ways: new peaks often appeared in mass spectra after H_2 was added to the discharge, and the overall signal level was enhanced. Finally, it was found that decreasing the pressure in the plasma output chamber enhanced photoionization of high-IE compounds. This is thought to be a result of reducing the collisional quenching mechanism which can limit Lyman-α production. Using these steps, this source can be effectively tuned in energy to produce these different ionization capabilities, as described in the following experiments.

5.3.2 Mass Spectrometry Applications

As an initial test of the performance of this ion source, the microplasma VUV source was used to photoionize a series of model compounds in MS experiments. The source was operated under the optimum parameters described above. Analytes were chosen to demonstrate the tunability of the photon energy range and the applicability to diverse molecules, some with low proton affinities. The latter are not as easily detected with typical ambient plasma-based techniques, unless very specific conditions are employed [52]. As before, the MHCD output chamber was purged with N_2. Azulene, a polycyclic aromatic hydrocarbon with an IE of 7.42 eV [97], was introduced into the sample chamber and analyzed by microplasma VUV photoionization MS (Figure 5.3a).

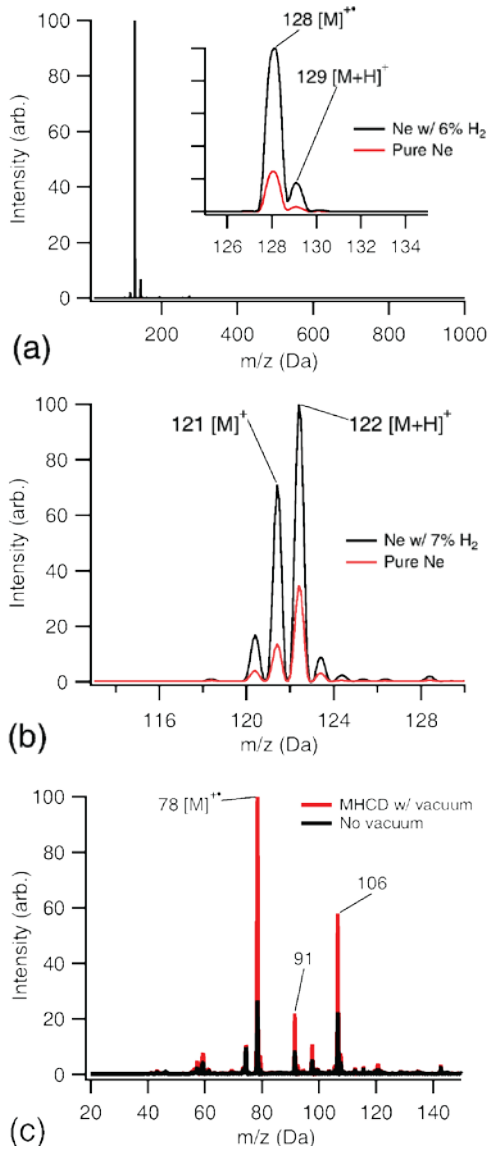

Figure 5.3 Sample mass spectra. (a) Azulene spectrum, shown with both Ne and Ne/H_2 discharge sources under N_2 purge. Inset: enlarged view of analyte peaks highlighting relative intensities. Total signal and molecular cation signal are increased with addition of H_2 to the plasma. (b) Dimethylaniline spectrum under similar conditions. Signal is likewise improved with the addition of H_2. (c) Benzene spectrum, obtained with pure Ne plasma operating with reduced pressure at the MHCD output.

With a pure Ne discharge, the molecular cation signal at 128 Da was observed, as well as a smaller satellite peak at 129 Da resulting from the combined isotopic abundance of ^{13}C $[M]^{+\bullet}$ and ^{12}C $[M+H]^+$ contributions. The figure shows that with a small (6 %)

admixture of H_2, the intensity of the $[M]^{+\bullet}$ peak was increased six-fold, in accordance with our photon detection experiments. The microplasma VUV source was also shown to be effective for photoionizing dimethylaniline, a liquid-phase cyclic organic with an IE of 7.12 eV [97]. Again, addition of H_2 to the discharge increased both the total signal level and the proportion of $[M]^{+\bullet}$ species detected in comparison to the protonated species. Signals for protonated analytes and more complex reaction products were observed for many other compounds, but the VUV source did not produce simple molecular cations for samples whose IEs ranged >7.5 eV. The source of the protons is undetermined, but may originate from residual atmospheric water in the chamber. Glycine (IE = 7.6 eV) was the lowest-IE analyte that was not observed as a molecular cation, which implied effective photon energy between 7.4-7.6 eV for the Ne/H_2 source purged with N_2.

It was suspected during early experiments that the contribution of Lyman-α (10.2 eV) photons was a major mechanism of this ionization enhancement, and we sought to improve production of these photons in our source. This was accomplished by adapting our experiment to more accurately emulate the work of Becker *et al.* [94] which demonstrated Lyman-α production by coupling microplasma devices to vacuum monochromators, thus reducing the pressure at the output of the plasma. We reproduced this condition at the MHCD outlet with a roughing pump, sealing the apparatus carefully to prevent the ingress of air. This minor modification resulted in raising the effective photon energy of our source. Under this conditions, we were able to detect $[M]^{+\bullet}$ species from acetone (IE = 9.70 eV). However, as acetone has a fairly high proton affinity (812 kJ/mol), the $[M+H]^+$ ion signal was still prominent. Benzene, which has an IE of 9.1 eV and a much lower proton affinity (184 kJ/mol), was analyzed as an indicator of source

photon energy. In this configuration, an abundant $[M]^{+\bullet}$ signal was observed (Figure 5.3b), together with signals we believe to represent ethylbenzene, xylene, (both with molecular weight 106 Da) and fragments of these compounds which often accompany benzene. Xylene and ethylbenzene are readily photoionized even in trace quantities, and generate fragments with molecular weight of 91 Da [98]. It may also be possible to form these compounds as a result of ion/molecule reactions in the benzene vapor cloud. The $[M]^{+\bullet}$ signal was present when the MHCD was operated with pure Ne, and as in previous experiments, signal intensity was significantly enhanced by the addition of only 4% H_2. Figure 5.3 also shows the result of closing the valve to the pump which reduced the MHCD pressure; this increased the pressure at the MHCD without introducing N_2 to the vicinity of the discharge, as is typical in atmospheric pressure operation. Some background peaks maintained a nearly constant signal, while the benzene peaks were significantly reduced. By reducing the pressure on the MHCD outlet and using a LiF window and a N_2 purge, high energy photons were generated that effectively ionize a range of samples with IEs as high as 9.7 eV.

5.4 Conclusions

This work demonstrates the first use of an atmospheric pressure microplasma-based vacuum ultraviolet (VUV) photoionization source in atmospheric pressure mass spectrometry applications. The device is a robust, easy-to-operate microhollow cathode discharge (MHCD) that enables generation of VUV photons from Ne and Ne/H_2 gas mixtures. The initial performance of the MHCD VUV source has been evaluated by photon detection with a microchannel plate detector and by analysis of diagnostic sample ions using a mass spectrometer. Specifically, analytes such as acetone, azulene, benzene,

and dimethylaniline were introduced in solid or liquid phase and easily detected with minimum fragmentation. These molecules represent species with both high and low proton affinities, and ionization energies ranging from 7.12 to 9.7 eV. This work highlights that by tuning the operating parameters, it is possible to operate the MHCD VUV source to perform in applications where selective ionization is required.

Microplasma sources are becoming popular in a wide range of applications for their low power and gas consumption, as well as for their compact and cost-effective nature. VUV photons similarly have already gained attention as a simple, effective, ionization means for mass spectrometry. As these MHCD VUV sources become better understood, it is conceivable that their impact in the plasma physics community will expand as they begin to be applied more widely in mass spectrometry.

5.5 Acknowledgements

The authors would like to acknowledge the NSF for support through an American Recovery and Reinvestment Act (ARRA) Major Research Instrumentation (MRI) Instrument Development grant #0923179 to FMF and TMO. The authors would also like to thank Dr. Prabha Dwivedi for invaluable discussions on this project.

CHAPTER 6
DAMAGE OF BIOMOLECULES BY MHCD IRRADIATION

6.1 Irradiation of bio-samples using MHCD

Using MHCDs, we have effectively produced ions at atmospheric pressure and analyzed them via mass spectrometry. Sources with sufficient energy to produce ionization will often be capable of modifying the chemical structure of biomolecules. For biological applications of this technology, understanding of such effects is important. Indeed, plasma medicine is a rapidly growing field [99], and microplasma devices are being applied to a wide range of living cell and tissue samples. Damage to DNA by these devices has been observed [100-101], but the mechanism of such damage is not yet well understood. The studies performed in this area indicate that such mechanisms are likely highly dependent on the sample environment and plasma source used.

We have chosen a range of biomolecular sample films, dried from solutions on gold surfaces, as a model for this study. By exposing the samples to a MHCD source with and without a filtering window, we studied the effects of MHCD-generated VUV irradiation as well as the damage contribution by the charged and neutral energetic species produced in the discharge.

6.2 Experimental

Samples of deoxyadenosine monophosphate (dAMP), deoxycytosine monophosphate (dCMP), deoxythymine monophosphate (dTMP), and ribo-adenosine monophosphate (rAMP) were prepared in solution and dried in spots onto a gold substrate.

Irradiation of the samples was performed in a purged environment of dry N_2 gas at atmospheric pressure. The first irradiation experiment employed a LiF window between the MHCD and the sample plate, as in the experiments performed in §3.3. This allowed only the light (down to wavelengths as short as 105 nm) produced by the MHCD to interact with the sample. The distance between the source and the sample plate was ~1.5 cm. The plate was oriented normal to the axis of the MHCD, which fully illuminated the sample. The MHCD structure was identical to that used in §3.3, and the discharge was operated using a 4% H_2 in Ne gas mixture at a rate of 20 sccm at atmospheric pressure with a 4 SLM N_2 purge. The discharge current used was ~10 mA. The sample chamber was purged with N_2 at a rate of 9 SLM. Exposure of the sample was performed for 1, 5, and 30 minute total intervals. Raman spectroscopy was used to analyze each sample between each exposure. Each sample was analyzed by Raman in five locations, and the data presented represents an average of those measurements.

Following VUV irradiation, a series of exposure using the discharge without the window was performed, allowing irradiation by electrons, ions, and metastable neutrals from the discharge. These exposures were performed for total spans of 1, 2.5, 5, and 30 minutes, again repeating Raman analysis between each exposure. For these experiments, a pure Ne discharge was used. The Ne gas was supplied to the MHCD at a rate of 20 sccm, and the sample/plasma environment was purged with N_2 as before at a rate of 9 SLM. Raman measurements were found to be reproducible at the same sample position, indicating that damage to the sample from the laser is negligible. The data reported have gone through a background subtraction process.

6.3 Results and discussion

VUV irradiation of these samples produced very little change in the Raman results. This is likely due to the low total VUV flux. In §5.3.1 we estimated the VUV (105-200 nm) flux from this source to be 4×10^{10} VUV photons/s·sr under the operating conditions used, of which ~10^9 photons/s would reach our sample substrate. Figures 6.1-6.4 show the results of the windowless plasma irradiation, where metastable Ne, electrons, and gas phase chemistry (despite the N_2 purge) play a larger role.

It is common practice in the literature for similar experiments to normalize Raman data by one of the peaks [102]. For our data, the most logical choice of normalization peak would be one that is present in all our samples. In this case, a peak related to the phosphate backbone would be ideal, as the nucleoside varies between these samples. One such peak occurs at 847.5 cm^{-1}, which corresponds to an O-P-O stretch mode in the phosphate (Table 6.1) [103]. Unfortunately, the intensity of this peak is low in our data, and overlapped too much with neighboring peaks to be used. This makes normalization more difficult, and impedes comparison between these samples.

We performed normalization to a nucleoside peak in order to observe relative changes in peak intensity for different bands within a sample, but a consistent trend was not observed. Some peaks did change, but this did not generally occur consistently as a function of irradiation time. One exception might be the 30 minute irradiation time scan: most peaks decreased after this much exposure. The spectra presented in Figures 6.1-6.4 shows the non-normalized, data after background subtraction. Peak assignments are presented in Tables 6.1-6.3 [103-104].

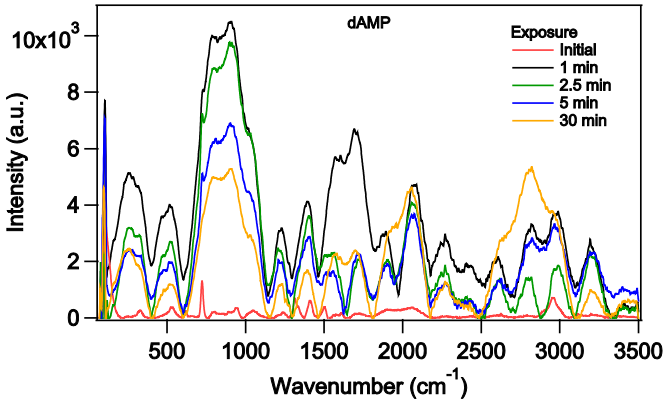

Figure 6.1 Raman spectra of dAMP before and after windowless MHCD irradiation

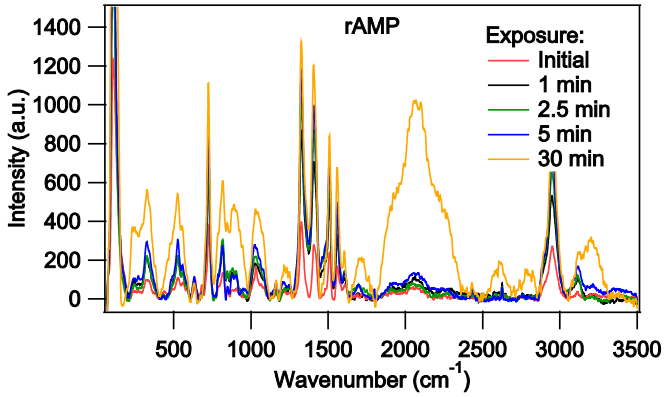

Figure 6.2 Raman spectra of rAMP before and after windowless MHCD irradiation

Peak assignments matched well for the initial Raman spectra of dAMP and rAMP, which is consistent with the small variation in these molecules. For rAMP, we see the reduction of several peaks, which corresponds to damage of the nucleoside as this sample is irradiated, as shown in Table 6.1.

Table 6.1 Peak assignments for Raman spectroscopy of adenosine monophosphate. Trends observed for rAMP and dAMP after windowless microplasma irradiation are indicated by arrows.

Raman shift cm^{-1}	Assignments	rAMP trend
722.527	Ring breathing (Pyrimidine)	↓
792.371	Backbone(OPO stretching), Ring stretching	
847.5	Backbone(OPO stretching)	
946.052	NH_2 rocking, sugar (ribose)	
1047.35	N-sugar stretching, sugar (CO stretching)	↓
1072	N-sugar stretching, backbone (PO_2^-) stretching	
1242.654	Ring stretching (C5-C6)	
1312.67	C-N stretching imidazole	↓
1410.451	C6-N1 stretching Pyrinidine, ring	↓
1500.574	Ring stretching	↓
1551.5	Ring stretching (Pyrimidine)	↓
1611.652	Ring stretching (Pyrimidine)	
1685.103	NH_2 scissoring	
2955.704	OH/NH stretch	

The rAMP molecule has one additional oxygen compared to dAMP, located on C2. The extra O in the ribose backbone prevents the formation of the double helix conformation which provides stability in DNA. While DNA is typically more robust as a result of this effect in vivo, in these samples the molecules exist in single strands, where we may not expect to observe this effect. However, the presence of the O in rAMP may enhance damage independently of this effect. It is believed that RNA damage may be enhanced by a radical-mediated mechanism via the oxygen atom [105].

In the dAMP sample, after only one minute irradiation we observe a highly modified Raman spectrum, with peaks disappearing, decreasing, and broadening at various wavenumbers. In contrast with the radical-mediated damage pathway described above, our results do not indicate enhanced damage of rAMP vs. dAMP.

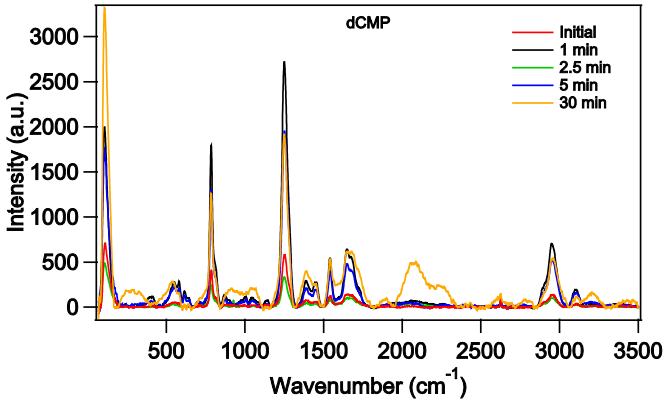

Figure 6.3 Raman spectra of dCMP before and after windowless MHCD irradiation

Table 6.2 Peak assignments for Raman spectroscopy of cytosine monophosphate

619.401	Ring breathing (Pyrimidine)
786.206	Ring breathing (Pyrimidine), backbone (OPO stretching)
873.906	N-C-N stretching
1007.504	NH_2 rocking
1047.122	N-Sugar stretching, sugar (CO stretch)
1139.417	C5-C6 stretching
1251.907	Ring-CH_3 stretching
1390.552	(C6-N1) stretching (Pyrimidine), ring
1451.041	C=N stretching (Pyrimidine) and C_2H_2 deformation
1542.261	NH_2 deformation, ring stretching

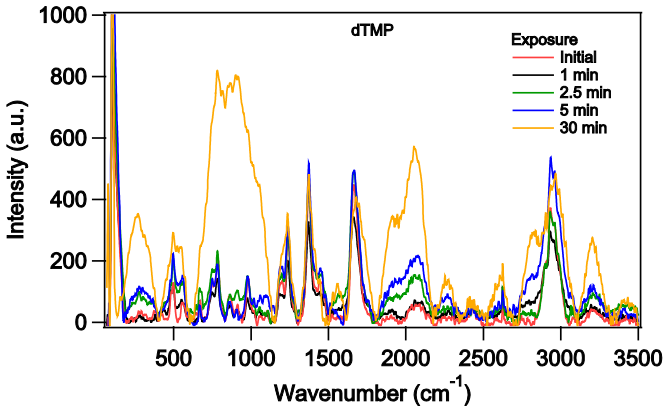

Figure 6.4 Raman spectra of dTMP before and after windowless MHCD irradiation

Table 6.3 Peak assignments for Raman spectroscopy of thymine monophosphate

668.492	Ring breathing Imidazole
783.345	Ring breathing (Pyrimidine)
854.062	N-C-N stretching
979.614	N-Sugar stretching
1102.294	N-Sugar stretching, PO_2^- stretching
1237.548	Ring-CH_3 stretching
1370.253	C-N stretching (Pyrimidine)
1390	CH_3 deformation
1558.665	Ring stretching (Pyrimidine)
1665.579	C=O stretching

The damage profile for dCMP and dTMP were similar to that observed in dAMP, though it should be noted that we cannot distinguish absolute peak increases from relative increases in this analysis without the normalization steps noted previously. In general, peaks were degraded after a long exposure, but the nature of this damage could not be clearly identified via this method. This is an ongoing work, and this analysis is not complete. However, the damage processes that may be involved in these experiments are described in further detail in the literature.

In the preceding discussion, we have assumed our normalization methods have not obscured other phenomena that may affect signal strength. It should be noted that there is another effect that could be responsible for the apparent increase in signal shown in the raw data in Figures 6.1-6.4. The windowless MHCD cathode is constantly sputtered into the gas phase, and some of the Mo particles could make their way to the sample surface. A common Raman spectroscopy technique, surface-enhanced Raman spectroscopy (SERS), utilizes metallic nanoparticles to significantly enhance Raman signal from sample molecules [106]. While Mo is not traditionally recognized as a SERS-

active material, it is possible there could be a related effect increasing the observed peaks. If this effect is active, our signal enhancement is likely due to removal of the sample, as the measured sample spot is well into the interior of the bulk. We would probably not observe the SERS-active interface between the sample and gold substrate until the sample thickness was reduced below the 2 μm effective depth.

6.4 Conclusions

The results from these experiments do not provide a sufficiently clear picture of the complex damage processes that are likely occurring in the sample [107]. As in [69], we expect metastable Ne and the reactive products of the resulting gas-phase chemistry to be primarily responsible for the damage on the sample at atmospheric pressure at this range from the source. Additional measurements, including XPS analysis of the samples to investigate the SERS-like enhancement argument, are underway. Atomic force microscopy (AFM) could be used to measure any erosion of the sample occurring during exposure, but the material removal rate does not appear to be high.

In order to better understand the molecular damage produced in these experiments, it would be advantageous to study this damage process using a radiation source that will not deposit metal onto the sample. Ideally, a tunable high-energy light source, such as a synchrotron, could be used for irradiation: this would be the best approach to investigating the damage process in these complex molecules.

CHAPTER 7
MICROPLASMA CONCLUSIONS

7.1 Review of results

Microplasmas are sensitive to power, gas pressure and composition, device materials, and construction geometry. This makes reproducibility and comparison between devices difficult. We have demonstrated great improvements in the fabrication and control of microhollow cathode discharges (MHCDs), and demonstrated their use as radiation sources in a variety of applications.

Compared to larger plasma sources, microplasmas operate at lower power, lower discharge voltage, and may be operated with a DC power supply at high pressures, which significantly simplifies their operational requirements. Additionally, these sources are very inexpensive and relatively simple to produce, features which have boosted their popularity in recent years.

We have performed experiments probing the capabilities of these sources for ambient mass spectrometry. Using a windowless MHCD, we have successfully ionized low-molecular-weight neutrals from gas, liquid, and solid phase samples. This was performed without an additional desorption phase, though it was observed that thermal or laser desorption assistance improves results. Most samples observed were protonated ions, and so this technique worked best for samples with high proton affinity. It was concluded that in this experimental configuration, atmospheric water molecules played an important role in the proton transfer process [69]. This device was found to perform

similarly to a DART ionization source, another plasma-based technique, and produced limited fragmentation of sample molecules.

We enhanced the capabilities of the MHCD in atmospheric pressure mass spectrometry applications by configuring the device to produce vacuum ultraviolet photons which could produce sample ions via single photon ionization. By adding a LiF window to our device, we turned off the ionization mechanisms observed in the windowless plasma and studied only the contribution of high energy photons. We investigated the photon energy and total VUV flux from this source, which we found to be comparable to the flux from some commercial Kr discharge lamps [96], and similar on a volumetric basis to a high-intensity Kr excimer lamp [108]. Using this source at atmospheric pressure, we were able to photoionize samples with ionization energies less than ~7.5 eV. By this process, we were able to produce molecular cations with very little fragmentation. We showed that this process was active for a pure Ne MHCD, and was enhanced by adding small amounts (~4-8%) of H_2 to the discharge gas. In VUV light detection experiments, a 4% H_2 mixture produced approximately five times higher signal from the MCP detector compared to a pure Ne discharge.

By reducing the discharge pressure, we were able to change the discharge mode and effectively tune the photon production of the source. In MS experiments, the reduced pressure MHCD was shown to enhance ionization of samples with IEs as high as 9.7 eV, a threshold useful for a wide range of biologically-relevant samples [80]. This work demonstrates the potential of MHCDs to be used as a tunable ionization source for MS, which can enhance analysis capabilities.

A number of optical and electrical measurements have been made of the MHCD in its various configurations, and several figures of merit have been measured for our source. This helps maintain consistency in our source as we continue to develop the apparatus for new experiments, and helps map this part of the microplasma parameter space for the plasma community. We hope this will contribute to the development of more general theoretical models.

Our work highlights the flexibility of microplasmas; this wide adaptability is an aspect of plasma sources that is most interesting and useful in applications like mass spectrometry. One of the fundamental challenges in ambient mass spectrometry is the need to employ a variety of techniques to ensure ionization of an unknown sample. The tunable aspect of the source we have developed is invaluable in this role, as it may reduce or eliminates the need to employ a host of different ionization sources and yet achieve the energetic variety necessary.

As the fundamental understanding of MHCDs and microplasma sources deepens, it is conceivable that the proliferation we have seen in the microplasma community may begin to consolidate. Ideally, a smaller basis set of devices will be able to replicate the operational diversity in ionization sources we now enjoy, simply by adjusting power and gas supplies.

7.2 Future work

The work presented here has demonstrated the application of microplasma technology for atmospheric pressure mass spectrometry, but we have only begun a full study of the fundamentals governing their operation. Establishing sufficient control over the plasma and its environment made these studies quite difficult. The groundwork is

laid, however, for the next phase. A vacuum monochromator should be employed to develop a full spectral map of the plasma. If we can observe the Lyman-α emission line from this source directly, it should be much easier to optimize the MHCD device to encourage its production.

Smaller MHCD devices may improve ionization performance in atmospheric pressure MS applications. As described in [7], enhanced sheath voltage can be found in the transition from the abnormal glow we observe at high pressure to an "obstructed" abnormal glow, which occurs when $pd_{cathode} < (pd_{cathode})_{min}$ (*e.g.*, operation on the left side of the Paschen curve minimum). For the standard Paschen curve in Ne, this minimum $(pd)_{min} \approx 0.1 - 1$ Torr-cm. At atmospheric pressure, this corresponds to a characteristic length of 76 μm. If we reduce our cathode diameter below this limit, we may find enhancement of the plasma energy, though current fabrication methods cannot produce such small holes in the foil-based design. A return to the Si-based MHCD or the development of another strategy will be left as an exercise to the reader. We should be able to confirm this effect in an optical emission experiment, and this would be a prudent first experiment in the continuation of this work.

A host of interesting experiments may be performed with the device as it is now, as well: most of the design features necessary to perform mass spectrometry imaging have been implemented.

More careful study of the electrical measurements will likely be rewarding. In particular, we have not performed any time-resolved measurements. The literature indicates that pulsed operation of these devices increases both output energy and device lifetime [47, 61, 109]. This comes at the cost of some simplicity which makes the MHCD

appealing, but the gains may prove worthwhile. For characterization of the discharge in pulsed or AC operation, time-resolved measurements will be crucial. Pulsed operation in particular would be well-suited to future applications in MS imaging, as it may help to alleviate some of the contrast issues experienced with our early capillary-based DC microplasma design (see §2.1.5).

Our mass spectrometry measurements of small biomolecules ionized by microplasma radiation may have some unobserved effects. It is likely that damage may be produced in these samples below the ionization limit, and so a study of this phenomenon is in order. Particularly, as plasmas become more prolific in clinical applications, as demonstrated by the emerging field of plasma medicine, a more sophisticated comprehension of the effects of radiation damage is desirable. The radiation sources we have developed, however, are probably not well-suited for such experiments, as the broadband nature of their emission would complicate such studies.

CHAPTER 8
THE RELATIONSHIP BETWEEN INTERFACIAL BONDING AND RADIATION DAMAGE IN ADSORBED DNA

We have performed a comparison of the radiation damage occurring in DNA adsorbed on gold in two different conformations, when the DNA is thiolated and bound covalently to the substrate and when it is unthiolated and interacts with the substrate through the bases. Both molecules were found to organize so as to protrude from the surface at ~45 degrees. Distinct differences were found in the N 1s X-ray absorption spectra corresponding to the lowest unoccupied molecular orbitals (LUMO) associated with the N-C=N bond of the isolated molecule. In the case of the adsorbed thiolated DNA, this state is less populated as compared to the adsorbed unthiolated molecules. This is a result of a higher degree of electron transfer from the substrate to the unthiolated adsorbed DNA. Changes in the time-dependent C 1s and O 1s X-ray photoelectron (XP) spectra resulting from irradiation were interpreted to arise from cleavage of the phosphodiester bond and possibly COH desorption. By fitting the time-dependent XP spectra to a simple kinetic model, time constants were extracted, which were converted to cross sections and quantum yields for the damage reaction. These values are significantly higher for the thiolated DNA, probably resulting from the N-C=N LUMO being less populated and hence more effective in capturing of low energy electrons.

8.1 Introduction to X-ray photoelectron spectroscopy of DNA damage

In the following work, a study of DNA damage by soft X-ray and low energy electron irradiation is described. The primary tool for this study was X-ray photoelectron

spectroscopy (XPS). A brief introduction to this technique is in order, since it represents a departure from the methods used in previous experiments.

When discussing “damage” in a molecule such as DNA, we are referring to reorganization in the chemical structure; the breaking and reformation of bonds between the atoms, as well as the outright removal of some parts of the molecule.

XPS is a technique used to observe the chemical structure of sample molecules. The energy of core electrons corresponds to photon energies in the X-ray region, and we are able to eject them from the atom using high energy photon sources [110]. With knowledge of the incident photon energy, we can measure the kinetic energy of the emitted electron and determine the energy of a core state. Core electrons do not participate in chemical bonding, so to first order this energy level does not depend on the structure of the sample. However, small perturbations due to the local chemical environment are observed in these peaks, and by careful fitting we are able to observe changes in the chemical bond structure for different elements as we irradiate the molecule.

This is a powerful technique for the analysis of DNA damage, since it affords us location-specific information about how the structure of our molecule is modified in the course of the experiment.

8.2 Overview

High energy ionizing irradiation produces large amounts of low energy (<20 eV) secondary electrons (SEs). These electrons are produced via a cascade process following the ionization of a core (deeply bound) electron. Due to their low energy there is a high probability for the SEs to become trapped in antibonding orbitals, via resonant scattering,

forming a temporary negative ion (TNI) resonance. If the lifetime of the TNI state is long enough, then bond rupture can occur by by a process known as dissociative electron attachment (DEA). Sanche and coworkers showed how low-energy electrons produce complex DNA damage by a DEA process [111]. Electrons that have slowed down to energies too low to induce ionization of DNA undergo resonant attachment to DNA bases. It has been shown that these electrons, once captured, are efficiently transferred to the sugar-phosphate backbone [112-113], causing the breaking of one or both strands of the DNA. One electron can in this way produce multiple lesions, thus amplifying the clustering of damage induced in DNA by a single radiation track [114]. Clustered lesions are difficult for the cell to repair and are therefore more likely to lead to permanent damage to the genome [115]. Recent work using Raman microspectroscopy has shown that substrate interactions and the specific base pair sequence affects the single strand break probability via low energy (< 5 eV) shape resonances [116].

Radiation therapy and radiosensitization applications take advantage of the fact that the local environment and bonding of DNA can have a profound impact on the effectiveness of low energy electrons. For instance it has been shown that binding of just two cisplatin molecules to a 3,197 base pair plasmid increases the number of single strand breaks caused by 10 eV electrons by nearly four times [117]. Also, the insertion of gold nanoparticles in the vicinity of DNA in cancer cells can lead to an increase in the number of low energy secondary electrons. The gold nanoparticles preferentially concentrate in subcutaneous tumors and thus have applications as radiosensitizers in cancer treatment [118]. Furthermore, the orientation of DNA on the gold surface has been

shown to affect the OH^- yield induced by low energy electrons [119]. However, the effect of the DNA-gold bond on the reaction rate has not been studied.

There is vast literature on the role of TNI states and DEA in DNA related radiation chemistry [120-124]. We have recently found that if the SEs are spin polarized, then chiral-specific radiation chemistry may result [125]. Due to its high flux density, synchrotron radiation (SR) has often been used to induce and study radiation chemistry in numerous systems [126], including DNA and related molecules [127-134]. SR has also been used to probe the electronic structure and bonding of such molecules, primarily by probing the occupied states with X-ray photoelectron spectroscopy (XPS) and the unoccupied states with X-ray absorption (XAS) measurements. Bond overlap and localization can be revealed by XPS while XAS can determine the density of unoccupied states and the orientation of the orbitals [135-147]. Resonant photoemission (combining XPS and XAS) can be used to determine the lifetime of the excited state with 100 femtosecond precision [148-149]. It is expected that the extent of occupation and the lifetime will play a critical role in determining the nature of the TNI state and thus the efficiency of the DEA process. However, to our knowledge there has been no direct study on the correlation between the lowest unoccupied molecular orbital (LUMO) occupation and radiation damage.

In the present paper we examine X-ray induced reactions of DNA adsorbed on a gold substrate when the DNA is either thiolated (tDNA) or when it is unthiolated (uDNA). By performing polarization-dependent X-ray absorption spectroscopy at the N K edge we determined that the thiolated DNA protrudes from the surface at ~45 degrees, in agreement with previous studies [136, 150]. We also found that the unthiolated

molecules have a similar orientation. However, due to differences in charge transfer between the gold and the DNA in the two systems there is a higher density of unoccupied states in the N-C=N derived π^* orbital for tDNA. We also found that the adsorbed tDNA has a significant higher cross section for radiation damage. The reason for this enhancement could arise from the greater probability of forming a TNI state for the tDNA due to the higher density of unoccupied π^* states.

8.3 Experimental

The samples were prepared at the Weizmann Institute according to a method described previously [151-152]. They consisted of 40 base pairs of 3' thiolated as well as unthiolated DNA on a clean 200 nm thick polycrystalline gold film on a Si substrate. The exact sequence was:

5' - TCT CAA GAA TCG GCA TTA GCT CAA CTG TCA ACT CCT CTT T -3'

3' - AGA GTT CTT AGC CGT AAT CGA GTT GAC AGT TGA GGA GAA A -5'

The samples were shipped in sealed vials under a nitrogen atmosphere to laboratories in the United States and not opened until shortly before they were loaded into a load lock chamber, which was immediately evacuated. Work functions of single-stranded variants were determined at the Weizmann Institute according to a method described previously [153].

The measurements for these experiments were performed at two different synchrotron radiation sources. Experiments utilizing X-rays in the range 500 to 1000 eV were performed on beamline 4-ID-C at the Advanced Photon Source (APS). The angle (Φ) between the incoming X-ray beam and the sample surface was 55 degrees and the emitted electrons were detected by a CLAM 2 electron energy analyzer, oriented at an

angle θ of 35 degrees (Figure 8.1) and operated at a pass energy of 50 eV, except for the P 2p results, which were obtained using 100 eV pass energy.

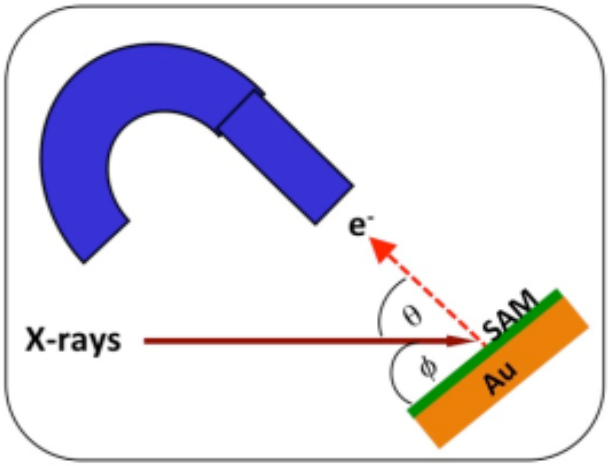

Figure 8.1 Schematic diagram of the experimental setup for XPS experiments.

All X-ray photoelectron spectroscopy (XPS) data were taken at a photon energy of 950 eV. The total electron yield (TEY) from the electrically isolated sample was determined by measuring the restoring current using a current amplifier. The APS measurements were performed with the storage ring operating in “top up” mode so the X-ray flux density was constant to within 1-2 % during all measurements at a given energy. XPS and polarization-dependent near-edge X-ray absorption fine structure (NEXAFS) measurements at the N K edge (400 eV) were carried out on the HERMON beamline at the Synchrotron Radiation Center (SRC). NEXAFS data were acquired by measuring the TEY emitted from the sample. The spectra were normalized to the beamline flux by measuring the electron yield from a partially transmitting gold mesh inserted into the X-ray beam. To minimize possible effects of radiation damage, each NEXAFS scan was acquired at a fresh spot on the sample. XPS data were acquired with a cylindrical mirror

electron energy analyzer (CMA) oriented at 90 degrees with respect to the incident photon beam.

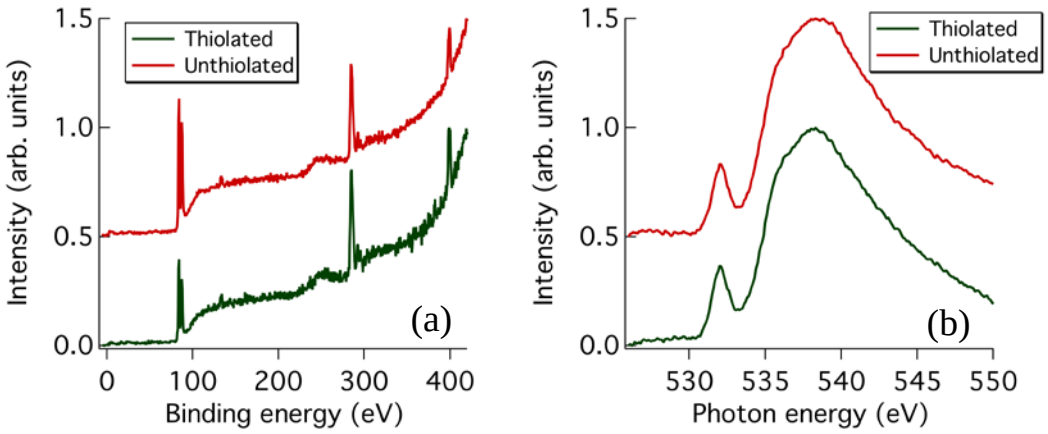

Figure 8.2 (a) Survey XPS spectra of thiolated (bottom) and unthiolated (top) DNA adsorbed on Au taken with 500 eV photons at the SRC. (b) O 1s X-ray absorption spectra of thiolated (bottom) and unthiolated (top) DNA adsorbed on Au taken at the APS.

Characterization of the samples was done at both APS and SRC. Figure 8.2(a) shows survey XPS spectra of tDNA and uDNA acquired using 500 eV X-rays at SRC. Both samples show characteristic C 1s (285 eV) and N 1s (400 eV) DNA peaks as well as Au 4f peaks (~84 eV) from the substrate. Note that the DNA signals are stronger and the Au 4f peaks are smaller for tDNA indicating that the tDNA coverage is slightly higher than that of uDNA. Oxygen K X-ray absorption spectra of both samples, obtained at the APS, are shown in Figure 8.2(b). Both spectra are similar to each other and to previously reported results [127, 129, 144, 147, 154-155].

8.4 Results and Discussion

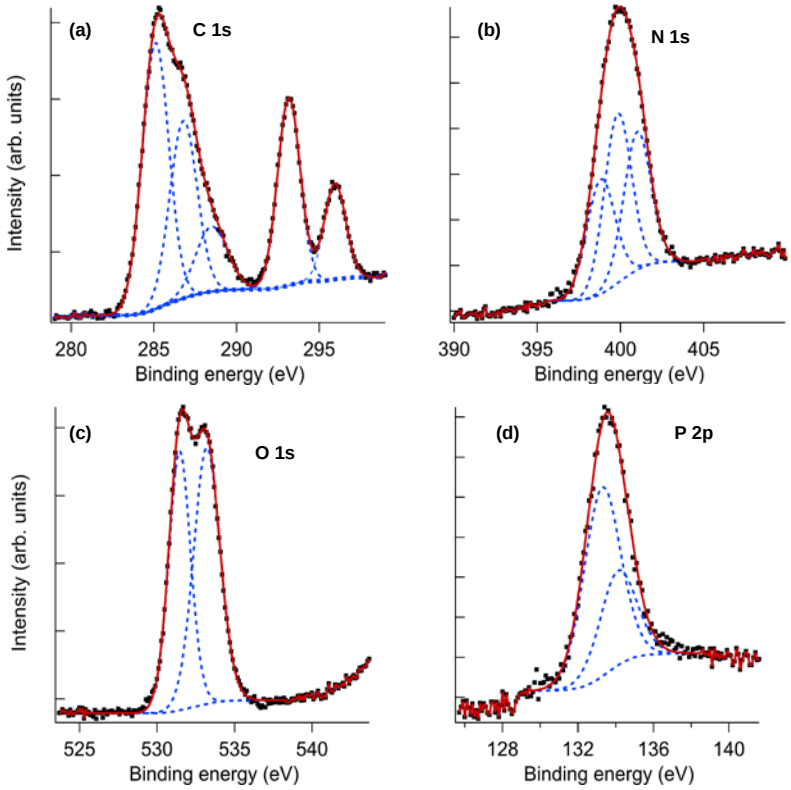

Figure 8.3 Core level XPS of thiolated DNA adsorbed on Au taken with 950 eV X-rays at the APS. (a) C 1s and K 2p (b) N 1s (c) O 1s (d) P 2p. The points are the experimental data, the dashed lines are fits to individual components (see Table 8.1) and the solid line is the fitted envelope.

Core level XPS data obtained at 950 eV at APS from tDNA are shown in Figure 8.3. These spectra are the result of signal averaging up to 30 individual spectra taken at the same position. During the course of these measurements significant changes were observed in the individual components that make up the spectral envelope in the case of C 1s (a) and O 1s (c), but not for N 1s (b) and P 2p (d). These changes will be dealt with in depth later in the paper. The results shown in Figure 8.3 are similar to previously reported spectra of DNA and related molecules [135, 139, 142, 156-157]. Due to the complex chemical environment of the C, N, O atoms in DNA each core level peak is

composed of two or more components. To gain insight into the energies of these components, curve-fitting techniques were employed. For these spectra most of the peak width is due to instrumental broadening, so the peaks were fit using components that carried a 10 % Lorentzian, 90 % Gaussian peak shape. The minimum number of components that resulted in a reasonable fit was utilized. These components, along with their assignments, are shown in Table 8.1. The spectra and their components are in reasonable agreement with previously reported results [139, 158], considering the lower resolution of the present work.

Polarization-dependent N NEXAFS obtained using linearly polarized light from both forms of DNA are shown in Figure 8.4. The two sharp peaks at 399 and 401 eV are due to N 1s excitation to π^* orbitals which are localized on the base pairs, while the broad peak at 407 eV is due to excitation to σ^* orbitals. The 401 eV peak has been assigned to core level excitation of a nitrogen bound to a carbonyl group and the 399 eV peak arises from excitation of the remaining nitrogen atoms [139]. As the angle between the X-ray beam and the sample normal increases, the E vector becomes more aligned with the π^* orbitals of the base pairs for the protruding DNA. This enhances the N 1s $\rightarrow$ π^* intensity as has been observed in previous studies on tDNA [136, 140, 143]. To our knowledge there have been no previously reported polarization-dependent N NEXAFS studies on uDNA, such as those shown in Figure 8.4(b). The spectra of the two types of DNA are similar except for the enhancement of the 399 eV peak in the case of tDNA.

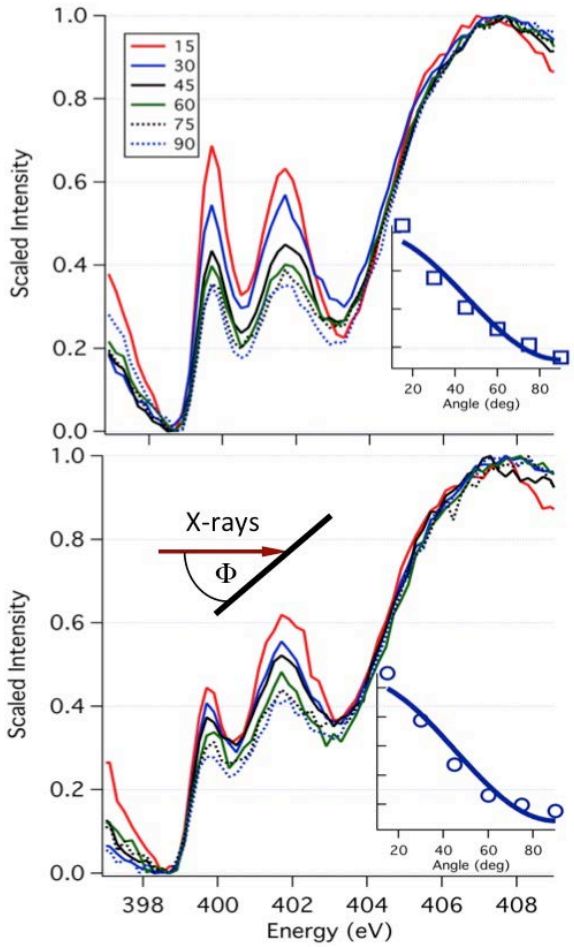

Figure 8.4 Polarization-dependent N 1s X-ray absorption spectra of thiolated (top) and unthiolated (bottom) DNA adsorbed on Au taken at the SRC. The insets show the angular dependence of the π* resonance at 399 eV for thiolated DNA and 401 eV for unthiolated DNA. The symbols are the experimental data and the straight line is a fit to the model discussed in the text.

To determine the orientation of the DNA on the gold surface, the areas of the 399 eV peak (tDNA) and the 401 eV peak (uDNA) were extracted using curve fitting techniques [159]. These areas are plotted as a function of angle in the insets of Figure 8.4(a) and Figure 8.4(b). For 100% linearly polarized light, the following equation describes the angular (θ) dependence of the π* orbital [137]:

$$I(\theta) = \frac{A}{3} \cdot \left[1 + \frac{(3\cos^2\theta - 1)(3\cos^2\alpha - 1)}{2}\right] \qquad \text{Equation 8.1}$$

A is a constant, θ is the angle between the polarization vector and the sample normal, and α is the polar angle between the vector of the π* orbital and the surface normal. The solid line in the insets in Figure 8.4 is a fit to this equation and yields angles α of 43° ± 2° for tDNA and 44° ± 2° for uDNA, which is in agreement with previously reported results for tDNA [136, 150]. Therefore, the two types of DNA are oriented in a similar fashion, although the coverage is lower for uDNA.

NEXAFS spectra map out the local density of unoccupied states. The spectral differences between the two types of DNA seen in Figure 8.4 reveal changes in the N-related unoccupied levels that occur as a result of dissimilar substrate-bonding interactions. For tDNA it is well established that bonding to the gold substrate occurs through the thiol group [160], which results in a net transfer of holes to the tDNA and electrons to the gold [152]. Polarization modulation infrared reflection absorption spectroscopy data obtained on these samples also indicate strong gold-base interaction (data not shown). For uDNA bonding to the Au substrate likely occurs through a primary amine group on one of the bases [161-163], most likely the adenine base [156]. The Au-N bond has a weaker binding strength and higher contact resistance than the Au-S bond [164], which should result in less charge transfer between the Au and the uDNA. This is reflected in the NEXAFS spectra in Figure 8.4; the greater intensity of the 399 eV peak for tDNA as compared to uDNA is due to more holes being injected into the tDNA through the Au-S bond. Analogous changes in N 1s → π* intensity have been seen for N_2O adsorbed on a metal surface where the peak intensity resulting from excitation to an orbital localized on a particular N atom was reduced when that atom was coupled to the

surface [165]. The increased electron transfer from tDNA to gold is also supported by our work function measurements made on single-stranded variants. For the bare gold surface the work function was found to be 4.88 eV, for the thiolated sample it was 4.45eV, while for the unthiolated DNA it was 4.57 eV (all measurement errors are less than 0.05 eV).

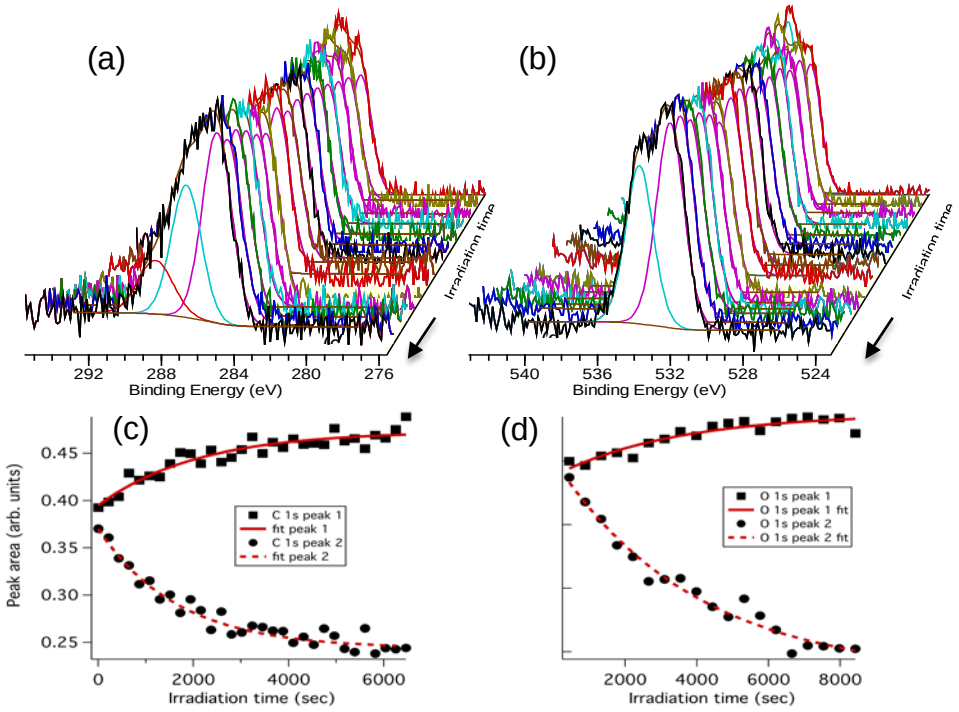

Figure 8.5 Series of irradiation time-dependent XP spectra: (a) C 1s (b) O 1s. Also shown are the deconvoluted spectral components. Irradiation time dependence of the areas of peaks 1 and 2 (see Table 8.1) for (c) C 1s (d) O 1s. The symbols are the experimental data and the straight line is a fit to the model discussed in the text.

Irradiation time-dependent C 1s and O 1s XPS spectra for tDNA are shown in Figure 8.5(a) and (b). The peak-fit extracted areas of components 1 and 2 (Table 8.1) are plotted as a function of irradiation time in Figure 8.5(c) and (d). Component 1 for C (C-C, C=C) and O (C=O, P=O, P-$O^-(K^+)$) increased and component 2 (C: C-O, C-N, C-NH_2, N-C-N, N=C-N) (O: C-O-P, C-O-C) decreased with time, but the attenuation of component 2 was higher than the rise in component 1. Component 3 of the C 1s data also decreased with

time, but due to its weak intensity the data were noisier than that of component 2. The overall intensities of the C 1s and O 1s peaks decreased by ~10 %. No significant changes were observed in the N 1s or P 2p XPS spectra under these conditions. Using the kinetic relationship,

$$I = I_0 e^{-t/\tau}, \qquad \text{Equation 8.2}$$

where I = peak area, I_0 = initial peak area, and t = time. We are able to extract the time constants, τ, for the reactions resulting in a decrease in the area of a component. Similar first order kinetic treatment yields the equation

$$I = I_0\left(1 - e^{-t/\tau}\right) \qquad \text{Equation 8.3}$$

for components that increase [166]. Results of fitting the data to these equations are shown as the lines in Figure 8.5(c) and (d). The derived time constants for the decreasing and increasing components for both C 1s and O 1s XPS data were the same, within experimental error.

Based on the assignments in Table 8.1, the decay of peak 2 in the C 1s spectra indicates the loss of C-O or C-N bonds and the rise in peak 1 indicates the formation of C-C or C=C species. Similarly the changes in the O 1s spectra indicate the loss of C-O-P and C-O-C species and the formation of C=O, P=O, or P-O^-(K^+) bonds. The similarity of the time constants for all the reactions suggests that these processes are correlated. Since no significant changes were observed in the N 1s spectra, reactions involving the base pairs appear to play a minor role under these conditions. Fission of the C-NH_2 bond would lead to an overall decrease in intensity, and loss of carbonyl species would result in changes of the relative intensities of peak 1 and peak 2. Cleavage of the *N*-glycosidic bond is also consistent with this result. However, due to the relatively poor resolution,

slight changes in the relative intensities of the two components of the N 1s spectra would not be noticeable, but it is clear that there was no significant loss of N-containing species during the reaction.

In previous time-dependent XPS measurements of X-ray irradiated DNA [157], Ptasinska, *et al.* observed behavior that differed from that of the present work. They reported a significant decrease in the O 1s signal and smaller reductions in the N 1s and P 2p intensities; the overall C 1s signal increased. These experiments were performed using a laboratory XPS system and fairly thick films of plasmid or calf thymus DNA on Si or Ta substrates. Xiao, *et al.* also reported time-dependent XPS results [167] at variance with the present study in the cisplatin-DNA system. They showed an ~50% decrease in the O and C 1s signals and ~20% reduction in N 1s and P 2p intensities following 3 hours of irradiation with a laboratory x-ray source. Since it has been shown that substrate-DNA interactions [116, 119] and morphology [168] can have a profound effect on its radiation chemistry, it is not surprising that the present results are not consistent with this previous work.

The amount of water coadsorbed with the DNA can also influence the radiation chemistry [120, 169]. Although these measurements were made under ultra-high vacuum conditions, it is possible that some water remained. However, there is no indication of a water peak at ~535.4 eV [170] in the O 1s XPS data in Figure 8.3(c), so it should not be a major factor.

It has been well established that one of the main mechanisms for low energy electrons to produce strand breaks (SBs) in DNA is by phosphodiester bond cleavage [121-122, 171-172]. The mechanism is thought to involve decay of the transient radical

anion of the phosphate π* orbital to the strongly dissociative C-O σ* orbital [172]. This would result in loss of C-O-P species, formation of $P\text{-}O^-$ and $C\text{-}C^\bullet$ bonds and would be consistent with the results shown in Figure 8.5. If the reaction also led to COH loss by decomposition of the sugar molecule [157, 173], this could account for the 10 % decrease in overall C 1s and O 1s XPS signals. Although it is not possible to rule out other minor pathways, such a reaction scheme should be a major factor in the overall X-ray induced reaction.

By performing numerous measurements of the time constants for the decay rate of component 2 of the C 1s peak (Figure 8.5 (c)), it was possible to extract cross sections for the reaction for both tDNA and uDNA. The cross sections (σ) were determined using the relationship $\sigma = 1/\tau * f$, where τ is the time constant and f is the flux density. A photodiode was used to measure the flux and the beam size was determined using a wire scanner; the resulting flux density was 2 $x10^{14}/cm^2$. Since secondary electrons are thought to play a prominent role in the reaction, cross sections for electron-induced reactions were also determined by measuring the TEY for the samples and converting it into an electron flux density using the measured spot size. Due to the lower coverage, the TEY for uDNA was ~30% higher than for tDNA. To take into account the differences in coverage from spot to spot and from sample to sample, the quantum yield (QY) was also calculated by multiplying σ by the surface coverage [174]. The coverage was taken to be proportional to the total C 1s peak area for the first spectrum of a given photolysis series, and the average coverage for tDNA was set to 1.4 x 10^{13} molecules/cm^2 [112]. Results of these calculations for tDNA and uDNA using both the photon and electron flux density are shown in Table 8.2. Although the given absolute cross sections and quantum yields may

have large systematic errors, due to uncertainties in measurements of the coverage, x-ray beam size and flux, the relative values should be accurate to within the stated uncertainties. Despite the systematic errors, note that the absolute cross sections are in the same range as those reported for DEA to 2-deoxyribose [175], and the per-nucleotide value for plasmid DNA [176].

The overall conclusion from the results in Table 8.2 is that the radiation damage process is more efficient for tDNA as compared to uDNA. The ratios of the σ or QY values for thiolated versus unthiolated range from 1.2 ± 0.1 to 1.9 ± 0.2. A possible reason for this effect may be gleaned by examination of the N 1s X-ray absorption data shown in Figure 8.4. Due to the relatively strong coupling between tDNA, as compared to uDNA, and the gold susbtrate, more holes are injected into tDNA. For Au-S the bond strength is ~40 kcal/mol, while for Au-N the bond strength is estimated to be 8 kcal/mol [164]. As a result there is a significantly higher density of unoccupied states for the lowest unoccupied molecular orbital (LUMO) associated with the N-C=N states for tDNA, as revealed by the greater intensity of the peak at 399 eV [139]. Similar phenomenon in which the gold substrate contributes to the adsorbate's state was observed for semiconductor nanoparticles adsorbed on gold via alkyldithiols [177].

Therefore, due to the higher N-C=N LUMO density for tDNA, there is a greater probability for capture of a low energy secondary electron generated by the X-rays. It has been shown that low energy electron induced SBs in DNA depend on the electron capture probability of the DNA bases. Once captured, the electrons transfer from the base to the phosphate group and cause C-O bond rupture by a DEA process [172, 178-180]. Experiments and theory indicate that the process is enhanced by excitation of π* shape

resonances and/or Feshbach resonances [116, 121-122, 169, 172, 181]. Electron transmission measurements indicate that the number of guanine bases controls the electron capturing efficiency, perhaps as the result of its large dipole moment [112-113, 153]. The present study is the first to correlate the radiation damage process with the nature of the unoccupied states in two DNA species that differ only in the way they are bound to the surface. Our results support the importance of low-lying π^* states in radiation damage caused by low energy electrons.

8.5 Conclusions

In summary, we have examined the X-ray induced radiation chemistry of the same double stranded DNA molecule adsorbed on a gold surface in two different configurations. The first is indirectly bonded via a thiol group whereas the second involves direct, though weaker adsorption, via the nitrogen on a base such as adenine. By examining polarization-dependent N 1s X-ray absorption spectra, both species were found to be oriented to the surface at ~45 degrees, but the thiolated DNA had a higher density of LUMO states. Time-dependent XPS spectra revealed changes in the C-O bonding following irradiation, which were thought to be the result of the interaction of low energy secondary electrons. The results are consistent with a model involving cleavage of the phosphodiester bond and possibly COH loss by decomposition of the sugar molecule. Time constants for the reaction were obtained by fitting the time-dependent XPS data to a simple kinetic model, which were then converted to cross sections and quantum yields for the reaction. The overall reaction rate is significantly higher for the thiolated DNA, which we conjecture is a result of its higher density of LUMO states. This leads to more efficient capture of the low energy electrons by the

bases, hence to a higher degree of phosphodiester bond cleavage following electron transfer to the phosphate group. It is interesting to note that one of the main differences between the present results and prior studies of X-ray damage on thick DNA films is that little or no reactions involving N were observed here, whereas substantial N radiation chemistry was observed in the thick film work. We speculate that directly bonding the DNA to the substrate in the present work may shorten the lifetime of the repulsive state that leads to nitrogen release, thereby effectively quenching that reaction. These studies emphasize the importance of understanding the influence of local bonding in biomolecules in order to comprehend the manner in which low energy electrons produced by irradiation induce chemical reactions in these systems.

8.6 Supplemental

Table 8.1 Binding energies of the components in Figure 8.3 and their chemical assignments [139].

Core level	Peak	|BE (eV)	Chemical moiety
C 1s	1	285.1	C-C, C=C
	2	286.8	C-O, C-N, C-NH_2, N-C-N, N=C-N
	3	288.5	N-C-O, N-C=O, N-C(=O)-N
N 1s	1	399.6	C-NH_2, C=N-C
	2	401.1	N-C-O, N-C=O
O 1s	1	531.5	C=O, P=O, P-$O^-(K^+)$
	2	533.2	C-O-P, C-O-C
P 2p	1	133.3	$2p_{3/2}$
	2	134.1	$2p_{1/2}$

Table 8.2 Values of the cross section and quantum yield for tDNA and uDNA calculated using the X-ray or electron flux density.

	Thiolated (t)	Unthiolated (u)	Ratio (t/u)
X-ray cross section (Mb)	3.1± 0.2	2.5 ± 0.2	1.2 ± 0.1
Electron cross section (Mb)	5.5 ± 0.3	3.6 ± 0.3	1.5 ± 0.1
X-ray quantum yield ($x10^{-5}$)	4.0 ± 0.2	2.6 ± 0.2	1.5 ± 0.1
Electron quantum yield ($x10^{-5}$)	7.2 ± 0.4	3.7 ± 0.3	1.9 ± 0.2

8.7 Acknowledgements

The work performed at the Advanced Photon Source was supported by the U.S. Department of Energy, Office of Science, Office of Basic Energy Sciences under Contract No. DE-AC02-06CH11357. This work is based in part upon research conducted at the Synchrotron Radiation Center, University of Wisconsin-Madison, which is supported by the National Science Foundation under Award No. DMR-0537588. TMO and JMS wish to acknowledge support from the U.S. Department of Energy, Office of Basic Energy Sciences under Contract No. DE-FG02-02ER15337. We would like to thank Nir Eliyahu for experimental support.

APPENDIX A

PROCESS FOR FABRICATION OF WAFER-BASED MHCD DEVICES

Details for fabrication of Si-based MHCD devices.

A.1 Optional step: electroplated electrodes

Optional step: electrode layer thickness enhancement by electroplating.

1. Steps 1-5 are performed as described in §2.1.1.1
2. A thin Ni layer (~100 nm) is deposited over the entire wafer by e-beam evaporation.
3. A photoresist mask is added to the wafer, revealing only the portions meant to be developed into cathode material (excluding cathode holes and margins)
4. Using a wet electroplating process, a thick (~100 μm) layer of Ni is anisotropically deposited on the wafer.
5. Photoresist layer is stripped off
6. Using a brief HCl wet etch, Ni is removed from the wafer until only the thick regions remain.
7. Wafer is diced as usual.

A.2 Lithographic Recipe for producing MHCDs

Note: See final pages of Pettit cleanroom notebook for additional details. Best process was used for production of wafers #1-4.

1. Deposit ~7 µm SiO_2 via PECVD
    a. Oxford PECVD Recipe: Standard library recipe 2012-08-27
        i. Table temp: 300 °C
        ii. Pressure: 1000 mTorr
        iii. Power: 20 W
        iv. Gas flows: 8.5 sccm SiH_4 / 710 sccm N_2O / 162 sccm N_2
        v. Deposition rate: ~62 nm/min
        vi. 40 minute maximum consecutive run: run clean step on chamber in between deposition steps. (clean time >= deposition time)
    b. Unaxis PECVD Recipe: 60 min. standard oxide
        i. WATLOW 250 °C
        ii. Gas flow: SiH_4 400 sccm / N_2O 900 sccm
        iii. Pressure: 900 mTorr
        iv. Power: 25 W RF / 2 W DC
        v. Deposition rate: 53.3 – 53.5 nm / min
    c. Unaxis Clean process
        i. WATLOW 250 °C
        ii. N_2O 40 sccm / SF_6 160 sccm

iii. 200 mTorr

iv. 350 W RF / 9 W DC

2. Coat wafer with ~14-15 µm HMDS (not strictly necessary, but helps)
    a. Tool: Karl Suss RC8 Spinner (Pettit)
        i. Spread 18 s @ 400 rpm
        ii. Spin 80 s @ 1000 rpm
3. Coat with ~15 µm photoresist mask
    a. PR: SPR-220
    b. Spin coat RC8
        i. 6 mL resist at room temperature. Don't be stingy. Remove all bubbles with pipette.
        ii. 30 s @ 400 rpm spread
        iii. 80 s @ 1000 rpm spin
        iv. Soft bake for 360 s on 105 °C hotplate
        v. Measure temperature: hotplates are often inaccurate, and this is somewhat sensitive.
    c. UV Exposure
        i. ~1200 – 1400 mJ. (Still adjusting this value)
        ii. Hard contact
    d. Rest 3 hours (optional?)
    e. Post-exposure bake (PEB) on 110 °C hotplate for 300 s
    f. Rest 45 minutes for rehydration

g. Develop in Microposit MF 319, agitating continuously for approximately 225 seconds. Measure features under optical microscope to determine development time.

h. Results: 15.3 – 15.5 µm thick PR layer with 112 µm hole from 125 µm mask pattern

4. Mount wafer to carrier wafer with Cool Grease (necessary for any through-wafer etch).

    a. Apply a thin layer with a swab to the back of the wafer, leaving 5-10 mm margin at the edge of the wafer to prevent squeeze-out.

    b. Bond together on hotplate at 110 - 120 °C for ~60 s

5. Etch SiO_2 in exposed areas

    a. Tool: PlasmaTherm ICP

    b. ~35-40 min C_4F_8 etch process for a 7.1 µm SiO_2 layer.

    c. Pressure: 4.9 Torr

    d. He Flow: 3.53 sccm / Pressure: 4.68 Torr

    e. Ar: 5.0 sccm / C_4F_8: 15.0 sccm / CO_2: 28.0 sccm

    f. Power: RF1: 40 W (0 W reflected) / DC: 155 W / RF2: 802 W (4.9 W reflected)

6. Etch Si (using remaining PR and SiO_2 as mask layers)

    Note: this step has been problematic, since my wafer patterns have many different feature sizes. A mask with uniform feature size should be much more controllable.

Larger features etch more quickly than smaller ones, and once the backing wafer (and Cool-Grease) has been reached, etch rate drops significantly in smaller features.

   a. Tool: STS ICP
   b. Recipe: saved as “joshsmod”
      i. Param switching on
      ii. Select process time by number of cycles
      iii. Pressure: Manual APC, 68.4%
      iv. Gas: 100 sccm C_4F_8 etch, 10:1 SF_6:O_2
      v. RF Power: 10 W (very sensitive!)
      vi. Expected rate: ~0.5 – 0.6 µm / cycle Si etch
   c. Process runtime: 300 cycles (90 minutes) between checking.
   d. Largest features developed after 600 – 800 cycles, and the smallest features were still undeveloped after 1400 cycles (7 hours).
   e. Monitor progress with profilometer (e.g. KLA Tencor P-15)
7. Deposit Ni seed layer with E-beam evaporator
   a. ~100 nm total thickness
   b. ~3 Å/sec deposition rate

   (Finishing steps, not yet performed)
8. Deposit photoresist mask exposing areas to be metallized
9. Plate wafer with 100 µm of Ni from solution
10. Strip mask, etch in HCl to remove seed layer from masked areas.

APPENDIX B

PROTOCOL FOR MHCD OPERATION

Steps for setting up and running experiments using the gas mixing manifold and computer control.

B.1 Evacuating the manifold

- Close ALL the valves in the mixing manifold and gas supply lines.
- Exceptions: "bellows" valve between mixing manifold and mix bottle, and mix bottle valve itself. Leave these two open, unless you're not making a new gas mixture.
- Bellows valves (in general) need **not** be turned very tightly to be very closed; just a little bit will do, especially the Swagelok (larger disc) handles.
- Proper tightness might be the minimum amount of force required to call it "firm".
- Nu-pro valves (smaller handles) probably require the same torque, but it feels harder because of the smaller handle.
- When valves are open, don't open them 100% of the way, so it's easy to tell if a valve is open or closed with very gentle jiggling.
- Double check.
- Open Baratron Interpreter program in LabVIEW.
- Turn on Agilent meter which reads the Baratron
- Make sure Baratron + supply is on (preamp power supply)
- Read Baratron pressure. This reads absolute pressure in Torr
- This is as opposed to "gauge" pressure, which is what you see on most gauges.
- absolute pressure = gauge pressure + 1 atm (14.7 psi, 760 torr)
- Open any high pressure lines that need to be roughed out. For regular mixing, this should only be "Bellows" and "Bottle", as mentioned above.
- **For intensive gas purging** also open "Mix" and "Ne Man". This opens the gas line from the Ne bottle (which should remain closed!) to the mixing manifold so it can all be evacuated.
- Rough out mixing manifold
- If there is substantial pressure in mixing manifold, it may be easiest to let it all leak out through MFC 1 first.
- Connect the black "Aux Vac" line to the white tubing attached to the "Rough" valve
- When pressure is reasonable, close 3-way valve on roughing foreline to prevent over-backpressure to turbo pump.
- This should only be done when UHV chamber pressure is reasonable (> 10^-7 torr or so), as the turbo will now have no backing pump
- With that in mind, **do not leave 3-way valve closed too long!** A few minutes is fine, but hours would probably be catastrophic.

- Open Aux Vac valve
- Open Rough valve
- You should now see Manifold pressure change. It may go up or down, depending on how low the pressure was originally.
- The aux vac leaks; don't expect the pressure to be very low.
- **Slowly** open "High P" valve.
- Manifold pressure will spike. Ideally this should be kept less than max (<10^3 torr)
- Pressure at manifold convectron gauge must **NEVER exceed 2500 torr** (absolute pressure).
- This corresponds to 4.8 V as read by the Agilent meter.
- It may pop or become permanently damaged if pressure is exceeded.
- Watch foreline pressure as an indication of gas load. This pressure should stay reasonable (ideally <1 torr) during pumping.
- As foreline pressure improves, open High P valve further. Once both pressures are within reasonable ranges you can crank it open all the way.
- With rough vac valves fully open, wait for a few minutes until manifold pressure reaches 10^-2 range. Make it as low as your patience allows, it will make the next step easier.
- During this time, when foreline pressure is reasonably low, **reconnect 3-way valve** to turbo pump by pointing the handle toward the turbo.
- Close "Rough" valve.
- Close Aux Vac valve
- Open 3-way valve to the turbo, if you have not already. **It must be open for next step!**
- With ~10^-2 torr in mixing manifold, **SLOWLY** open UHV valve.
- Watch ion gauge controller as you do this. Make sure pressure stays <~9x10^-4 torr (ideally 10^-5 torr). If it gets too high, stop opening, or close a tiny bit and wait for the pump to catch up.
- As pressure starts to come down on ion gauge, open valve fully.
- Wait.
- For gas mixing, manifold convectron pressure should reach mid 10^-3 torr, and UHV chamber pressure might reach 10^-7 torr.
- Gas lines besides the mixing manifold may be somewhat leaky and your pressure will get better after you close these off.
- When desired pressure is reached, close High P valve. (This segment is also a bit leaky, pressure will improve if you let it keep pumping)
- Close UHV valve.
- Congratulations! The manifold is empty. Now fill it with gas.
- Make sure you reconnected that 3-way valve to the turbo.

B.2 Making a gas mixture

- Open H_2 mix calculator 2.1 LabVIEW program
- Enter desired targets: total pressure and H_2 concentration.
    - Usually you want as much total pressure as possible for more experiment runtime.
    - There is a tradeoff between total pressure and H_2 concentration, which is limited by the amount of H_2 you are able to stuff into the mixing manifold.
    - Feel free to overshoot total pressure target; the program will adjust.
- Select valve on front panel: "bellows" or "bottle". These correspond to the labeled valves on the mixing manifold.
- By using the bottle valve, you allow the mixing volume to be larger compared to the storage volume, allowing slightly higher concentrations.
- Hit "Run Continuously".
    - The program will go through values until it finds ones that fall within the limits.
    - Make sure both Initial pressures are possible (<5100 torr; this pressure is the maximum allowed by the Baratron gauge (~100 psi)).
    - Actual H_2 limit may be lower as we deplete the bottle.
- Initial Ne and H_2 pressures correspond to voltages to be read off Agilent meter (via Baratron interpreter sub-vi).
-
- **Evacuate** mixing manifold
- Carefully **purge** MFC 1 with pure Ne (described in Gas Handling protocol; set up as if you are running the plasma through MFC 1)
    - This may be done simultaneously as evacuation is taking place (if you are careful not to expose UHV chamber to high pressure gas)
    - After purging, stop flow controllers and close MFC 1 valve.
- After evacuation completes, close: UHV valve, High P valve, MFC 1 valve.
- For security, close Ne bottle valve. This will prevent catastrophic loss of all our neon if something bad happens.
- With all sensitive chambers carefully sealed, open Mix valve.
    - With Ne bottle valve closed, this pressure should drop significantly and then stop at some low value.
    - Open Ne bottle valve and it will fill the mixing volume.
- **Fill manifold with Ne**: Adjust regulator 0 until baratron matches Initial Ne pressure
    - If you overshoot a little, turning the regulator back down a small amount may help.
    - Perfect accuracy is not critical, just record the actual value.
- Close chosen mix valve (either Bellows or Bottle). Your initial Ne volume is stored.
- **Close all the Ne valves** that you no longer need: Ne bottle valve, Ne man valve, Mix valve, MFC 1 valve.

- **Evacuate** the rest of the manifold as before. Do not include Ne manifold. **Make sure to close UHV** again!
- When a good pressure is reached, turn H_2 regulator knob counter-clockwise to reduce output pressure.
    - When the knob starts to fall off, you've gone plenty far.
- Open H_2 valve, filling the mixing manifold with hydrogen.
- **Fill manifold with H2:** Adjust H_2 regulator knob until desired Initial H2 pressure is reached.
    - Usually you will be cranking it up as far as it will go.
- When desired H2 pressure is reached, close H_2 valve and reduce H_2 regulator pressure
    - Note actual H2 pressure, and enter into mix calculator. This value with the actual Ne pressure should calculate your actual concentration: record this
    - Enter mix concentration in Plasma Controller program and save value as default in program. Make sure to select proper mix gases in the dropdown menus.
    - Indicated pressure may not actually drop, but unscrewing the knob ensures that H2 won't leak out unchecked if the line becomes disconnected.
- **Open** Bellows valve and Bottle valve, combining Ne and H2 volumes.
    -
- Congratulations! You have a new gas mixture. The new indicated pressure should match the calculated total pressure in the mix program.
- Open Mix valve and MFC 1 valve and you are ready to perform experiments with the gas mixture.
    - As noted previously, you may want to bleed out some of the excess Ne pressure in MFC 1 before opening Mix valve in order to decrease dilution of the gas mixture.

B.3 Plasma operation and data recording

- Set up gases (see: gas handling protocol)
- Set up recording
    - Click folder icon near save filename box
    - Navigate to save destination (on D: drive)
    - Make a folder for that day's experiments
    - Create a text file named "test.txt" or something in that folder, and select that as your save file
    - Click "OK." You will now be brought back to the Controller front panel, which will display "test.txt" at the end of the save file path
    - Change this to whatever filename you want to start recording
- Turn on preamp power supply (black box on rack with "V buffer" and "Baratron +" labels. This type of supply is used for the F-100T preamp that is attached to the MCP detector on the UHV chamber.

- Start recording (before or after power on, depending on whether you want to record startup currents)
    - This records all of the data shown in the front panel. This is helpful for changing parameters and not needing to take careful notes on what you did
    - 100 "Samples per loop" is a good high-resolution speed. You can turn this down for even faster data collection, or up to ~500 samples per loop for long data sets.
    - Sample rate is set to 2000 (per second); this is the maximum for this little USB DAQ. Could get better data with a faster DAQ.
    - Program may spontaneously stop recording if file becomes too large (use more samples per loop).
    - More samples = less noise in data.
- After gas is flowing in device, turn on voltage (labeled Plasma Supply) to desired power level.
- Make sure "display" button is on.
    - If chart become laggy, right click on it and select "clear chart." I haven't found a good way to avoid this yet.
- Perform experiments

- Troubleshooting:
    - If current/voltage becomes very unstable, device may be "wearing out." I do not yet understand what causes this behavior.
    - If voltage is on but current is zero, you might not have:
        ..1 connected the wires to the ballast box and/or plasma
        ..2 gas flow
        ..3 contacted the foil with the power wire in the device
        ..4 something grounded
    - If current is nonzero but no light is visible, the device is probably shorting internally.
        ..1 Turn it off! You might also try some different gas flow and power settings to confirm.
        ..2 This could be because of poor contact to plasma, or insufficient insulation in the device (add grease).
- NOTES:
- When you change mix concentrations, it may take up to two minutes (depending on flow rate) for mix gas to reach the plasma.
    - It's best to let it flow for a little while before you assume the mix concentration at the microplasma is accurate

REFERENCES

1. Cooks, R. G.; Ouyang, Z.; Takats, Z.; Wiseman, J. M., Detection Technologies. Ambient mass spectrometry. Science 2006, 311 (5767), 1566-70.

2. Eden, J. G.; Park, S. J.; Cho, J. H.; Kim, M. H.; Houlahan, T. J.; Li, B.; Kim, E. S.; Kim, T. L.; Lee, S. K.; Kim, K. S.; Yoon, J. K.; Sung, S. H.; Sun, P.; Herring, C. M.; Wagner, C. J., Plasma Science and Technology in the Limit of the Small: Microcavity Plasmas and Emerging Applications. Plasma Science, IEEE Transactions on 2013, 41 (4), 661-675.

3. Becker, K. H.; Schoenbach, K. H.; Eden, J. G., Microplasmas and applications. J Phys D Appl Phys 2006, 39 (3), R55-R70.

4. Lazzaroni, C.; Chabert, P., A global model of the self-pulsing regime of micro-hollow cathode discharges. Journal of Applied Physics 2012, 111 (5), 053305.

5. Kushner, M. J., Hybrid modelling of low temperature plasmas for fundamental investigations and equipment design. J Phys D: Appl Phys 2009, 42 (19), 194013.

6. Biborosch, L.-D.; Petzenhauser, I.; Lee, B.-J.; Frank, K.; Schoenbach, K. H., Excimer Emission of Open and Closed Microhollow Cathode Discharges in Xenon. Rom Journ Phys 2005, 50 (7-8), 711-722.

7. Roth, J. R., Industrial Plasma Engineering: Volume 1 - Principles. IOP Publishing LTD: 1995; Vol. 1.

8. Paschen, F., Ueber die zum Funkenübergang in Luft, Wasserstoff und Kohlensäure bei verschiedenen Drucken erforderliche Potentialdifferenz. Annalen der Physik 1889, 273 (5), 69-96.

9. Marić, D.; Škoro, N.; Maguire, P.; Mahony, C.; Malović, G.; Petrović, Z. L., On the possibility of long path breakdown affecting the Paschen curves for microdischarges. Plasma Sources Science and Technology 2012, 21 (3), 035016.

10. Miller, H. C., Breakdown potential of neon below the paschen minimum. Physica 1964, 30 (11), 2059-2067.

11. Eichhorn, H.; Schoenbach, K. H.; Tessnow, T., Paschen's law for a hollow cathode discharge. Appl Phys Lett 1993, 63 (18), 2481-2483.

12. Paschen, F., Bohrs Heliumlinien. Annalen der Physik 1916, 355 (16), 901-940.

13. Gundersen, M. A.; Schaefer, G.; Division, N. A. T. O. S. A., Physics and applications of pseudosparks. Plenum Press: 1990.

14. Gill, P.; Webb, C. E., Electron energy distributions in the negative glow and their relevance to hollow cathode lasers. J Phys D: Appl Phys 1977, 10 (3), 299.

15. Günther-Schulze, A., Die Stromdichte des normalen Kathodenfalles. Z Phys 1923, 19 (1), 313-332.

16. Choi, J.; Iza, F.; Lee, J. K.; Ryu, C. M., Electron and ion kinetics in a DC microplasma at atmospheric pressure. Ieee Transactions on Plasma Science 2007, 35 (5), 1274-1278.

17. Watson, J. T.; Sparkman, O. D., Introduction to mass spectrometry: instrumentation, applications, and strategies for data interpretation. John Wiley & Sons: 2007.

18. Park, S. J.; Eden, J. G.; Chen, J.; Liu, C., Microdischarge devices with 10 or 30 μm square silicon cathode cavities: pd scaling and production of the XeO excimer. Appl Phys Lett 2004, 85 (21), 4869.

19. Schoenbach, K. H.; El-Habachi, A.; Moselhy, M. M.; Shi, W. H.; Stark, R. H., Microhollow cathode discharge excimer lamps. Phys Plasmas 2000, 7 (5), 2186-2191.

20. Shelley, J. T.; Wiley, J. S.; Chan, G. C.; Schilling, G. D.; Ray, S. J.; Hieftje, G. M., Characterization of direct-current atmospheric-pressure discharges useful for ambient desorption/ionization mass spectrometry. Journal of the American Society for Mass Spectrometry 2009, 20 (5), 837-44.

21. Marcus, R. K.; Broekaert, J. A., Glow discharge plasmas in analytical spectroscopy. John Wiley & Sons: 2003.

22. Hippler, R.; Pfau, S.; Schmidt, M.; Schoenbach, K. H., Low temperature plasma physics: fundamental aspects and applications. Low Temperature Plasma Physics: Fundamental Aspects and Applications, by Rainer Hippler (Editor), Sigismund Pfau (Editor), Martin Schmidt (Editor), Karl H Schoenbach (Editor), pp 530 ISBN 3-527-28887-2 Wiley-VCH, June 2001 2001, 1.

23. Lofthus, A.; Krupenie, P. H., The spectrum of molecular nitrogen. J Phys Chem Ref Data 1977, 6 (1), 113-307.

24. Herzberg, G.; Spinks, J. W. T., Molecular spectra and molecular structure. Prentice-Hall: 1966; Vol. 3.

25. Akatsuka, H., Progresses in Experimental Study of N2 Plasma Diagnostics by Optical Emission Spectroscopy. Chemical Kinetics, Chapter 13 2012, 283-308.

26. K.P. Huber and G. Herzberg (data prepared by J.W. Gallagher and R.D. Johnson, I., "Constants of Diatomic Molecules". In NIST Chemistry WebBook, NIST Standard Reference Database Number 69, 2014.

27. Zare, R. N.; Larsson, E. O.; Berg, R. A., Franck-Condon Factors for Electronic Band Systems of Molecular Nitrogen. J Mol Spectrosc 1965, 15 (2), 117-&.

28. Navratil, Z.; Trunec, D.; Smid, R.; Lazar, L., A software for optical emission spectroscopy - problem formulation and application to plasma diagnostics. Czech J Phys 2006, 56, B944-B951.

29. Konjević, N.; Ivković, M.; Sakan, N., Hydrogen Balmer lines for low electron number density plasma diagnostics. Spectrochimica Acta Part B: Atomic Spectroscopy 2012, 76 (0), 16-26.

30. Acon, B. W.; Stehle, C.; Zhang, H.; Montaser, A., Stark-broadened hydrogen line profiles predicted by the model microfield method for calculating electron number densities. Spectrochim Acta B 2001, 56 (5), 527-539.

31. Foest, R.; Schmidt, M.; Becker, K., Microplasmas, an emerging field of low-temperature plasma science and technology. Int J Mass Spectrom 2006, 248 (3), 87-102.

32. Moselhy, M.; Petzenhauser, I.; Frank, K.; Schoenbach, K. H., Excimer emission from microhollow cathode argon discharges. J Phys D: Appl Phys 2003, 36, 2922-2927.

33. Takats, Z.; Wiseman, J. M.; Gologan, B.; Cooks, R. G., Mass spectrometry sampling under ambient conditions with desorption electrospray ionization. Science 2004, 306 (5695), 471-3.

34. Van Berkel, G. J.; Pasilis, S. P.; Ovchinnikova, O., Established and emerging atmospheric pressure surface sampling/ionization techniques for mass spectrometry. J Mass Spectrom 2008, 43 (9), 1161-1180.

35. Venter, A.; Nefliu, M.; Cooks, R. G., Ambient desorption ionization mass spectrometry. Trends Anal Chem 2008, 27 (4), 284-290.

36. Harris, G. A.; Nyadong, L.; Fernandez, F. M., Recent developments in ambient ionization techniques for analytical mass spectrometry. The Analyst 2008, 133 (10), 1297-301.

37. Haapala, M.; Pol, J.; Saarela, V.; Arvola, V.; Kotiaho, T.; Ketola, R. A.; Franssila, S.; Kauppila, T. J.; Kostiainen, R., Desorption atmospheric pressure photoionization. Anal Chem 2007, 79 (20), 7867-72.

38. Cody, R. B.; Laramee, J. A.; Durst, H. D., Versatile new ion source for the analysis of materials in open air under ambient conditions. Anal Chem 2005, 77 (8), 2297-302.

39. Andrade, F. J.; Shelley, J. T.; Wetzel, W. C.; Webb, M. R.; Gamez, G.; Ray, S. J.; Hieftje, G. M., Atmospheric pressure chemical ionization source. 1. Ionization of compounds in the gas phase. Anal Chem 2008, 80 (8), 2646-53.

40. Ratcliffe, L. V.; Rutten, F. J. M.; Barrett, D. A.; Whitmore, T.; Seymour, D.; Greenwood, C.; Aranda-Gonzalvo, Y.; Robinson, S.; McCoustra, M., Surface

analysis under ambient conditions using plasma-assisted desorption/ionization mass spectrometry. Anal Chem 2007, 79 (16), 6094-6101.

41. Jackson, A. T.; Scrivens, J. H.; Williams, J. P.; Baker, E. S.; Gidden, J.; Bowers, M. T., Microstructural and conformational studies of polyether copolymers. Int J Mass Spectrom 2004, 238 (3), 287-297.

42. Harper, J. D.; Charipar, N. A.; Mulligan, C. C.; Zhang, X.; Cooks, R. G.; Ouyang, Z., Low-temperature plasma probe for ambient desorption ionization. Anal Chem 2008, 80 (23), 9097-104.

43. Na, N.; Zhang, C.; Zhao, M. X.; Zhang, S. C.; Yang, C. D.; Fang, X.; Zhang, X. R., Direct detection of explosives on solid surfaces by mass spectrometry with an ambient ion source based on dielectric barrier discharge. J Mass Spectrom 2007, 42 (8), 1079-1085.

44. Coon, J. J.; McHale, K. J.; Harrison, W. W., Atmospheric pressure laser desorption/chemical ionization mass spectrometry: a new ionization method based on existing themes. Rapid Commun Mass Spectrom 2002, 16 (7), 681-685.

45. Kurunczi, P.; Abramzon, N.; Figus, M.; Becker, K. In Measurement of rotational temperatures in high-pressure microhollow cathode (MHC and capillary plasma electrode (CPE) discharges, Slovak Acad Sciences Inst Physics: 2004; pp 115-124.

46. Jinan, C.; Baoming, L.; Daniel, Y. K., Selective surface modification and patterning by a micro-plasma discharge. Appl Phys Lett 2005, 86 (3), 034107.

47. Schoenbach, K. H.; Verhappen, R.; Tessnow, T.; Peterkin, F. E.; Byszewski, W. W., Microhollow cathode discharges. Appl Phys Lett 1996, 68 (1), 13-15.

48. Wang, Q.; Economou, D. J.; Donnelly, V. M., Simulation of a direct current microplasma discharge in helium at atmospheric pressure. Journal of Applied Physics 2006, 100 (2), -.

49. Tonkyn, R. G.; Barlow, S. E.; Orlando, T. M., Destruction of carbon tetrachloride in a dielectric barrier/packed-bed corona reactor. J Appl Phys 1996, 80 (9).

50. Harris, G. A.; Fernandez, F. M., Simulations and Experimental Investigation of Atmospheric Transport in an Ambient Metastable-Induced Chemical Ionization Source. Anal Chem 2009, 81, 322-329.

51. Sunner, J.; Nicol, G.; Kebarle, P., Factors Determining Relative Sensitivity of Analytes in Positive Mode Atmospheric-Pressure Ionization Mass-Spectrometry. Anal Chem 1988, 60 (13), 1300-1307.

52. Cody, R. B., Observation of molecular ions and analysis of nonpolar compounds with the direct analysis in real time ion source. Anal Chem 2009, 81 (3), 1101-7.

53. Kawai, Y.; Yamaguchi, S.; Okada, Y.; Takeuchi, K.; Yamauchi, Y.; Ozawa, S.; Nakai, H., Reactions of protonated water clusters H+(H2O)(n) (n=1-6) with dimethylsulfoxide in a guided ion beam apparatus. Chem Phys Lett 2003, 377 (1-2), 69-73.

54. Kawai, Y.; Yamaguchi, S.; Okada, Y.; Takeuchi, K., Reactions of protonated water clusters H+(H2O)n (n=2 and n=4) with D2O, acetonitrile, acetone, DMS, DMSO, and pyridine. J Mass Spectrom Soc Jpn 2004, 52 (5), 271-76.

55. Honma, K.; Armentrout, P. B., The mechanism of proton exchange: guided ion beam studies of the reactions, H(H2O)n+ (n=1-4)+D2O and D(D2O)n+ (n=1-4)+H2O. The Journal of chemical physics 2004, 121 (17), 8307-20.

56. Kushner, M. J., Modelling of microdischarge devices: plasma and gas dynamics. J Phys D Appl Phys 2005, 38 (11), 1633-1643.

57. Oyler, J.; Darwin, W. D.; Cone, E. J., Cocaine contamination of United States paper currency. J Anal Toxicol 1996, 20 (4), 213-6.

58. Chen, H. W.; Talaty, N. N.; Takats, Z.; Cooks, R. G., Desorption electrospray ionization mass spectrometry for high-throughput analysis of pharmaceutical samples in the ambient environment. Anal Chem 2005, 77 (21), 6915-6927.

59. Song, L. G.; Dykstra, A. B.; Yao, H. F.; Bartmess, J. E., Ionization Mechanism of Negative Ion-Direct Analysis in Real Time: A Comparative Study with Negative Ion-Atmospheric Pressure Photoionization. J Am Soc Mass Spectrom 2009, 20 (1), 42-50.

60. Song, L. G.; Wellman, A. D.; Yao, H. F.; Bartmess, J. E., Negative ion-atmospheric pressure photoionization: Electron capture, dissociative electron capture, proton transfer, and anion attachment. J Am Soc Mass Spectrom 2007, 18 (10), 1789-1798.

61. Adler, F.; Davliatchine, E.; Kindel, E., Comprehensive parameter study of a micro-hollow cathode discharge containing xenon. J Phys D Appl Phys 2002, 35 (18), 2291-2297.

62. Stark, R. H.; Schoenbach, K. H., Electron heating in atmospheric pressure glow discharges. Journal of Applied Physics 2001, 89 (7), 3568.

63. Horning, E. C.; Horning, M. G.; Carroll, D. I.; Dzidic, I.; Stillwel.Rn, New Picogram Detection System Based on a Mass-Spectrometer with an External Ionization Source at Atmospheric-Pressure. Anal Chem 1973, 45 (6), 936-943.

64. Dzidic, I.; Carroll, D. I.; Stillwell, R. N.; Horning, E. C., Comparison of Positive-Ions Formed in Nickel-63 and Corona Discharge Ion Sources Using Nitrogen, Argon, Isobutane, Ammonia and Nitric-Oxide as Reagents in Atmospheric-Pressure Ionization Mass-Spectrometry. Anal Chem 1976, 48 (12), 1763-1768.

65. Zhao, J. G.; Zhu, J. Z.; Lubman, D. M., Liquid Sample Injection Using an Atmospheric-Pressure Direct-Current Glow-Discharge Ionization Source. Anal Chem 1992, 64 (13), 1426-1433.

66. Sofer, I.; Zhu, J. Z.; Lee, H. S.; Antos, W.; Lubman, D. M., An Atmospheric-Pressure Glow-Discharge Ionization Source. Appl Spectrosc 1990, 44 (8), 1391-1398.

67. Monge, M. E.; Harris, G. A.; Dwivedi, P.; Fernandez, F. M., Mass spectrometry: recent advances in direct open air surface sampling/ionization. Chem Rev 2013, 113 (4), 2269-308.

68. Miclea, M.; Okruss, M.; Kunze, K.; Ahlman, N.; Franzke, J., Microplasma-based atomic emission detectors for gas chromatography. Anal Bioanal Chem 2007, 388 (8), 1565-72.

69. Symonds, J. M.; Galhena, A. S.; Fernandez, F. M.; Orlando, T. M., Microplasma discharge ionization source for ambient mass spectrometry. Anal Chem 2010, 82 (2), 621-7.

70. Franzke, J., Microdischarges for analytical applications. Anal Bioanal Chem 2009, 395 (3), 547-8.

71. Franzke, J., The micro-discharge family (dark, corona, and glow-discharge) for analytical applications realized by dielectric barriers. Anal Bioanal Chem 2009, 395 (3), 549-57.

72. Gianchandani, Y. B.; Wright, S. A.; Eun, C. K.; Wilson, C. G.; Mitra, B., Exploring microdischarges for portable sensing applications. Anal Bioanal Chem 2009, 395 (3), 559-75.

73. Vautz, W.; Michels, A.; Franzke, J., Micro-plasma: a novel ionisation source for ion mobility spectrometry. Anal Bioanal Chem 2008, 391 (7), 2609-15.

74. Karanassios, V.; Johnson, K.; Smith, A. T., Micromachined, planar-geometry, atmospheric-pressure, battery-operated microplasma devices (MPDs) on chips for analysis of microsamples of liquids, solids, or gases by optical-emission spectrometry. Anal Bioanal Chem 2007, 388 (8), 1595-604.

75. Weagant, S.; Karanassios, V., Helium-hydrogen microplasma device (MPD) on postage-stamp-size plastic-quartz chips. Anal Bioanal Chem 2009, 395 (3), 577-89.

76. Meyer, C.; Heming, R.; Gurevich, E. L.; Marggraf, U.; Okruss, M.; Florek, S.; Franzke, J., Radiofrequency driven and low cost fabricated microhollow cathode discharge for gaseous atomic emission spectrometry. J Anal Atom Spectrom 2011, 26 (3), 505-510.

77. Guchardi, R.; Hauser, P. C., A capacitively coupled microplasma in a fused silica capillary. J Anal Atom Spectrom 2003, 18 (9), 1056-1059.

78. Park, S. J.; Kim, K. S.; Chang, A. Y.; Hua, L. Z.; Asinugo, J. C.; Mehrotra, T.; Spinka, T. M.; Eden, J. G., Confinement of nonequilibrium plasmas in microcavities with diamond or circular cross sections: Sealed arrays of Al/Al2O3/glass microplasma devices with radiating areas above 20 cm(2). Appl Phys Lett 2006, 89 (22), 221501.

79. Lazzaroni, C.; Chabert, P., Electrical characteristics of micro-hollow cathode discharges. J Phys D Appl Phys 2013, 46 (45), 455203.

80. Hanley, L.; Zimmermann, R., Light and molecular ions: the emergence of vacuum UV single-photon ionization in MS. Anal Chem 2009, 81 (11), 4174-82.

81. Vaikkinen, A.; Haapala, M.; Kersten, H.; Benter, T.; Kostiainen, R.; Kauppila, T. J., Comparison of direct and alternating current vacuum ultraviolet lamps in atmospheric pressure photoionization. Anal Chem 2012, 84 (3), 1408-15.

82. Robb, D. B.; Covey, T. R.; Bruins, A. P., Atmospheric pressure photoionization: an ionization method for liquid chromatography-mass spectrometry. Anal Chem 2000, 72 (15), 3653-9.

83. Chen, Y.; Sullards, M. C.; Hoang, T. T.; May, S. W.; Orlando, T. M., Analysis of organoselenium and organic acid metabolites by laser desorption single photon ionization mass spectrometry. Anal Chem 2006, 78 (24), 8386-94.

84. Kurunczi, P.; Lopez, J.; Shah, H.; Becker, K., Excimer formation in high-pressure microhollow cathode discharge plasmas in helium initiated by low-energy electron collisions. Int J Mass Spectrom 2001, 205 (1-3), 277-283.

85. Meyer, C.; Demecz, D.; Gurevich, E. L.; Marggraf, U.; Jestel, G.; Franzke, J., Development of a novel dielectric barrier microhollow cathode discharge for gaseous atomic emission spectroscopy. J Anal Atom Spectrom 2012, 27 (4), 677-681.

86. Ladislas Wiza, J., Microchannel plate detectors. Nucl Instrum Methods 1979, 162 (1-3), 587-601.

87. Wakaki, M.; Kudo, K.; Shibuya, T., L. In Physical Properties and Data of Optical Materials, CRC Press: 2007; pp 233-268.

88. Ladenburg, R.; Van Voorhis, C. C., The continuous absorption of oxygen between 1750 and 1300A and its bearing upon the dispersion. Phys Rev 1933, 43 (5), 315-321.

89. Watanabe, K.; Zelikoff, M., Absorption Coefficients of Water Vapor in the Vacuum Ultraviolet. J Opt Soc Am 1953, 43 (9), 753.

90. Giuliani, A.; Yao, I.; Lagarde, B.; Rey, S.; Duval, J. P.; Rommeluere, P.; Jamme, F.; Rouam, V.; Wein, F.; De Oliveira, C.; Ros, M.; Lestrade, A.; Desjardins, K.; Giorgetta, J. L.; Laprevote, O.; Herbaux, C.; Refregiers, M., A differential

pumping system to deliver windowless VUV photons at atmospheric pressure. J Synchrotron Radiat 2011, 18 (Pt 4), 546-9.

91. Heath, D. F.; Sacher, P. A., Effects of a simulated high-energy space environment on the ultraviolet transmittance of optical materials between 1050 A and 3000 A. Appl Opt 1966, 5 (6), 937-43.

92. Sansonettia, J.; Martin, W., Handbook of Basic Atomic Spectroscopic Data. Carbon 2005, 100, 1634.

93. Paresce, F., Quantum efficiency of a channel electron multiplier in the far ultraviolet. Appl Opt 1975, 14 (12), 2823-4.

94. Kurunczi, P.; Shah, H.; Becker, K., Hydrogen Lyman-α and Lyman-β emissions from high-pressure microhollow cathode discharges in Ne–H2 mixtures. J Phys B: At Mol Opt Phys 1999, 32, L651-L658.

95. Cottin, H.; Moore, M. H.; Benilan, Y., Photodestruction of relevant interstellar molecules in ice mixtures. Astrophys J 2003, 590 (2), 874-881.

96. Chen, P.; Hou, K.; Hua, L.; Xie, Y.; Zhao, W.; Chen, W.; Chen, C.; Li, H., Quasi-trapping chemical ionization source based on a commercial VUV lamp for time-of-flight mass spectrometry. Anal Chem 2014, 86 (3), 1332-6.

97. Lias, S. G., "Ionization Energy Evaluation". In "Ionization Energy Evaluation", 2011.

98. Abd El-Kader, F. H.; Shokhba, A. A., Molecular and fragment ion structure for ortho- and meta-xylene isomers. Int J Mass Spectrom Ion Phys 1983, 52 (1), 59-63.

99. Fridman, G.; Friedman, G.; Gutsol, A.; Shekhter, A. B.; Vasilets, V. N.; Fridman, A., Applied Plasma Medicine. Plasma Processes Polym 2008, 5 (6), 503-533.

100. Han, X.; Klas, M.; Liu, Y.; Sharon Stack, M.; Ptasinska, S., DNA damage in oral cancer cells induced by nitrogen atmospheric pressure plasma jets. Appl Phys Lett 2013, 102 (23), -.

101. Stypczyńska, A.; Ptasińska, S.; Bahnev, B.; Bowden, M.; Braithwaite, N. S. J.; Mason, N. J., The influence of amino acids on DNA damage induced by cold plasma radiation. Chem Phys Lett 2010, 500 (4–6), 313-317.

102. Papadopoulou, E.; Bell, S. E., Label-Free Detection of Nanomolar Unmodified Single-and Double-Stranded DNA by Using Surface-Enhanced Raman Spectroscopy on Ag and Au Colloids. Chemistry-A European Journal 2012, 18 (17), 5394-5400.

103. Socrates, G.; Socrates, G., Infrared and Raman characteristic group frequencies: tables and charts. Wiley Chichester: 2001; Vol. 245.

104. Barhoumi, A.; Zhang, D.; Tam, F.; Halas, N. J., Surface-enhanced Raman spectroscopy of DNA. J Am Chem Soc 2008, 130 (16), 5523-5529.

105. Ptasińska, S.; Sanche, L., Dissociative electron attachment to hydrated single DNA strands. Physical Review E 2007, 75 (3), 031915.

106. Pristinski, D.; Tan, S.; Erol, M.; Du, H.; Sukhishvili, S., In situ SERS study of Rhodamine 6G adsorbed on individually immobilized Ag nanoparticles. J Raman Spectrosc 2006, 37 (7), 762-770.

107. Ptasinska, S.; Bahnev, B.; Stypczynska, A.; Bowden, M.; Mason, N. J.; Braithwaite, N. S. J., DNA strand scission induced by a non-thermal atmospheric pressure plasma jet. PCCP 2010, 12 (28), 7779-7781.

108. Mühlberger, F.; Wieser, J.; Ulrich, A.; Zimmermann, R., Single photon ionization (SPI) via incoherent VUV-excimer light: robust and compact time-of-flight mass spectrometer for on-line, real-time process gas analysis. Anal Chem 2002, 74 (15), 3790-3801.

109. Heming, R.; Michels, A.; Olenici, S. B.; Tombrink, S.; Franzke, J., Electrical generators driving microhollow and dielectric barrier discharges applied for analytical chemistry. Anal Bioanal Chem 2009, 395 (3), 611-8.

110. Kolasinski, K. K., Surface science: foundations of catalysis and nanoscience. John Wiley & Sons: 2012.

111. Boudaïffa, B.; Cloutier, P.; Hunting, D.; Huels, M. A.; Sanche, L., Resonant Formation of DNA Strand Breaks by Low-Energy (3 to 20 eV) Electrons. Science 2000, 287 (5458), 1658-1660.

112. Ray, S. G.; Daube, S. S.; Cohen, H.; Naaman, R., Electron capturing by DNA. Isr J Chem 2007, 47 (2), 149-159.

113. Ray, S. G.; Daube, S. S.; Naaman, R., On the capturing of low-energy electrons by DNA. Proc Nat Acad Sci USA 2005, 102 (1), 15-19.

114. Nikjoo, H.; O'Neill, P.; Goodhead, D. T.; Terrisol, M., Computational modelling of low-energy electron-induced DNA damage by early physical and chemical events. Int J Radiat Biol 1997, 71 (5), 467-483.

115. Ward, J. F., Biochemistry of DNA Lesions. Radiat Res 1985, 104 (2s), S103-S111.

116. Sidorov, A. N.; Orlando, T. M., Monolayer Graphene Platform for the Study of DNA Damage by Low-Energy Electron Irradiation. J Phys Chem Lett 2013, 4 (14), 2328-2333.

117. Zheng, Y.; Hunting, D. J.; Ayotte, P.; Sanche, L., Role of Secondary Low-Energy Electrons in the Concomitant Chemoradiation Therapy of Cancer. Phys Rev Lett 2008, 100 (19), 198101.

118. Zheng, Y.; Hunting, D. J.; Ayotte, P.; Sanche, L., Radiosensitization of DNA by Gold Nanoparticles Irradiated with High-Energy Electrons. Radiat Res 2008, 169 (1), 19-27.

119. Pan, X.; Sanche, L., Mechanism and Site of Attack for Direct Damage to DNA by Low-Energy Electrons. Phys Rev Lett 2005, 94 (19), 198104.

120. Alizadeh, E.; Sanche, L., Precursors of Solvated Electrons in Radiobiological Physics and Chemistry. Chem Rev 2012, 112 (11), 5578-5602.

121. Baccarelli, I.; Bald, I.; Gianturco, F. A.; Illenberger, E.; Kopyra, J., Electron-induced damage of DNA and its components: Experiments and theoretical models. Phys Rep 2011, 508 (1,Äì2), 1-44.

122. Gu, J.; Leszczynski, J.; Schaefer, H. F., Interactions of Electrons with Bare and Hydrated Biomolecules: From Nucleic Acid Bases to DNA Segments. Chem Rev 2012, 112 (11), 5603-5640.

123. Naaman, R.; Sanche, L., Low-Energy Electron Transmission through Thin-Film Molecular and Biomolecular Solids. Chem Rev 2007, 107 (5), 1553-1579.

124. Sanche, L., Low-energy electron scattering from molecules on surfaces. J Phys B: At Mol Opt Phys 1990, 23, 1597.

125. Rosenberg, R. A.; Abu Haija, M.; Ryan, P. J., Chiral-Selective Chemistry Induced by Spin-Polarized Secondary Electrons from a Magnetic Substrate. Phys Rev Lett 2008, 101 (17), 178301.

126. Rosenberg, R. A.; Frigo, S. P., Fundamental aspects of synchrotron radiation initiated surface chemistry. In Chemical Applications of Synchrotron Radiation, Part II: X-ray Applications, Sham, T. K., Ed. World Scientific Publishing Co.: Singapore, 2002; Vol. 12A, p 462.

127. Akamatsu, K.; Yokoya, A., X-Ray Absorption near Edge Structures of DNA or its Components around the Oxygen K-shell Edge. Radiat Res 2001, 155 (3), 449-452.

128. Fujii, K.; Shikazono, N.; Yokoya, A., Nucleobase Lesions and Strand Breaks in Dry DNA Thin Film Selectively Induced by Monochromatic Soft X-rays. J Phys Chem B 2009, 113 (49), 16007-16015.

129. Fujii, K.; Yokoya, A., Spectral change in X-ray absorption near edge structure of DNA thin films irradiated with monochromatic soft X-rays. Radiat Phys Chem 2009, 78 (12), 1188-1191.

130. Johnson, P. S.; Cook, P. L.; Liu, X.; Yang, W.; Bai, Y.; Abbott, N. L.; Himpsel, F. J., Universal mechanism for breaking amide bonds by ionizing radiation. J Chem Phys 2011, 135 (4), 044702-9.

131. Kade, A.; Kummer, K.; Vyalikh, D. V.; DanzenbaÃàcher, S.; BluÃàher, A.; Mertig, M.; Lanzara, A.; Scholl, A.; Doran, A.; Molodtsov, S. L., X-ray Damage in Protein,àíMetal Hybrid Structures: A Photoemission Electron Microscopy Study. J Phys Chem B 2010, 114 (24), 8284-8289.

132. Tzvetkov, G.; Netzer, F. P., Synchrotron x-ray photoemission study of soft x-ray processed ultrathin glycine-water ice films. J Chem Phys 2011, 134 (20), 204704-8.

133. Wang, J.; Morin, C.; Li, L.; Hitchcock, A. P.; Scholl, A.; Doran, A., Radiation damage in soft X-ray microscopy. J Elec Spec Rel Phen 2009, 170 (1,Äì3), 25-36.

134. Zubavichus, Y.; Fuchs, O.; Weinhardt, L.; Heske, C.; Umbach, E.; Denlinger, J. D.; Grunze, M., Soft X-Ray-Induced Decomposition of Amino Acids: An XPS, Mass Spectrometry, and NEXAFS Study. Radiat Res 2004, 161 (3), 346-358.

135. Ballav, N.; Koelsch, P.; Zharnikov, M., Orientation and Ordering in Monomolecular Films of Sulfur-Modified Homo-oligonucleotides on Gold. J Phys Chem C 2009, 113 (42), 18312-18320.

136. Crain, J. N.; Kirakosian, A.; Lin, J. L.; Gu, Y.; Shah, R. R.; Abbott, N. L.; Himpsel, F. J., Functionalization of silicon step arrays II: Molecular orientation of alkanes and DNA. J Appl Phys 2001, 90 (7), 3291-3295.

137. Fujii, K.; Akamatsu, K.; Yokoya, A., Near-Edge X-ray Absorption Fine Structure of DNA Nucleobases Thin Film in the Nitrogen and Oxygen K-edge Region. J Phys Chem B 2004, 108 (23), 8031-8035.

138. Hua, W.; Gao, B.; Li, S.; Ågren, H.; Luo, Y., Refinement of DNA Structures through Near-Edge X-ray Absorption Fine Structure Analysis: Applications on Guanine and Cytosine Nucleobases, Nucleosides, and Nucleotides. J Phys Chem B 2010, 114 (41), 13214-13222.

139. Kummer, K.; Vyalikh, D. V.; Gavrila, G.; Preobrajenski, A. B.; Kick, A.; Bönsch, M.; Mertig, M.; Molodtsov, S. L., Electronic Structure of Genomic DNA: A Photoemission and X-ray Absorption Study. J Phys Chem B 2010, 114 (29), 9645-9652.

140. Lee, C.-Y.; Gong, P.; Harbers, G. M.; Grainger, D. W.; Castner, D. G.; Gamble, L. J., Surface Coverage and Structure of Mixed DNA/Alkylthiol Monolayers on Gold: Characterization by XPS, NEXAFS, and Fluorescence Intensity Measurements. Anal Chem 2006, 78 (10), 3316-3325.

141. Liu, X.; Zheng, F.; Jürgensen, A.; Perez-Dieste, V.; Petrovykh, D. Y.; Abbott, N. L.; Himpsel, F. J., Self-assembly of biomolecules at surfaces characterized by NEXAFS. Can J Chem 2007, 85 (10), 793-800.

142. Petrovykh, D. Y.; Kimura-Suda, H.; Tarlov, M. J.; Whitman, L. J., Quantitative Characterization of DNA Films by X-ray Photoelectron Spectroscopy. Langmuir 2004, 20 (2), 429-440.

143. Petrovykh, D. Y.; Pérez-Dieste, V.; Opdahl, A.; Kimura-Suda, H.; Sullivan, J. M.; Tarlov, M. J.; Himpsel, F. J.; Whitman, L. J., Nucleobase Orientation and Ordering in Films of Single-Stranded DNA on Gold. J Am Chem Soc 2005, 128 (1), 2-3.

144. Samuel, N. T.; Lee, C.-Y.; Gamble, L. J.; Fischer, D. A.; Castner, D. G., NEXAFS characterization of DNA components and molecular-orientation of surface-bound DNA oligomers. J Elec Spec Rel Phen 2006, 152 (3), 134-142.

145. Schreiner, S. M.; Hatch, A. L.; Shudy, D. F.; Howard, D. R.; Howell, C.; Zhao, J.; Koelsch, P.; Zharnikov, M.; Petrovykh, D. Y.; Opdahl, A., Impact of DNA‚ÄìSurface Interactions on the Stability of DNA Hybrids. Anal Chem 2011, 83 (11), 4288-4295.

146. Vyalikh, D. V.; Danzenbächer, S.; Mertig, M.; Kirchner, A.; Pompe, W.; Dedkov, Y. S.; Molodtsov, S. L., Electronic Structure of Regular Bacterial Surface Layers. Phys Rev Lett 2004, 93 (23), 238103.

147. Zubavichus, Y.; Shaporenko, A.; Korolkov, V.; Grunze, M.; Zharnikov, M., X-ray Absorption Spectroscopy of the Nucleotide Bases at the Carbon, Nitrogen, and Oxygen K-Edges. J Phys Chem B 2008, 112 (44), 13711-13716.

148. Kato, H. S.; Furukawa, M.; Kawai, M.; Taniguchi, M.; Kawai, T.; Hatsui, T.; Kosugi, N., Electronic Structure of Bases in DNA Duplexes Characterized by Resonant Photoemission Spectroscopy Near the Fermi Level. Phys Rev Lett 2004, 93 (8), 086403.

149. Vyalikh, D. V.; Maslyuk, V. V.; Blüher, A.; Kade, A.; Kummer, K.; Dedkov, Y. S.; Bredow, T.; Mertig, I.; Mertig, M.; Molodtsov, S. L., Charge Transport in Proteins Probed by Resonant Photoemission. Phys Rev Lett 2009, 102 (9), 098101.

150. Kelley, S. O.; Barton, J. K.; Jackson, N. M.; McPherson, L. D.; Potter, A. B.; Spain, E. M.; Allen, M. J.; Hill, M. G., Orienting DNA Helices on Gold Using Applied Electric Fields. Langmuir 1998, 14 (24), 6781-6784.

151. Gohler, B.; Hamelbeck, V.; Markus, T. Z.; Kettner, M.; Hanne, G. F.; Vager, Z.; Naaman, R.; Zacharias, H., Spin Selectivity in Electron Transmission Through Self-Assembled Monolayers of Double-Stranded DNA. Science 2011, 331 (6019), 894-897.

152. Ray, S. G.; Daube, S. S.; Leitus, G.; Vager, Z.; Naaman, R., Chirality-Induced Spin-Selective Properties of Self-Assembled Monolayers of DNA on Gold. Phys Rev Lett 2006, 96 (3), 036101.

153. Markus, T. Z.; Daube, S. S.; Naaman, R., Cooperative Effect in the Electronic Properties of Human Telomere Sequence. J Phys Chem B 2010, 114 (43), 13897-13903.

154. Fujii, K.; Akamatsu, K.; Muramatsu, Y.; Yokoya, A., X-ray absorption near edge structure of DNA bases around oxygen and nitrogen K-edge. Nucl Instr Meth B 2003, 199 (0), 249-254.

155. Oka, T.; Yokoya, A.; Fujii, K.; Fukuda, Y.; Ukai, M., Unpaired Electron Species in Thin Films of Calf-Thymus DNA Molecules Induced by Nitrogen and Oxygen K-Shell Photoabsorption. Phys Rev Lett 2012, 109 (21), 213001.

156. Opdahl, A.; Petrovykh, D. Y.; Kimura-Suda, H.; Tarlov, M. J.; Whitman, L. J., Independent control of grafting density and conformation of single-stranded DNA brushes. Proc Nat Acad Sci 2007, 104 (1), 9-14.

157. Ptasinska, S.; Stypczynska, A.; Nixon, T.; Mason, N. J.; Klyachko, D. V.; Sanche, L., X-ray induced damage in DNA monitored by X-ray photoelectron spectroscopy. J Chem Phys 2008, 129 (6), 065102-6.

158. Petrovykh, D. Y.; Kimura-Suda, H.; Whitman, L. J.; Tarlov, M. J., Quantitative Analysis and Characterization of DNA Immobilized on Gold. J Am Chem Soc 2003, 125 (17), 5219-5226.

159. Ravel, B. Athena, 0.8.56; Chicago, 2009.

160. Herne, T. M.; Tarlov, M. J., Characterization of DNA Probes Immobilized on Gold Surfaces. J Am Chem Soc 1997, 119 (38), 8916-8920.

161. Erdmann, M.; David, R.; Fornof, A. R.; Gaub, H. E., Electrically induced bonding of DNA to gold. Nat Chem 2010, 2 (9), 745-749.

162. Leff, D. V.; Brandt, L.; Heath, J. R., Synthesis and Characterization of Hydrophobic, Organically-Soluble Gold Nanocrystals Functionalized with Primary Amines. Langmuir 1996, 12 (20), 4723-4730.

163. Venkataraman, L.; Klare, J. E.; Nuckolls, C.; Hybertsen, M. S.; Steigerwald, M. L., Dependence of single-molecule junction conductance on molecular conformation. Nature 2006, 442 (7105), 904-907.

164. Chen, F.; Li, X.; Hihath, J.; Huang, Z.; Tao, N., Effect of Anchoring Groups on Single-Molecule Conductance: Comparative Study of Thiol-, Amine-, and Carboxylic-Acid-Terminated Molecules. J Am Chem Soc 2006, 128 (49), 15874-15881.

165. Ceballos, G.; Wende, H.; Baberschke, K.; Arvanitis, D., Molecular geometry modifications upon adsorption for N2O: N and O K-edge NEXAFS. Surf Sci 2001, 482-485 (0), 15-20.

166. Klyachko, D. V.; Huels, M. A.; Sanche, L., Halogen Anion Formation in 5-Halouracil Films: X Rays Compared to Subionization Electrons. Radiat Res 1999, 151 (2), 177-187.

167. Xiao, F.; Luo, X.; Fu, X.; Zheng, Y., Cleavage Enhancement of Specific Chemical Bonds in DNA by Cisplatin Radiosensitization. J Phys Chem B 2013, 117 (17), 4893-4900.

168. Mirsaleh-Kohan, N.; Bass, A. D.; Sanche, L., Effect of morphology of thin DNA films on the electron stimulated desorption of anions. J Chem Phys 2011, 134 (1), 015102-8.

169. Orlando, T. M.; Oh, D.; Chen, Y.; Aleksandrov, A. B., Low-energy electron diffraction and induced damage in hydrated DNA. J Chem Phys 2008, 128 (19), 195102-7.

170. Vilar, M. R.; Botelho do Rego, A. M.; Ferraria, A. M.; Jugnet, Y.; Noguès, C.; Peled, D.; Naaman, R., Interaction of Self-Assembled Monolayers of DNA with Electrons: HREELS and XPS Studies. J Phys Chem B 2008, 112 (23), 6957-6964.

171. Sanche, L., Low energy electron-driven damage in biomolecules. The European Physical Journal D - Atomic, Molecular, Optical and Plasma Physics 2005, 35 (2), 367-390.

172. Simons, J., How Do Low-Energy (0.1-2 eV) Electrons Cause DNA-Strand Breaks? Acc Chem Res 2006, 39 (10), 772-779.

173. Fujii, K.; Akamatsu, K.; Yokoya, A., Decomposition of 2-deoxy-D-ribose by irradiation with 0.6 keV electrons and by 0.5 keV ultrasoft X-rays. Int J Radiat Biol 2004, 80 (11-12), 909-914.

174. Wolf, M.; Nettesheim, S.; White, J. M.; Hasselbrink, E.; Ertl, G., Dynamics of the ultraviolet photochemistry of water adsorbed on Pd(111). J Chem Phys 1991, 94 (6), 4609-4619.

175. Ptasinska, S.; Denifl, S.; Scheier, P.; Mark, T. D., Inelastic electron interaction (attachment/ionization) with deoxyribose. J Chem Phys 2004, 120 (18), 8505-8511.

176. Panajotovic, R.; Martin, F.; Cloutier, P.; Hunting, D.; Sanche, L., Effective Cross Sections for Production of Single-Strand Breaks in Plasmid DNA by 0.1 to 4.7 eV Electrons. Radiat Res 2006, 165 (4), 452-459.

177. Markus, T. Z.; Wu, M.; Wang, L.; Waldeck, D. H.; Oron, D.; Naaman, R., Electronic Structure of CdSe Nanoparticles Adsorbed on Au Electrodes by an Organic Linker: Fermi Level Pinning of the HOMO. J Phys Chem C 2009, 113 (32), 14200-14206.

178. Zheng, Y.; Cloutier, P.; Hunting, D. J.; Sanche, L.; Wagner, J. R., Chemical Basis of DNA Sugar-Phosphate Cleavage by Low-Energy Electrons. J Am Chem Soc 2005, 127 (47), 16592-16598.

179. Zheng, Y.; Cloutier, P.; Hunting, D. J.; Wagner, J. R.; Sanche, L., Phosphodiester and N-glycosidic bond cleavage in DNA induced by 4--15 eV electrons. J Chem Phys 2006, 124 (6), 064710-9.

180. Zheng, Y.; Wagner, J. R.; Sanche, L., DNA Damage Induced by Low-Energy Electrons: Electron Transfer and Diffraction. Phys Rev Lett 2006, 96 (20), 208101.

181. Martin, F.; Burrow, P. D.; Cai, Z.; Cloutier, P.; Hunting, D.; Sanche, L., DNA Strand Breaks Induced by 0-4 eV Electrons: The Role of Shape Resonances. Phys Rev Lett 2004, 93 (6), 068101.